2014

MODELING OF AQUEOUS EQUILIBRIUM: THREE-DIMENSIONAL TREND SURFACES (TOPOS)

Mohammad Mainul Hossain
The University of Montana

MODELING OF AQUEOUS EQUILIBRIUM: THREE-DIMENSIONAL TREND SURFACES (TOPOS)

By
MOHAMMAD MAINUL HOSSAIN
MSc, Chemistry, Jahangirnagar University, Dhaka, Bangladesh, 2000

Dissertation
Presented in partial fulfillment of the requirements
for the degree of

Doctor of Philosophy
in Chemistry

The University of Montana
Missoula, MT

July 2014

Approved by:

J. B. Alexander (Sandy) Ross, Dean of the Graduate School
Graduate School and
Committee Member

Garon C. Smith, Chair
Department of Chemistry and Biochemistry

Edward Rosenberg
Department of Chemistry and Biochemistry

Richard J. Field
Department of Chemistry and Biochemistry

Nancy Hinman
Department of Geosciences

Hossain, Mohammad, Ph.D., summer 2014 Chemistry

MODELING OF AQUEOUS EQUILIBRIUM: THREE-DIMENSIONAL TREND SURFACES (TOPOS)

Chairperson: Dr. Garon C. Smith Department of Chemistry & Biochemistry

This dissertation establishes a comprehensive approach to looking at aqueous equilibria phenomena over essentially all feasible compositions of two component solutions – acid-base titrations, metal-ligand complexation, oxidation-reduction couples and solubility of binary ionic compounds. Fundamental to this method is the definition of a composition grid above which numerous system properties can be plotted as three-dimensional trend surfaces to visualize important aspects of system behavior. These have been named "topos" because their appearance is similar to topographic maps. In each case Microsoft Excel™ worksheets have been designed with embedded Visual Basic™ macros that provide an easy means for anyone to generate surfaces of interest. The only inputs required are thermodynamic values such as acid dissociation constants (K_a), overall formation constants (βs), standard reduction potentials (E^o) or solubility product constants (K_{sp}). Once the macro is started, the software generates equilibrium values for system parameters at every composition grid point and then constructs 3-D surfaces in plotting windows. The resultant plots can be rotated in any direction to enhance viewing of surface features.

Several new chemical phenomena have been identified in the course of this project: 1) in acid-base systems buffering against dilution effects has been characterized more thoroughly than previously found in the literature. 2) New equations relating buffer capacity to titration procedures have been derived and visualized as topos. 3) Anti-buffering, a new behavior in metal-ligand complexation systems has been identified; it was confirmed experimentally with a Cu^{2+}-ethylenediamine system where the activity of free Cu^{2+} ion increased more than 100-fold as the system was diluted more than 1300 times. 4) Overall trends in cell potentials have been clarified and utilized in describing why batteries supply a nearly constant voltage until suddenly dying. 5) A composition grid has been designed for future studies on the solubility of ionic compounds.

The interactive Excel spreadsheets are easily adapted to use in pedagogic settings. Suggested PowerPoint teaching resources and explanations of the numerical methods used to solve the equilibrium calculations have been supplied as examples in the acid-base studies.

Acknowledgements

I am delighted to express my deepest sense of gratitude and thanks to my thesis advisor Professor Garon Smith (G Wiz.) for his time, indispensable guidance, constant encouragement and thoughtful suggestions throughout my graduate research. Thanks to my advisory committee Professors Edward Rosenberg, J. B. Alexander (Sandy) Ross, Richard J. Field and Nancy Hinman for their guidance and cooperation during the course of the work. I am appreciative of the visionary role that Dr. Patrick MacCarthy played in shaping the direction of my thesis project. I wish to offer my deepest sense of gratitude to the Department of Chemistry & Biochemistry at University of Montana for the support with teaching assistanceships throughout my graduate study. I owe warm thanks to Professors Mark Cracolice and Trina Valencich for their kindness in helping me learn to teach in a very different culture. Thanks to Jeff Monroe for all his help in general chemistry labs. Thanks to Dr. Glenn Pinson and Daniel Berry for helping me build my experimental apparatus. Ofuka Ichire, a good friend, offered insightful advice. I thank Nurul Huda, Mizan Rahman, Abdul Kadir, Kamrul Hasan, Abdus Sabur, Sadia Jame, Fakhrul Islam and Abdul Goni, to name a few, for their inspiration and advice. I wish to offer my heartiest compliments to my late grandmother, my parents and sisters for their unconditional love and constant inspirations. I wish to extend my gratitude to my M. Sc. thesis supervisor Professor Shariff Kabir, a long time research collaborator of Professor Ed Rosenberg, for his guidance, inspiration and help to advance my graduate study in the United States. Above all, my warm thanks to my beloved wife Ayesha Sharmin. This thesis might have been completed earlier were it not for the loving interruptions by my wonderful daughter Maryam.

Table of Contents

Appendices

List of Figures

Chapter 2

Chapter 3

Chapter 4

Chapter 5

Chapter 6

Chapter 7

Chapter 8

Appendix II

List of Tables

Chapter 3

Chapter 4

Chapter 5

Chapter 1
Introduction and Statement of the Problem

1.1 Introduction

This thesis is primarily a theoretical study of aqueous equilibrium chemistry focusing on aspects of acid-base reactions, metal-ligand complexation reactions, redox reactions and the solubility of ionic salts. The investigation of these areas is initiated through a series of composition grids and associated three-dimensional trend surfaces (topos). Over the wide ranges of compositions established by the grids, numerical methods are employed to model chemical behavior based on underlying equilibrium expressions. The output of the modeling is a series of 3-dimensional topo surfaces that present a visual summary of system trends. Features on these topos often prompt new questions about the underlying chemistry. Previously unperceived or uncharacterized trends may appear as dramatic ridges, plateaus or chasms on the surfaces themselves. New conceptual understandings emerge in seeking their explanation. Counterintuitive outcomes have been confirmed through laboratory experiments.

1.2 Acid-base systems

For acid-base neutralization reactions, a new composition grid has been developed for which the x-axis holds the volume of titrant added while the y-axis tracks dilution of the reagents. Topo surfaces plotted above this grid show both a buffer's pH and its extent of effectiveness (*i.e.,* its capacity). The topos exhibit not only visual evidence for buffering against addition of acids and bases, but also buffering when reagent concentrations are diluted. It is easy to demonstrate how sufficient dilution eventually erodes a buffer's effectiveness, how the simplified Henderson-Hasselbalch[1] equation for calculating a buffer's

pH eventually breaks down, and how the titration curves beyond that point are reminiscent of a dilute strong acid/dilute strong base titration curve. At sufficient dilution, the buffer properties of a system are a function of K_w, the H^+ and OH^- concentrations of the solvent water itself.

This study portrays the buffer capacity changes during a titration as a function of the volume of base added, a viewpoint rarely addressed in acid-base studies. The difference between this new viewpoint and traditional buffer capacity plots is illustrated with side-by-side topo surfaces for comparison. The new buffer capacity surfaces also explore the meaning of buffer capacity for conditions not often considered – strong acid solutions, strong base solutions and extremely dilute systems. Acid samples modeled include a strong acid, a weak monoprotic acid, a weak diprotic acid and a weak triprotic acid.

1.3 Metal-ligand complexation systems

For metal complexation systems a traditional composition grid has been used that plots the total analytical concentration of metal on the x-axis and the total analytical concentration of ligand on the y-axis[2]. The z-axis records the equilibrium activity of free metal. This study identifies an unusual behavior in the concentration of free metal ions that can occur under the right circumstances – the presence of complexes with higher coordination numbers, *i.e.,* more than just a 1:1 stoichiometry, under excess ligand compositions. When these conditions are met, the activity of free metal will actually increase as the overall system is diluted. This behavior will be denoted by the term "anti-buffering". The higher the coordination number of the complexes, the more pronounced the observed anti-buffering in model calculations. A copper

(II) ethylenediamine system was employed to experimentally demonstrate this behavior.

1.4 Redox systems

For redox systems, a new composition grid has been developed to portray the Nernst equation and the chance of half-cell voltages as electrochemical cells operate. One grid axis holds the activity of the oxidized species; the other holds the activity of the reduced species. Calculated potentials for a given composition are plotted as the z-coordinate to form Nernst topo surfaces. The Nernst topos: 1) dramatize the importance of the E^o value over most solution compositions (it is essentially flat); 2) display, as surface pairs, the point where a galvanic cell reaches equilibrium, *viz* $E_{anode} – E_{cathode} = E_{cell} = 0$ V; 3) reveal the underlying principle of a concentration cell; and 4) illustrate systems in which the spontaneous reaction can run in either direction given the proper starting compositions or with changes in temperature or pH.

1.5 Solubility of ionic salts

Solubility equilibrium is traditionally taught from the standpoint of a simple K_{sp} expression[3]. This is an inadequate description of the rich chemistry that can occur. Ion pairing, hydrolysis reactions, dissolved aqueous complexes and polynuclear species are all possibilities. This study presents the simple K_{sp} case topos as the first stage toward looking at these complicating side-reactions in other topo surfaces above a composition grid. The composition grids employed in this part contain the analytical concentration of the anion on the y-axis and the analytical concentration of the cation on the x-axis. A modified definition of solubility is introduced for these surfaces because many systems

are more than just an ionic salt and water. Other components containing common ions can be modeled. The composition topos allow pre-visualization of experimental procedures through which the cation and anion can interact to form a precipitate.

1.6 Numerical Methods and Excel Macros

The exploration and construction of the 3-dimensional topo surfaces described above necessitated the development of numerical techniques and substantial computer programs (Visual Basic macros embedded in MicroSoft Excel) to calculate the equilibrium activities/concentrations of all species in a specified system[4]. These tools provide a rich framework for investigating aqueous equilibria in its full measure.

1.7 Thesis organization

Chapter 2 of this thesis provides an historical account of aqueous equilibrium modeling and three-dimensional trend surfaces. Chapter 3 is an article on acid-base titration surfaces, "3-D Surface Visualization of pH Titration "Topos": Equivalence Point Cliffs, Dilution Ramps, and Buffer Plateaus," that was published in the *Journal of Chemical Education*[4]. Chapter 4 is a companion manuscript on buffer capacity that is being readied for submission to the same journal. Chapter 5 describes a new phenomenon, named anti- buffering, where the activity of free metal increases with overall system dilution. Chapter 6 consists of an application of Nernst topo surfaces "Why Batteries Deliver a Fairly Constant Voltage until Dead" that was also published in the *Journal of Chemical Education*[5]. Chapter 7 is a more complete discussion of topo surfaces for all variables in the Nernst equation. Chapter 8 introduces

solubility topos for the simple K_{sp} case. Finally, Chapter 9 summarizes the insights that have emerged from the topo surface approach and where further development might proceed.

The Appendices include listings of the Visual Basic macros that generate the topo surfaces that are discussed in this thesis. They also contain more detailed descriptions of the experimental methodologies than are possible in published manuscripts. Finally, the complete derivations of the new equations that were required for the buffer capacity topos are provided. Digital copies of all programs used in preparing the topo figures in this thesis are included on a CD that is found in a storage sleeve inside the back cover.

References

1. Po, H. N.; Senozan, N. M. "The Henderson-Hasselbalch Equation: Its History and Limitations," *J. Chem. Ed*. **2001**, 78, 1499-1503.
2. MacCarthy, P.; Smith, G.C. Quantitative Model for Complexation in Multiligand Mixtures, *Chemical Modeling in Aqueous Systems: ACS Symposium Series,* **1979**. 93, Ch10, pp 201–222.
3. Clark, R.W.; Bonicamp, J.M. The Ksp- Solubility Conundrum. *J. Chem. Educ.* **1998**, 75 (9), 1182-1185.
4. Smith, G. C.; Hossain, Md. M.; MacCarthy, P 3-D Surface Visualization of pH Titration "Topos": Equivalence Point Cliffs, Dilution Ramps, and Buffer Plateaus J*. Chem. Educ.*, **2014**, *91* (2), pp 225–231.
5. Smith, G. C.; Hossain, Md. M.; MacCarthy, P. Why Batteries Deliver a Fairly Constant Voltage until Dead *J. Chem. Educ.* **2012**, 89 (11) 1416–1420.

Chapter 2

Background of the Problem: Composition Grids and 3-D Trend Surfaces

2.1 Composition grids

This thesis introduces a series of composition grids, a method of visualizing trends in chemical behavior over a wide range of solution compositions. While many composition grids have been used in the past by other authors, their use has generally been restricted to the characterization of the mixture's composition, not following the trends in some solution parameter as system composition varies. The surfaces displayed in this research are largely innovative. Some of the grids have never before appeared in the literature. Neither have the topo trend surfaces for how pH, buffer capacity, extent of complexation, electrochemical cell voltages and solubility change with solution composition.

2.1.1 Ternary Grids: Triangular composition grids are probably the most frequently encountered style in the scientific literature. A comprehensive review article on ternary diagrams appeared in 1996[1]. This general method of displaying the interaction of three variables was used by Isaac Newton in his 1718 description of hues and shades in his color spectrum[2]. In 1876, J. Willard Gibbs presented the notion of triangular representation of ternary systems as equilateral triangles[3]and in 1894 H.W.B. Roozeboom introduced a right triangular representation of ternary systems[4]. They are used extensively in chemistry[5-7], geology[8,9], biological sciences[10-12] and metallurgy [13-15]. The compositions of a ternary system, one that contains three components, can be

expressed graphically as a point on a triangular-shaped grid (Figure 2.1)[16]. The three corners of the diagram represent the pure components. A mixture of any two components will appear as a point on the edge of the triangle. A mixture of all three will be a point on the interior of the grid. Several schemes have been in use to represent the composition of these three-component systems.

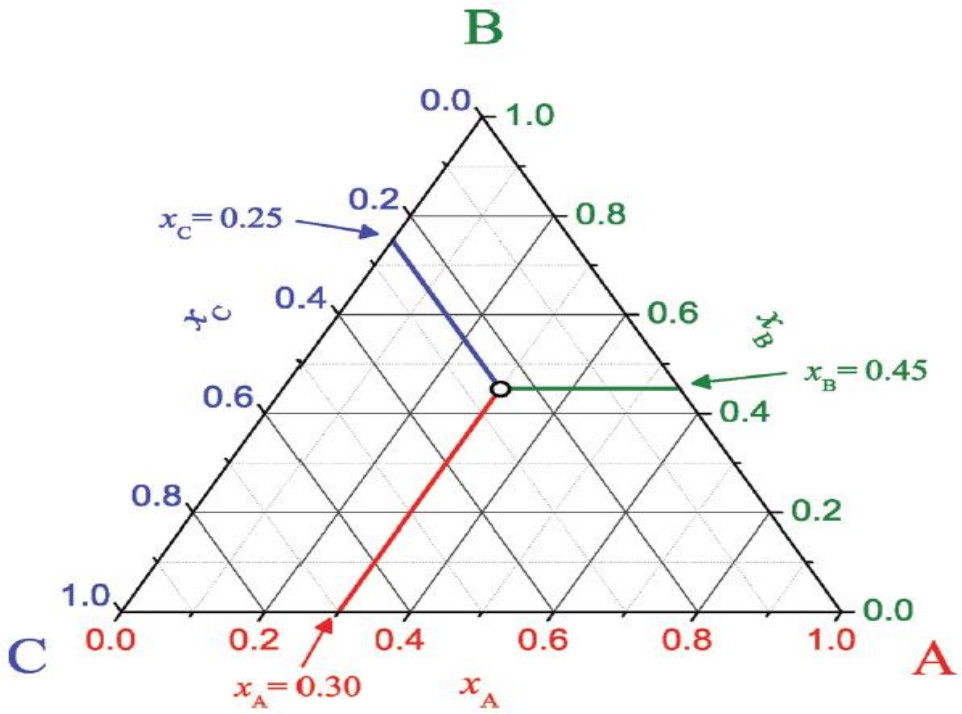

Figure 2.1. Triangular diagram for a ternary mixture with components A, B, and C. The point highlighted on the diagram has the composition x_A = 0.30, x_B= 0.45, and x_C = 0.25 where *x* denotes mole fraction[16]. Coordinates here are read by constructing lines to the appropriate axis that are parallel to the diagram's boundaries.

Not all ternary diagram coordinates are read in the same manner. Since there are at least four methods available for interpreting a ternary composition diagrams, confusion is always possible. Of the available methods for reading ternary diagrams, the parallel and perpendicular approaches are most widely

used (Figure 2.2). Some authors prefer a right isosceles triangle instead of the scalene version shown in Figure 2.2 because it is advantageous pedagogically to represent composition grids in a manner similar to reading conventional rectangular coordinates[17]. Although ternary representations are frequently used in various fields of science, most of them end by simply partitioning the ternary diagram into related groups of composition or phase diagrams.

Panel I

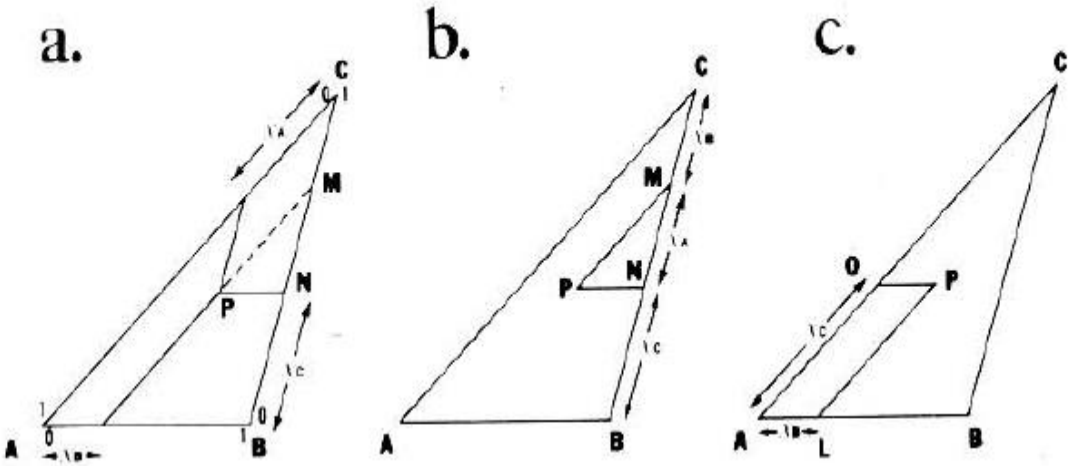

Panel II

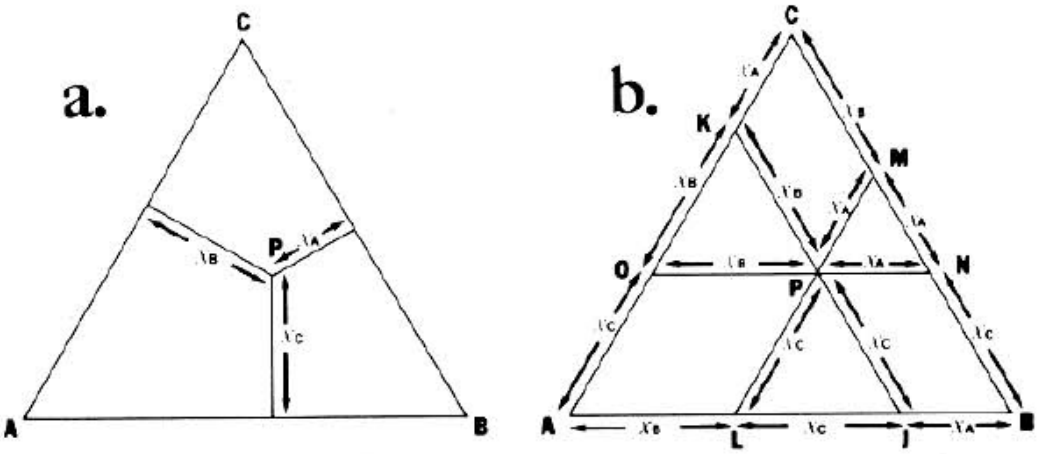

Figure 2.2. Methods of reading ternary diagrams. Panel I demonstrates the perpendicular method of interpretation. Panel II demonstrates the parallel method[17].

For example, in a study on a new class of molten salts as electrolytes, Kubota and others constructed ternary diagrams to note compositional variations with temperature (Figure 2.3).

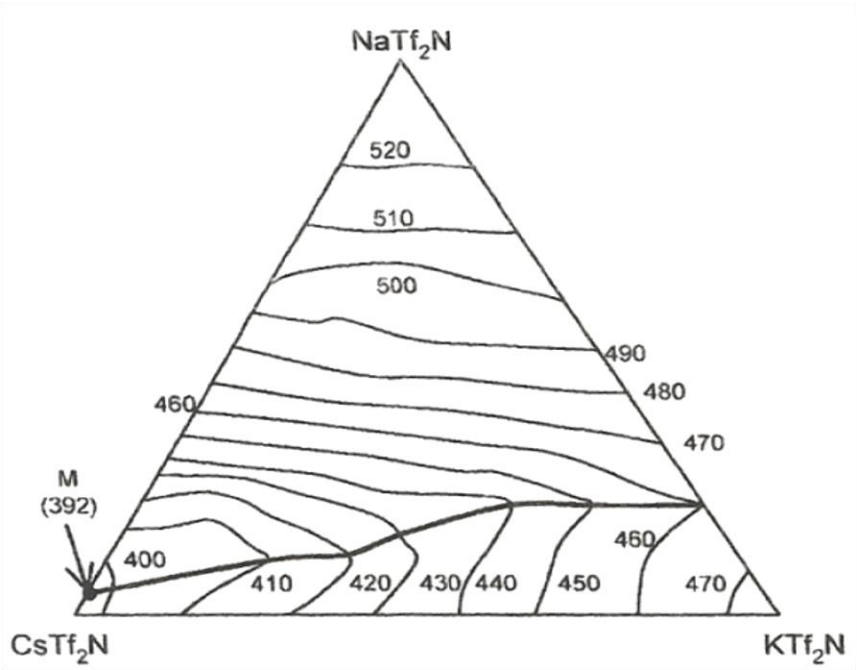

Figure 2.3. Compositional changes in a ternary system with temperature. Molten electrolyte compositions vary in their sodium, cesium and potassium triflet contents as a function of temperature[18].

Note that the main point of this plot is how the composition of the system varies with temperature. It is not about how the composition of the system affects some dependent system variable. The authors actually did generate an (x,y,z)-set of data that is presented as the contour diagram in Figure 2.3. This is a much less effective way to present the overall findings than a 3-dimensional wire-frame surface. When the same data from Figure 2.3 are displayed as a wire-frame surface, the compositional shift to the sodium form at high temperatures is immediately unmistakable. Presented with only the contour diagram of Figure 2.3, the reader must dedicate a significant amount of time in digesting the data and then mentally visualizing what it looks like. With such

easy access to 3-dimensional surface plotting software, wire-frame surfaces should be used more frequently to convey important points about data trends.

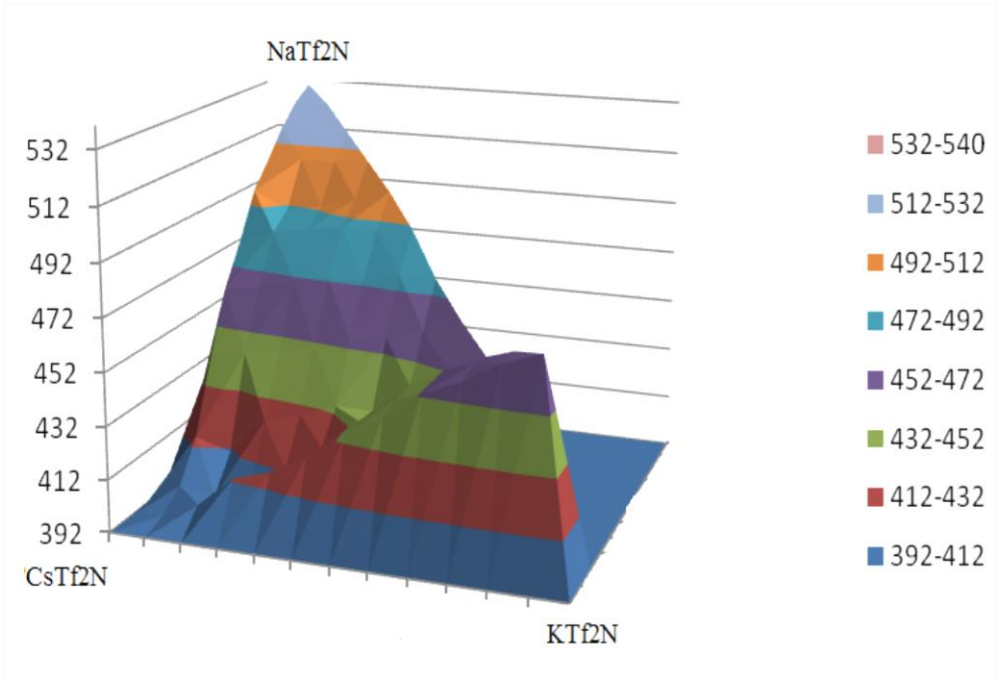

Figure 2.4. 3-Dimensional wire-frame compositional representation of Figure 2.3.

2.2 Composition grids with 3-D surfaces

The equilibrium concepts studied for this thesis are all based on binary composition grids above which three-dimensional topo surfaces for dependent variables are constructed. Constructing a surface plot for a dependent variable above a composition grid, in itself, is not a new idea. Figure 5 illustrates four such examples from the literature: a. Feigenson and Buboltz plot a 3-D surface of fluorescence responses above a composition grid for mixtures of hydrated lamellar lipids [19]; b. Catlett *et al.* illustrate the changes in free Zn^{2+} activity as the pH of a solution and the percent of organic matter are varied [20]; c. Bermudez *et al.* present dose-response changes that occur as the composition of two estrogen compounds are varied[21]; and d. Almas *et al.* show the greater

uptake of Zn-65 in the above-ground plant parts with increasing temperature and addition of organic matter to the soil[22].

Panel I

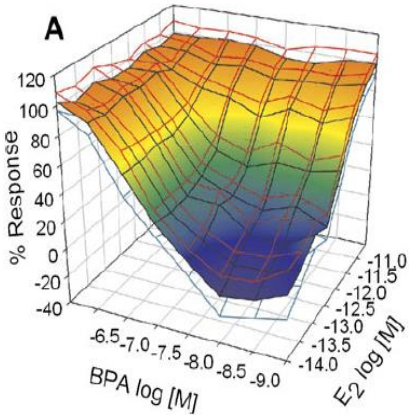

Panel II

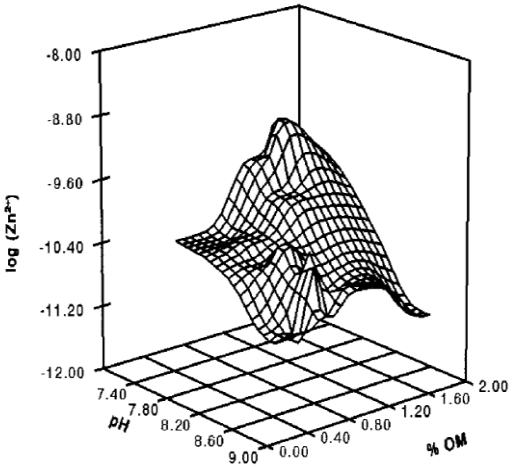

Panel III

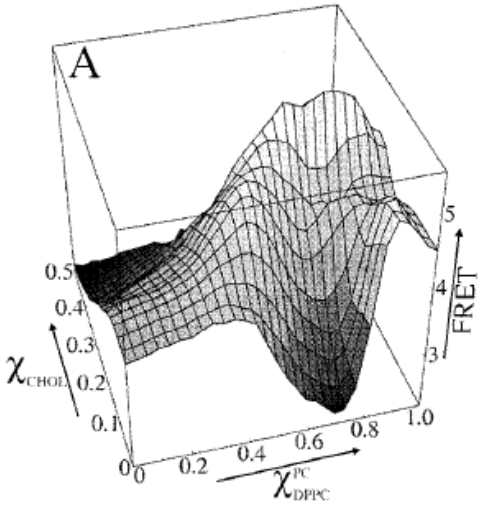

Panel IV

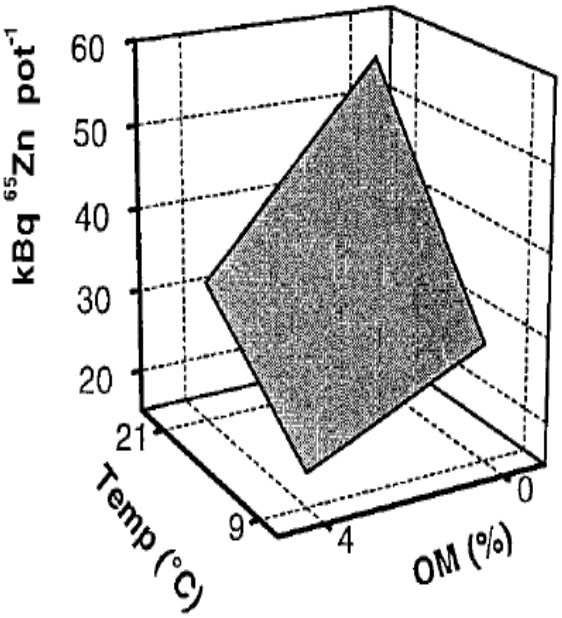

Figure 2.5. Surfaces for dependent variables plotted above a composition grid. Panel I- From reference 19; Panel II- from reference 20; Panel III- from 21; Panel IV- from 22.

2.2.1 Reaction paths

A reaction path on the composition grid is defined by the sequence of compositions that form as solutions are being mixed during the course of an experimental procedure. Reaction paths can be straight lines or curved tracks across the composition grid (Figure 2.6). Batch titrations that maintain one component constant as the other is varied generate experimental paths that parallel one of the grid axes. If the composition axes are logarithmic, dilution procedures diminish both components at the same rate and are represented by lines moving down and to the left with a slope of 1. A traditional titration generates a curved path because, as the titrant is added, its addition dilutes the analyte. Once generated, these reaction paths can be superimposed onto the 3-D surfaces above the grid.

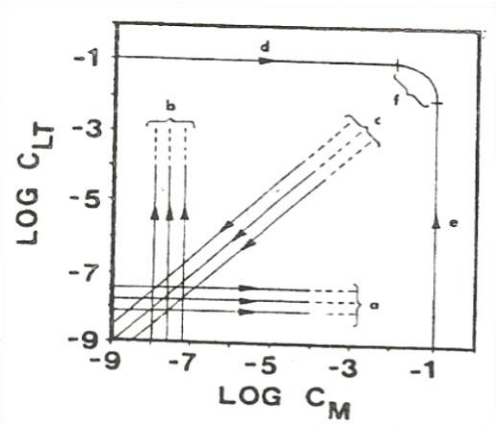

Figure 2.6: Log-log composition grid with reaction paths. (a) Metal into ligand batch titration, (b) ligand into metal batch titration, (c) dilution, (d) symmetrical (i.e. equimolar metal and ligand solutions) metal-into-ligand regular titration, (e) symmetrical ligand-into-metal regular titration. Note that (d) and (e) also correspond to symmetrical continuous variations plot, with most of the experimental points generally lying in the region (f) [23].

2.3.1 Composition grids for this thesis

This thesis project introduces the use of composition grids and 3-D topo surfaces to extend understanding of aqueous equilibrium concepts. Each category of reaction types will require a unique composition grid and/or unique definitions of z-axis variables. The x-axis of most composition grids will usually, but not always, represent analytical activities/concentrations of one species present in the equilibrium system under study and the y-axis will represent the analytical activities/concentrations of the second one. With an appropriate range of values for scales on the x- and y-axes, the composition of essentially any feasible solution made by the mixing of these two species can be represented as a point (x, y) on this two-dimensional coordinate system. The addition of a third variable as the z-axis creates the three-dimensional topo surfaces that will be explored and interpreted in this study.

2.3.2 Acid-base surfaces

The composition grid for visualizing acid-base reactions is constructed by plotting the volume of strong base added on the x-axis and the overall dilution of starting reagents on the y-axis. Most undergraduate analytical chemistry textbooks and many journal articles about titration curves come close to generating this type of composition grid when they plot multiple titration traces at successively more dilute conditions (Figure 2.7). This composition has a linear x-axis but a logarithmic y-axis. Several z-axes will be used to generate topos: 1) pH which is a logarithmic axis; 2) buffer capacity which can be either linear or logarithmic; and 3) distribution diagrams to follow extent of dissociation which is a linear variable. The typical topo is 41 points in the x-direction by 37 points in the y-direction for a total of 1517 grid points.

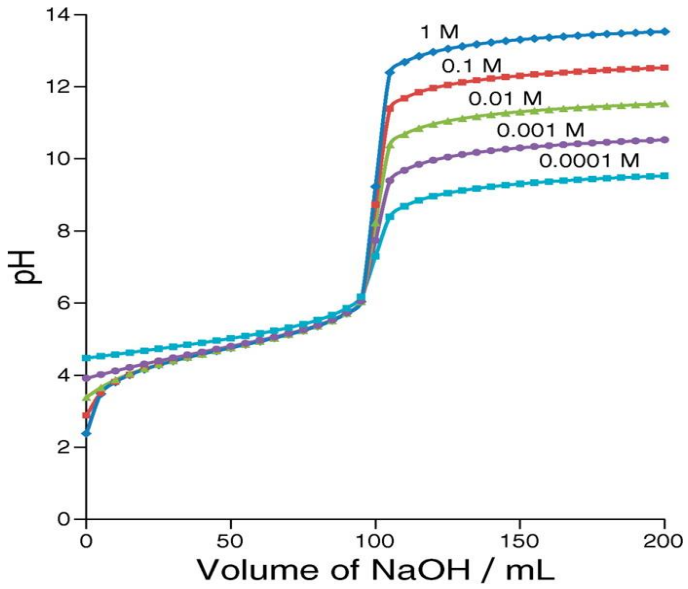

Figure 2.7. Dilution effects on a titration curve for 100 mL of acetic acid titrated with NaOH. Both the acetic acid and NaOH stock solutions are at the molarity noted on each trace.

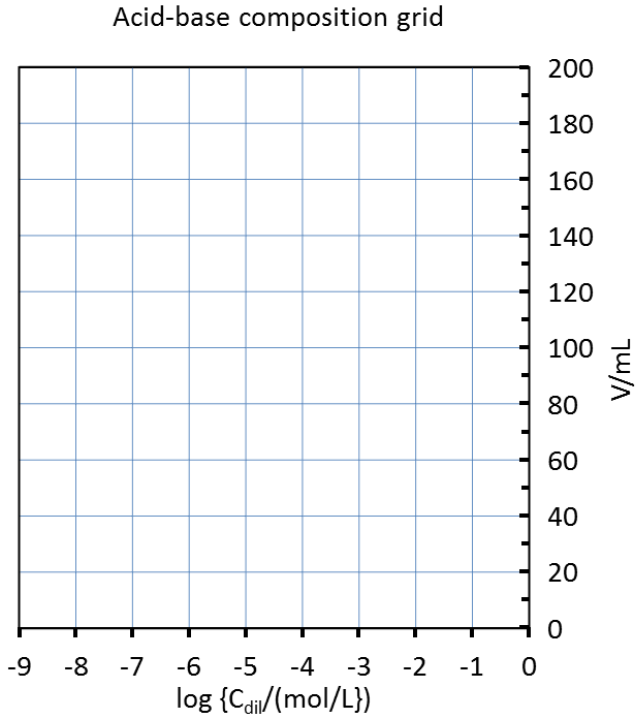

Figure 2.8. The typical composition grid for acid-base titration dilution topo surfaces. For simpler representation number of grid points are reduced. The orientation of the composition grid is rotated 90^{o} counter-clockwise to match the viewing angle of the topos presented in Chapters 3 and 4.

2.3.3 Metal-ligand surfaces

The composition grid for visualizing metal complexation reactions is constructed by plotting the total analytical concentration of metal on the x-axis and the total analytical concentration of the ligand on the y-axis (Figure 2.9). The main focus of this part of the thesis project is to present a rather unexpected consequence of metal complexation systems that contain stoichiometries above 1metal:1ligand. When higher stoichiometries are present (*e.g.,* 1:2, 1:3, etc.) and ligand is in excess, modeling suggests that a situation exists for which trace free metal activities actually increase as a sample is diluted.

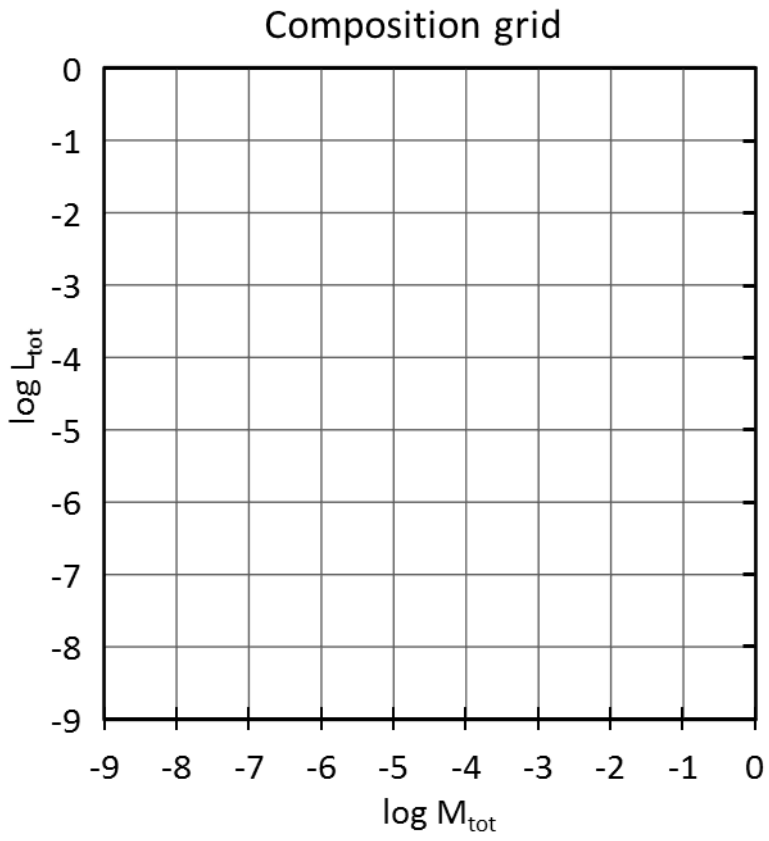

Figure 2.9. Composition grid for metal-complexation topo surfaces.

(The total metal undergoes dilution as expected.) This has been assigned the name "anti-buffering" for the present. Because the anti-buffering phenomenon occurs over many orders of magnitude, a log-log composition grid is used that contains 37 points in each dimension for a total of 1369 grid points. Variables that will be plotted on the z-axis to produce the 3-D topo surfaces are: 1) pM^{n+}, the free metal activity; 2) the activity of other system species; 3) experimental parameters such as absorbance for looking at reaction paths.

2.3.4 Redox surfaces

The composition grid for visualizing redox reactions can be either a linear-linear version or a log-log version depending on what system behavior is being highlighted (Figure 2.10). This is most novel grid because it is constructed by plotting the activity/ concentration of the oxidized form of a half-cell couple on the y-axis and the activity/ concentration of the reduced form of a half-cell couple on the x-axis. The z-axis records the half-cell potential as calculated by the Nernst equation for the redox couple. Reaction paths on this grid correspond to the series of half-cell compositions that are encountered during a current flow, either discharging a voltaic cell or operating an electrolytic cell. The most interesting consequence to emerge through 3-D modeling of Nernst equation surfaces involves superimposed surfaces that correspond to two half-reactions that form a Galvanic cell.

Panel I Panel II

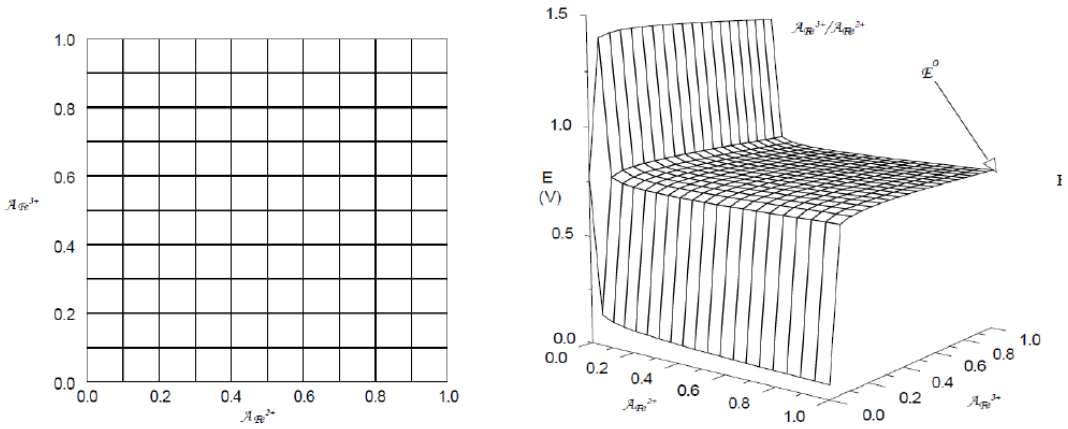

Figure 2.10. The redox composition grid and a Nernst surface. Panel I- The 2-diemensional coordinate system for the $Fe^{3+} + e^- \rightarrow Fe^{2+}$ redox couple. Panel II- The 3-dimensional surface for the calculated Nernst potential (E).

2.3.5 Solubility Surfaces

The composition grid for visualizing solubility of ionic salts is identical to that used for metal complexation topos. It is constructed by plotting the total analytical concentration of cation on the x-axis and the total analytical concentration of the anion on the y-axis (Fig 2.9 is a similar composition grid). The difference here is only in the choice of z-variables. Here the z-axis will be assigned to solubility (both as a linear and a logarithmic value) as well as the activities of individual species or combined aqueous species. The focus of this portion of the overall project is to generate a series of surfaces that embody ever increasing sophistication in capturing the variety of chemical interactions that are possible in a system containing a potential precipitate.

References

1. Howarth, R.J. Sources for a history of the ternary diagram; British Journal for the History of science.1996, 29, 337-356.
2. Newton. I. Opticks or A treatise of the reflections, Refractions, Inflections and colours of Light, 2nd edn, London, 1718, prop.VI, pp.134-137.
3. Gibbs. J.W. Equilibrium of heterogeneous substances trans. Conn. acad. 1876, 3, pp.55-353.
4. Roozeboom, H. W. B. Physik Chem., 1894, 15, 145-158.
5. Freidina, E B.; Fray, D.J. Study of the ternary system$CaCl_2$-NaCl-CaO by DSC; Thermochimica acta 2000, 356, 97-100.
6. Scott, R. L, J. Chem. Phys. 1949, 17, 268-279.
7. Folk, R. L., The distinction between grain size and mineral composition in sedimentary rocks. Journal of Geology 1954, 62, 344-359.
8. Flemming, B.W. A revised textural classification of gravel-free muddy sediments on the basis of ternary diagrams. Cont. Shelf Res. 2000, 20, 1125–1137.
9. Dickinson, W. R.; Beard, L. S.; Breckenridge, G. R., Provenance of North American Phanerozoic sandstones in relation to tectonic setting, Geological Society of America Bulletin 1983, 94, 222-235.
10. Chiarella, R. A.; Davey R. J.; Peterson M. L. Making co-crystals—The utility of ternary phase diagrams. Crystal Growth and Design 2007, 7, 1223-1226.
11. Veatch, S. L. Separation of Liquid Phases in Giant Vesicles of Ternary Mixtures of Phospholipids and Cholesterol, Biophysical Journal 2003, 85, 3074-3083.

12. Feigenson, G. W.; Buboltz, J. T. Ternary Phase Diagram of Dipalmitoyl-PC/Dilauroyl-PC/Cholesterol: Nanoscopic Domain Formation Driven by Cholesterol. Biophysical Journal 2001, 80, 2775-2788.
13. Rideout, S.; Manly, W.D.; Kamen, E.L.; Lement, B.S.; Beek, P.A. Intermediate Phases in Ternary Alloy Systems of Transition Elements, Trans. J Metals 1951, 3,872-876.
14. Van Beek, J.A.; Kodentsov, A.; Van Loo, F.J.J. Phase equilibria in the Cu-Fe-Ti system at 1123 K, J. Alloys Compd. 1995, 217, 97-103.
15. Zheng, K. J.; Hamalainen M., A theoretical study of the phase equilibrium in the Cu-Cr-Zr alloy. J. Alloys Compd. 1995, 220, 53-61.
16. Lombardo, T. G.; Stillinger, F. H.; Debenedetti P. G. Liquids and Structural Glasses Special Feature: Thermodynamic mechanism for solution phase chiral amplification via a lattice model , PNAS 2009 , 106(36),15131-15135.)
17. MacCarthy, P. J. Chem. Educ. 1983, 60, 922-928.
18. Kubota, K.; Noshira, T.; Goto, T.; Hagiwara, R. J. Chem. Eng. Data 2008, 53, 2144-2147.
19. Feigenson, G. W.; Buboltz, J. T. Ternary Phase Diagram of DipalmitoylPC/Dilauroyl-PC/Cholesterol: Nanoscopic Domain Formation Driven by Cholesterol. Biophysical Journal 2001, 80, 2775-2788.
20. Catlett, K. M.; Heil, D. M.; Lindsay, W. L.; Ebinger, M. H. Soil chemical properties controlling zinc activity in 18 Colorado soils. Soil Sci. Soc. Am. J. 2002, 66, 1182-1189.
21. Bermudez, D. S.; Gray, L.E.; Wilson, V. S. Toxicological sciences 2010, 116(2), 477-487.

22. Almas, A. R.; Singh, B. R. Plant uptake of Cadmium-109 and Zinc-.65 at Different Temperature and Organic Matter Levels. J. Environ Quality 2001, 30, 869–877.
23. MacCarthy, P.; Smith, G. Stability Surface Concept. In Chemical Modeling in Aqueous Systems; Jenne, E. ed; ACS Symposium Series 93; American Chemical Society: Washington, DC, 1979, 201-222.

Chapter 3

3-D Surface Visualization of pH Titration "Topos": Equivalence Point Cliffs, Dilution Ramps, and Buffer Plateaus

3.1 Introduction

One of the traditional approaches to understanding acid− base chemistry and pH is to study titration curves. Titration curves appear in virtually every general chemistry textbook[1–3] and titration procedures constitute an experiment in essentially every introductory laboratory manual[4,5]. But there are subtleties to titration curves that are often overlooked. For example, as a system is diluted, the magnitude of the equivalence point break deteriorates, buffer plateaus erode, and auto-dissociation of water eventually begins to dominate a system. This paper introduces 3-D topographic pH surfaces ("topos") with "cliffs", "plateaus", and "ramps" that change with addition of base or dilution of the system. The pH topos are designed to help beginning students see how acid dissociation constants, K_a's, affect pH and titration curves. As such, they are appropriate in teaching pH fundamentals in first-year college chemistry courses. But because the topos invite the reader to consider acid−base behavior over a broad range of conditions, they can also help students in upper-division analytical chemistry courses appreciate some nuances of acid−base behavior. Most specifically, the topos reveal how dilution affects a buffered system, a topic not pursued in standard analytical texts. The interactive spreadsheets permit students to quickly see the results of what would otherwise be an infeasible set of extensive calculations. The Supporting Information includes suggested timing and uses of

topos in lecture, provides PowerPoint slides to use in the classroom, suggested worksheets, and extensions into laboratory activities.

3.2 Titration curve calculations

S.P.L. Sørensen first formulated the concept of pH in 1909,[6] realizing that pH control via buffers was critical to his experiments with enzymes. But pH as a concept in introductory chemistry courses did not occur until about forty years later.[7] Even then, before the advent of digital computers, rigorous pH calculations were arduous. Titration curves were often computed using approximations with concomitant underlying assumptions. As computers and hand-held calculators evolved, a steady stream of papers appeared regarding how to solve the exact equations using numerical methods. A leader in this area was Lars Sillén of Sweden's Royal Institute of Technology[8]. Software packages that performed a wide variety of titration calculations for pH, buffers, and species distributions were available from JCE Software in 1989[9] and in an updated version again in 1998[10]. Unfortunately, these are no longer available. At this writing, CurTiPot, spreadsheets that do many of the same functions, is provided as a free download from I.G.R. Gutz[11]. This paper introduces a 3-D topo surface approach to pH and buffer calculations that offers new insights into old topics. Included in the Supporting Information is an Excel spreadsheet with embedded macros that will allow the reader to reproduce all pH surfaces discussed here as well as allowing them to create a pH surface for any other mono-, di-, or triprotic acid they wish to view. The only input required is acid dissociation constants, K_a values. Calculations utilized in creating the figures in this paper were performed in the Excel

environment using its Visual Basic programming capabilities. For topo surface plots, pH values must be calculated at regularly spaced grid intervals. A grid point consists of the volume of base added plus the logarithm of the overall system dilution, (V_b, log C_{dil}). The regular volume intervals required for topos demands numerical methods to solve a higher-order polynomial expression for each grid point. Many titration curve calculations in the literature are done in the inverse direction where the pH is stepped at regular intervals and plotted at whatever volume of base results[12,13]. Although these offer computational ease, they are not suitable for topo surface plots. A separate gridding operation would be required to yield interpolated volume values. Grid point pH values were computed to 15 significant figures. This permits species concentrations to be expressed far beyond the precision that can be measured in real experimental procedures. Although such precise results are beyond any instrumentation, they are completely valid in a theoretical sense. For the purpose of clarity, activity effects have not been explicitly included in the model systems. Their inclusion would be necessary before modeled results would match experimental measurements. They would not affect any of the conceptual points made in this paper. Real systems whose ionic strength is controlled would exhibit surfaces identical to those in this paper except for scalar factors. Values for K_a's are taken from Martell and Smith's Critical Stability Constants[14].

3.3 The titration and dilution pH topo surface

The discussion of pH changes and buffers is usually illustrated by means of titration curves. But a single titration curve displays only one set of solution

concentrations. As the reagents for a titration are diluted, the associated titration curve also changes (Figure 3.1). This point is made by many authors who, with multiple traces, show the equivalence point break diminishing as one goes to progressively more dilute conditions[15–17]. A close examination of the curves reveals that dilution causes each successive curve to start at a slightly higher level plus the magnitude of the post-equivalence point plateau drops by one pH-unit each time the reagents are diluted by a factor of 10.

A more comprehensive view of pH behavior during acid− base titrations can be visualized by plotting 3-D topo surfaces above a composition grid that encompasses most feasible reagent concentrations. The grid is constructed by recording the progress of a titration (volume of strong base added) on the x axis and following the overall dilution of the system (log C_{dil}) on the y axis. All concentrations are expressed in molarity (M). It is important to note that the x axis is linear whereas the y axis is logarithmic. When the pH associated with a set of regularly spaced grid points is plotted on the logarithmic z axis, a 3-D pH topo surface is generated. All surfaces for this paper are based on an initial volume of 100.0 mL for the acid analyte. The pH topo surface for acetic acid is shown in Figure 2 based on a K_a of 1.75×10^{-5}. The right-hand edge of the surface corresponds to a traditional titration curve as seen in texts and papers. As one moves to the left along the log C_{dil} axis, progressively more dilute conditions are encountered. For the most concentrated system (i.e., the line that forms the right-hand edge of the surface), 1.0 M CH_3COOH is being titrated with 1.0 M NaOH. Successive lines in the dilution direction indicate repeating the titration with both the acid and base concentrations adjusted identically.

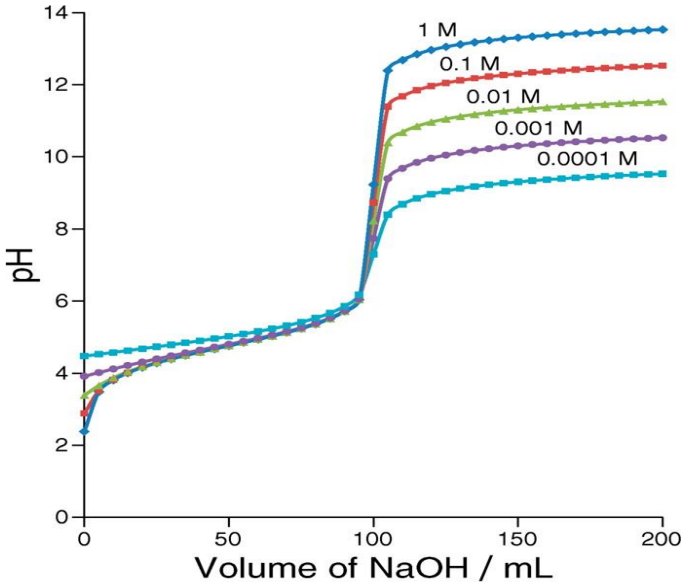

Figure 3.1. Dilution effects on a titration curve for 100 mL of acetic acid titrated with NaOH. Both the acetic acid and NaOH stock solutions are at the molarity noted on each trace.

Thus, at the most dilute point (the left-hand edge of the surface), 1.0×10^{-9} MCHCOOH is being titrated with 1.0×10^{-9} M NaOH. The five traces in Figure 3.1 are simply five of the 37 slices that comprise the overall pH topo surface of Figure 3.2, specifically, those slices corresponding to log C_{dil} values of 0, −1, −2, −3, and −4. With the complete topo surface, finer gradations between whole-numbered dilution values are seen. With an entire pH topo surface to view, one can discern a series of ramp, cliff, and plateau features. Ramps are associated with grid regions where dilution dominates the solution pH. Cliffs occur at initial and equivalence points during a titration procedure. Plateaus are indicative of situations in which pH is somewhat stable, that is, buffer zones plus extreme dilution conditions. The equivalence point cliff on the acetic acid pH topo appears at 100 mL of NaOH added. At the equivalence point, the solution is identical to

dissolving pure $NaCH_3COO$ in water. Beyond the 100 mL mark, excess NaOH titrant is now being added to the solution.

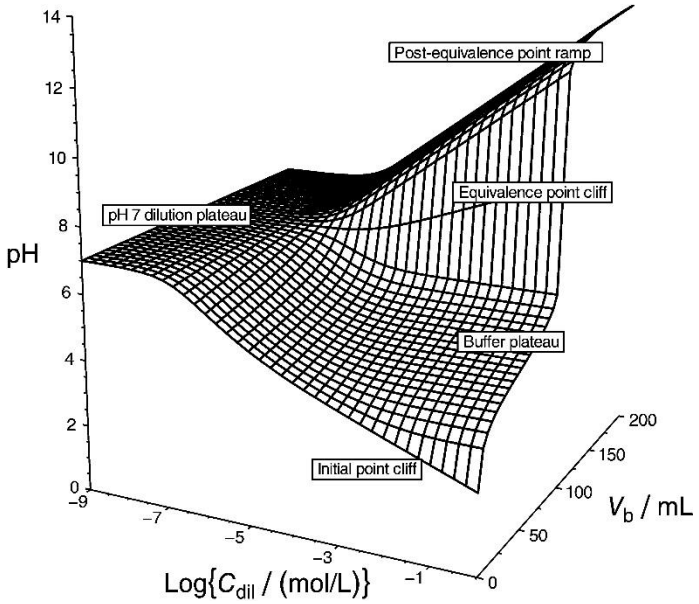

Figure 3.2. The acetic acid pH topo surface for a 100 mL sample.

Because NaOH is a strong base, the pH rapidly rises toward the pH of the titrant solution itself. As one moves to the left on the topo surface with dilution, the heights of cliffs diminish and all ramps proceed toward the pH 7 dilution plateau. Notice, for example, the change in the equivalence point cliff from its dramatic rise at a log C_{dil} of 0 to its pinched out ending at a log C_{dil} of about −6. As titration traces to the left are considered, the concentration of the NaOH titrant (as well as that of the analyte) is being systematically lowered. For a while, each log unit moved to the left also drops the post-equivalence point ramp pH by one unit. Eventually, however, when the titrant becomes sufficiently dilute with respect to NaOH (e.g., 1.00×10^{-6} M), the contribution of OH^- from the auto-dissociation of water (1×10^{-7} M) begins to become more significant. By the last titration slice, when the titrant is 1.0×10^{-9} M NaOH, the OH^- from water overwhelms that from

the titrant a hundred-fold. The concentration of OH^- in the 10^{-9} titrant would actually be 1.01×10^{-7} M where the first "1" is OH^- from water and the second "1" is OH^- from NaOH. The pH of this titrant is essentially 7. So, too, is the pH of the starting analyte mixture about 7. From modeling calculations, the H_3O^+ concentration in the 1×10^{-9} M CH_3COOH at the start is 0.000 000 100 498 M, a pH of 6.9978. There is no equivalence point cliff in the pH 7 dilution plateau because the total pH range of the entire trace varies from 6.9978 at 0 mL NaOH added to 7.00073 at 200 mL of NaOH added.

3.4 Strong acid versus weak acid topo surface

To better understand the initial point cliff and buffer plateau features on the acetic acid pH topo surface of Figure 3.2, it is helpful to first look at the topo for a strong acid−strong base titration. An example of this, the pH topo surface for hydrochloric acid titrated with NaOH, is shown as Figure 3.3. The pH topo for a strong acid shows no plateau in front of the equivalence point cliff. There is simply a broad pre-equivalence point ramp. This ramp shows solution behavior when there are no buffer interactions occurring. In the volume direction, the pH shows a shallow rise until the equivalence point is reached. This is "pseudo buffering", an artifact of the logarithmic nature of pH[18]. With dilution, however, there is a direct relationship with pH. The pre-equivalence point ramp rises to the left at a 45° slope; the concentration of H_3O^+ changes by an order of magnitude with each order of magnitude change caused by dilution. The linearity of the ramp eventually begins to degrade as contributions of H_3O^+ from the water of dilution start to become significant at about a log C_{dil} of −6. Weak acid pH topo surfaces

will have a buffer plateau and an initial point cliff that is not seen with a strong acid pH surface. This is immediately apparent when comparing Figures 3.2 and 3.3. To assist in visual comparison, Figure 3.4 superimposes the pH topo of acetic acid on top of that for HCl. The influence of the buffer action between acetic acid and acetate ion lifts the pH surface above the pre-equivalence point ramp.

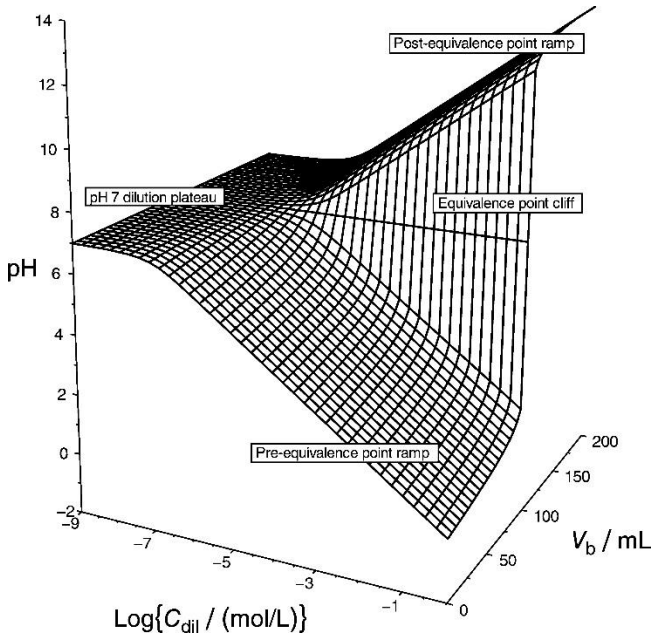

Figure 3.3. The hydrochloric acid pH topo surface for a 100 mL sample.

Any portions of the pH surface that are oriented at less than a 45° angle in the dilution direction have some buffer influence taking place.

3.5 A detailed analysis of other topo features for acetic acid

Weak acids will usually exhibit both an initial point cliff as well as a buffer plateau prior to the equivalence point cliff. Acetic acid is a typical monoprotic carboxylic acid. Its buffer plateau is centered around pH = pK_a = 4.757 and extends from the front edge of the surface to about midway toward the back.

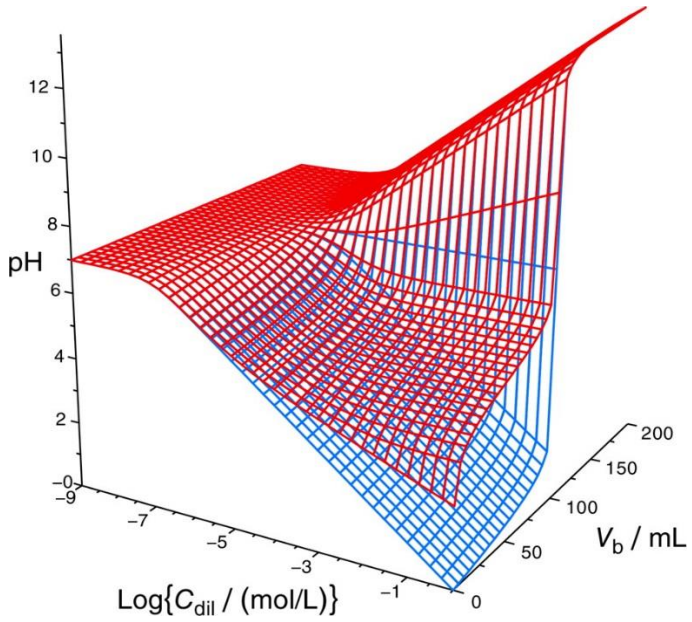

Figure 3.4. Overlay of acetic acid (red) and hydrochloric acid (blue) pH topo surfaces.

In the volume direction, it sits between the initial point cliff and the equivalence point cliff. This is the type of buffer behavior that is generally described. Most introductory chemistry texts introduce the Henderson−Hasselbalch equation 3.1[9] to demonstrate that pH is primarily governed by the pK_a and is then modified by the ratio of the buffer's base form to acid form to account for any imbalance in their relative amounts (eq 3.1):

Table 3.1. A Dilution Example for a 1.0 M System of Acetic Acid

	$[H_3O^+]$	**$[CH_3COO^-]$**	**$[CH_3COOH]$**	**base/acid ratio**	**pH**
Before dilution	1.749816×10^{-5}	0.3333508	0.3333158	1.000105	4.7570075
After dilution*	1.839816×10^{-6}	0.03333508	0.03333158	1.000105	5.7535226
At equilibrium	1.748165×10^{-5}	0.03335081	0.03331585	1.001049	4.7574175

"Includes a contribution of $[H_3O^+]$ from the pH 7 diluent water before accounting for equilibrium shifts"

Table 3.2. A Dilution Example for a 10^{-3} M System of Acetic Acid in Which the Henderson−Hasselbalch Equation Is Beginning To Fail

	$[H_3O^+]$	**$[CH_3COO^-]$**	**$[CH_3COOH]$**	**base/acid ratio**	**pH**
Before dilution	1.590600×10^{-5}	3.492387×10^{-4}	3.174280×10^{-4}	1.100214	4.7984391
After dilution*	1.680600×10^{-6}	3.492387×10^{-5}	3.174280×10^{-5}	1.100214	5.7745356
At equilibrium	9.645684×10^{-6}	4.297798×10^{-5}	2.368869×10^{-5}	1.814283	5.0156670

"Includes a contribution of $[H_3O^+]$ from the pH 7 diluent water before accounting for equilibrium shifts"

$$\mathrm{pH} \cong \mathrm{p}K_a + \log \frac{[C_b]}{[C_a]} \qquad \text{(eq 3.1)}$$

C_b and C_a are the respective stoichiometric concentrations of the base and acid forms of the buffer compound uncorrected for dissociation and hydrolysis. This is really just a special case for the more general mass action law of Guldberg and Waage[20, 21]. The Henderson−Hasselbalch form is only valid at relatively high concentrations of acid and base. Movement along the volume axis corresponds to adding a relatively concentrated solution of strong base, NaOH. When the base buffer capacity is exceeded, the Henderson−Hasselbalch equation no longer holds. The pH rapidly shoots upward at the equivalence point cliff, headed eventually for the pH of the NaOH solution that is being used as the titrant. Less frequently discussed is buffer behavior of a system as it undergoes dilution. A classical treatment of this subject was presented by Bates in 1954[15]. He organized his discussion around the pH shift caused by diluting a sample by a factor of 2, ΔpH1/2, and follows dilution effects over a total dilution range of 40-fold. The treatment in this paper tracks the pH changes across nine orders of dilution magnitude. Dilution of a buffer is a complex situation. For this analysis, it is better to consider the logarithmic form of the Guldberg and Waage mass action law (eq

3.2) that is general for all conditions[20, 21]. Note that, unlike eq 3.1, it employs equilibrium concentrations rather than stoichiometric concentrations:

$$pH = p\mathcal{K}_a + \log\frac{\left[CH_3COO^-\right]}{\left[CH_3COOH\right]} \qquad \text{(eq 3.2)}$$

When the pH of the buffer plateau is less than 7, the dilution effects are largely controlled by the concentration of the buffer's acid form. Diluting a 1 M H_3O^+ solution by 10, for instance, should drop the H_3O^+ concentration to 0.1 M and give rise to a ~1 pH unit change. This is where changes would stop with concentrated solutions of a strong acid and is the basis for the pre-equivalence point ramp for the HCl surface of Figure 3.3. But a solution containing a buffer will rebound from the dilution-caused pH rise. The basis for the counteraction comes out of the acid dissociation reaction (eq 3.3):

$$CH_3COOH + H_2O \leftrightarrow CH_3COO^- + H_3O^+ \qquad \text{(eq 3.3)}$$

Because H_2O is a reactant in eq 3.3, Le Chatelier's principle and mass action law dictate that the reaction will shift to the right until a new equilibrium is established. Thus, [CH_3COOH] will drop and [CH_3COO^-] will rise. If the buffer is working well, the system will rebound to almost the same pH. The dissociation of CH_3COOH needs to supply essentially 90% of the H_3O^+ if the effect of 10-fold dilution is to be overcome. Dilution will also drive the base form's hydrolysis reaction, but this will be small in magnitude because K_a (1.75×10^{-5}) $\gg$ K_b (5.71×10^{-10}). Consider the situation at the half-equivalence point volume of 50 mL of NaOH added (the Before Dilution row in Table 3.1). Next, let the system be diluted by a factor of 10 (the After Dilution row in Table 3.1). This has upset an equilibrium that will now shift toward the right in eq 3.3 until an equilibrium has once again been established. Using the K_a for acetic acid and the starting values in

the After Dilution row, one can solve for the amount of shift. This is calculated to be 1.573×10^{-5} M, which can be used to correct the After Dilution values to the new At Equilibrium values. These reveal that acetic acid has dissociated a small amount, but this amount of dissociation provides enough H_3O^+ to almost make up for the 10-fold dilution factor. Instead of the pH rising by one whole pH unit as dilution would suggest, the new pH has only risen 0.00041 pH units from its Before Dilution value. As long as there is a sufficient quantity of the acid form to dissociate, it maintains a reservoir of stored protons ready to be released through dissociation.

The Henderson−Hasselbalch equation is valid for dilution events as long as only a small part of the acid form must dissociate. Note in Table 1 that the ratio of base form to acid form has only changed by about 0.1% between the Before and After Dilution values. With successive 10-fold dilutions, an increasing proportion of the acid form must dissociate to maintain the pH. Consider, for example, a 10-fold dilution when the system concentration is 1.0×10^{-3} M. Table 3.2 demonstrates that a higher percentage of the acid form disappears. This results in a noticeable change in the base/acid ratio. Equation 3.2 shows that as the base/acid ratio changes, so too does the pH. The ∼65% shift in the ratio translates into a pH rise of 0.2172279 pH units. Note that the concentration of acetic acid drops by more than an order of magnitude. One order of magnitude for the drop is lost because of dilution. It drops even more, though, because now significant amounts of CH_3COOH are being converted to the base form through dissociation caused by H_2O driving eq 3.3 even further to the right. It is ∼34% lower than just dilution would cause. Conversely, the concentration of acetate does not drop by an order of magnitude, but is 23% higher than dilution alone would produce.

Table 3.3. A Dilution Example for a 10−7 M System of Acetic Acid in Which Contributions from the Auto-dissociation of H_2O Become Significant

	$[H_3O^+]$	**$[CH_3COO^-]$**	**$[CH_3COOH]$**	**base/acid ratio**	**pH**
Before dilution	1.749816×10^{-5}	0.3333508	0.3333158	1.000105	4.7570075
After dilution*	1.839816×10^{-6}	0.03333508	0.03333158	1.000105	5.7535226
At equilibrium	1.748165×10^{-5}	0.03335081	0.03331585	1.001049	4.7574175

"Includes a contribution of $[H_3O^+]$ from the pH 7 diluent water before accounting for equilibrium shifts"

As the dilution of a system approaches 10^{-6} M, a new controlling force for the system pH begins to emerge, namely, the H_3O^+ and OH^- content of the diluent water where $[H_3O^+]$ and $[OH^-]$ are both 1.0×10^{-7} M. Continued additions of this level of H_3O^+ and OH^- begin to overtake influence from the small quantities of buffer components that are present. Table 3 illustrates details of this situation at 10^{-7} M. The diluent water has nearly the same $[H_3O^+]$ as the Before Dilution system so the After Dilution concentration changes little. CH_3COOH is still undergoing further dissociation with dilution, but the H_3O^+ it produces (6.06685×10^{-12} M) does not contribute much. The overall system $[H_3O^+]$ is nearly 5 orders of magnitude larger at 1.016610×10^{-7} M. The upward drift essentially stops when the titration surface pH reaches the vicinity of 7. It is interesting to note, however, that the base to acid ratio continues to change as required by mass action effects.

3.6 The effect of pK_a on pH changes caused by dilution

The lower the pK_a, the sooner dilution causes the buffer plateau to start drifting upward. Figure 3.5 illustrates modeled systems for weak acids with hypothetical pK_a's of 1.00, 2.00, 3.00, and so forth. The traces shown are the dilution slices at 20 mL of NaOH added. This places the slices in a portion of whatever buffer

plateaus exist. Also included is a trace for the 20-mL slice of HCl so that visual comparisons with a strong acid can be made. There are three possible pH behaviors that can occur upon dilution: (1) the pH can vary directly with the amount of dilution; (2) the pH can be controlled by the auto-dissociation of the diluent; and (3) the pH can be stabilized to varying extents by the presence of a buffer system. A system with a strong acid exhibits behaviors 1 and 2 only whereas a system with a weak acid may exhibit all three (Figure 3.5). When the weak acid trace begins to overlap the HCl trace, then both strong and weak acids exhibit similar dilution behavior.

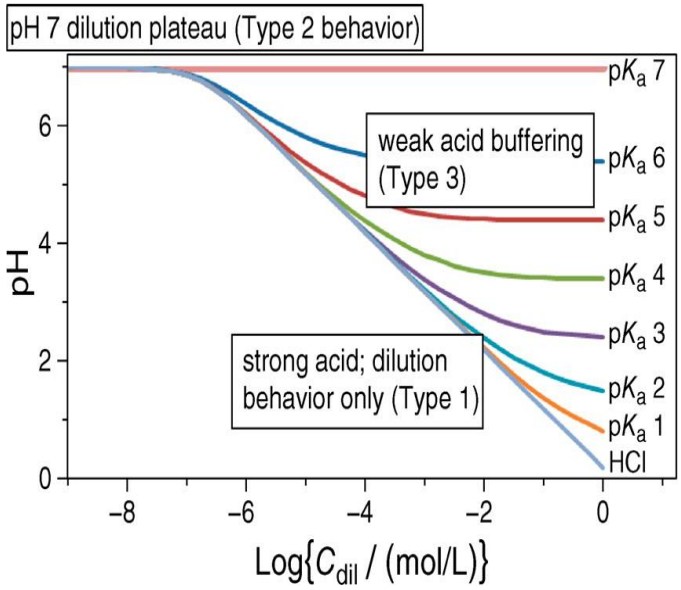

Figure 3.5. Dilution effect on pH vs pK_a value for 20 mL-added slices.

A strong acid system shows no buffer character. Strong acids essentially dissociate completely, so almost no associated form, that is, an HCl molecule, exists in water to react with added OH^-. The only significant acid in the system is H_3O^+.As a concentrated system is diluted, so too is the H_3O^+. This is the type 1 behavior listed above and leads to a graphical trace that rises at a 45° angle to the left. Eventually, however, the H_3O^+ content of the diluent water itself becomes

significant compared to the diluted H_3O^+ produced by the strong acid. When the system approaches 10^{-6} M, the H_3O^+ from diluent water starts to make headway over the remaining trace-level amounts of strong acid. Ultimately, it completely overwhelms the original H_3O^+ from the strong acid. The pH sits close to 7. This is type 2 behavior. A weak acid system will demonstrate type 3 behavior, a situation in which the effect of dilution is counteracted, sometimes almost completely. This is buffering against dilution and will occur to greater and greater extents as the pK_a of the acid approaches 7.00 (Figure 3.5). Weak acids only partially dissociate upon dilution, but they release sufficient protons in doing so that the pH does not rise so swiftly. The reason that pK_a's closer to 7.00 show more protracted buffering against dilution is because the weaker the acid, the less it dissociates when placed in water. Ever greater degrees of dilution are required to consume its base buffer capacity.

Figure 3.6 illustrates how many orders of magnitude of dilution are required to raise the pH of the system by 1 unit at the half equivalence point. This is illustrative of where the assumptions in the Henderson− Hasselbalch equation (eq 3.1) are beginning to fail. Note that $pK_a = 5$ is the highest value shown in Figure 3.6. At a pK_a of 6 there is never a 1-pH unit rise caused by dilution. Eventually, weak acids with pK_a's lower than 7 dissociate to the point at which they are indistinguishable from a strong acid. Figure 3.5 illustrates this point for weak acids. At a log C_{dil} value of around −6.0, there is no difference between the acidity of a solution of HCl and a weak acid with a pK_a of 5. Under these conditions, the pK_a 5 weak acid is a strong acid. As a special case, consider a hypothetical acid with a pK_a of 7.00. This acid would exhibit perfect buffering against dilution to any extent. Our modeled system for the pK_a 7.00 acid shows a

dilution slice at the 50-mL half-equivalence point with a pH of exactly 7.00000... across the entire surface.

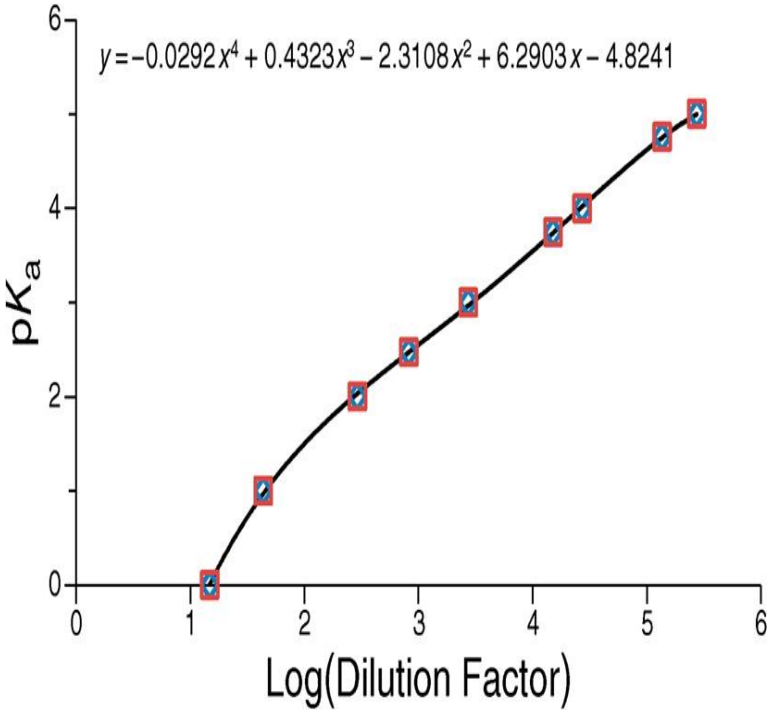

Figure 3.6. Orders of magnitude of dilution required to shift the base form/acid form ratio by a factor of 10 at the half equivalence point.

The species distribution coefficients, α_0 (the fraction of acetic acid in the protonated form) and α_1 (the fraction of acetic acid in the deprotonated form), are uniformly 0.500000... across the entire surface as well. This is consistent with the mass action law (eq 3.2). At pH = 7.00, the equilibrium in to being upset and the ratio of base form to acid form is always 1.00000.... so the log term disappears. Dilution does not affect the pH.

3.7 pH topo surfaces for polyprotic acid titrations

The pH topo surfaces for polyprotic acids have the same types of features, cliffs, plateaus, and ramps, just more of them. Figure 3.7, for example, displays the pH topo surface for the titration

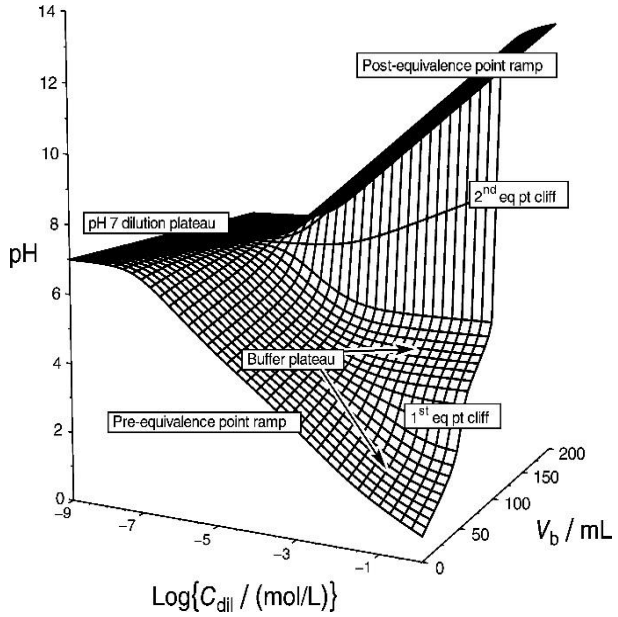

Figure 3.7. The pH surface for a 100 mL sample of the diprotic oxalic acid (HOOCCOOH).

and dilution of diprotic oxalic acid. The modeled surface is based on a K_{a1} of 5.6×10^{-2} (pK_{a1} =1.252) and a K_{a2} of 5.42×10^{-5} (pK_{a2} of 4.266). The first K_a is so low that oxalic acid is already missing most of its first titratable proton when initially dissolved in water. This leads to no initial point cliff being observed as it was for acetic acid. Note that there are two equivalence point cliffs, one for each of the two protons that can react with NaOH. Unless successive pK_a's are well separated, the equivalence point breaks are small. Thus, the first equivalence point cliff for

oxalic acid is not dramatic because the difference between pK_{a1} and pK_{a2} is only 3.14. The first equivalence point cliff begins diminishing at about log C_{dil} = −2. Recall that the extent of buffer plateaus is related to the pK_a of the acid form. Because the pK_{a1} for oxalic acid is so low, its ability to buffer against dilution has essentially already been exceeded by simply dissolving it in water (see pK_a = 1 trace in Figure 5). The buffer plateau associated with the pK_{a2} of 4.266 extends to about log C_{dil} = −5, as predicted from Figure 6. While oxalic acid can be modeled at a concentration of 1.0 M, in reality, a saturated solution in water at 25 °C is about 0.1 M. Thus, in experimental settings, the first equivalence point break will always be small. The second equivalence point break extends all the way to the pH 7 dilution plateau. This happens for any system for which the pK_{a2} associated with the break is within the range of 4−7. An example of the triprotic pH topo surface for L-histidine dihydrochloride is presented in Figure 3.8. The K_a's used in its calculation were 2.2×10^{-2}, 9.5×10^{-7}, and 8.3×10^{-10} (or pK_a's of 1.7, 6.02, and 9.08, respectively). It shares similar features to the oxalic acid topo surface up to the second equivalence point break. It has no initial point cliff and essentially no buffer plateau for the first proton. The first equivalence point break is more pronounced than that of oxalic acid because the difference in pK_{a1} and pK_{a2} is 4.32, more than one unit larger.

The only new feature seen with the L-histidine dihydrochloride surface is a third equivalence point above pH 7. The third buffer plateau (pH = pK_{a3} = 9.08) begins to degrade before the 10^{-3} level on the log Cdil axis. In this instance, $K_{b1} \gg K_{a3}$ so the diluent water is driving the hydrolysis reaction to reprotonate the his^{2-} species. From log C_{dil} values of −3 to −7, mass action effects from diluent water drive the protonation of Hhis− and converts it to H_2his.

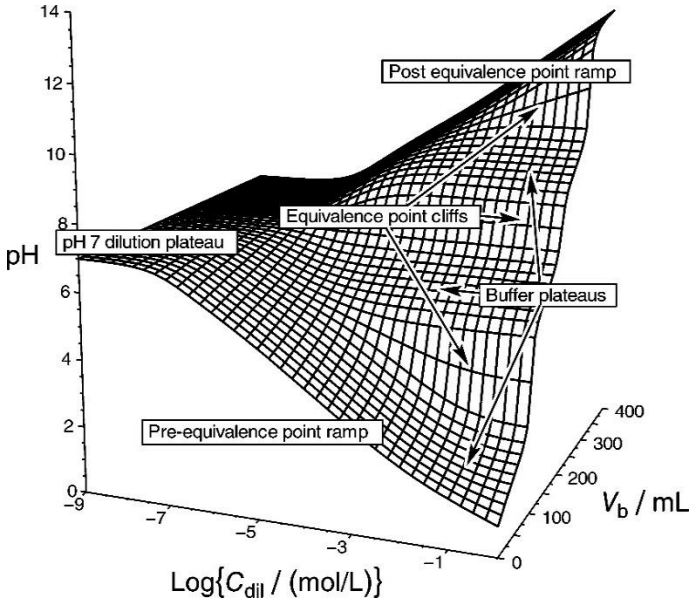

Figure 3.8. The pH surface for a 100 mL sample of the triprotic L-histidine dihydrochloride ($C_6H_9N_3O_2 \cdot 2HCl$).

At these alkaline starting pHs, very little H_2his is present to dissociate in opposition. From alpha species distribution calculations, the pH 7 dilution plateau shows a mixture that is roughly 90% Hhis− and 10% H_2his. The pH TOPO software permits one to easily illustrate conditions under which equivalence point breaks will be weak or unseen. This can happen when: (1) successive pK_a's are spaced at less than 3 orders of magnitude; (2) a pK_a is less than 3 pH units from the initial point; or (3) when the final pK_a is close to the pH of the titrant base. This is illustrated in the Supporting Information for case 1 in the pH TOPO surface for citric acid. A good example of case 2 is found in sulfuric acid. A good example of case 3 is present in the phosphoric acid surface.

3.8 Conclusions

A 3-D visualization of pH topo surfaces on the titration and dilution composition grid helps draw out subtle aspects of acid−base chemistry that might otherwise be overlooked. It converts a myriad of tedious calculations into a single, easy-to-understand picture. Students are much more likely to grasp difficult concepts from an image than they are from an abstract equation. This is especially true with regard to how dilution influences the pH of a system. The software provided in the macro-enabled Excel worksheets make it possible for students to EASILY view pH topo surfaces for a multitude of acids. All a user needs to supply here are K_a values. A few seconds later a complete pH topo surface is displayed. For advanced students,$[H_3O^+]$ and the associated pH values for every grid point can be examined in detail. For example, one can demonstrate the poor equivalence point breaks that correspond to the first two protons in citric acid by entering 7.44×10^{-4}, 1.73×10^{-5}, and 4.02×10^{-7} as $K_{a'}$s on the triprotic acid worksheet and then pressing Control+Shift+T. A few seconds later the topo surface will morph to one that has a broad ramp leading up to only a single perceivable equivalence point cliff. A particularly nice outcome of the pH surface approach is a visual demonstration of the limitations for the Henderson− Hasselbalch equation. The boundaries of the plateau portions of the surfaces denote where assumptions in the classical equation are breaking down. By noting that buffer plateaus persist on dilution to an extent that is a function of their $pK_{a'}$s is not a result that is easily seen in just looking at the equation itself. All surfaces for this paper were modeled assuming that the diluent was pure water at pH 7.0. In reality, obtaining and maintaining a reservoir of water at pH 7.0 is extremely difficult unless you isolate the system in a CO_2-free atmosphere. Many of the points raised here

would need to be modified if one used a typical surface water at pH 8.0 as the diluent or meteoric rainwater at pH 6.0. But with an understanding of the trends illuminated here, reasonable predictions of the changes would be rather straightforward. We hope that the pH topo program begins to replace the JCE Software titration curve software that is no longer available.

3.9 Associated content

Supporting information

Suggested timing and uses of topos in lecture; PowerPoint slides to use in the classroom; suggested worksheets; extensions into laboratory activities; an Excel spreadsheet with embedded macros that will allow the reader to reproduce all pH surfaces discussed here as well as allowing them to create a pH surface for any other mono-, di-, or triprotic acid. This material is available via the Internet at http://pubs.acs.org.

References

1. Cracolice, M.S. and Peters, E.I., *General Chemistry: An Inquiry Approach, Second Semester*, Cengage Learning, Mason, OH, 2009.
2. Chang, R.; Goldsby, K.A., *Chemistry,* 11 ed., McGraw-Hill, Columbus, OH, 2013.
3. Brown, T.E.; LeMay, H.E.H.; Bursten, B.E.; Murphy, C.; Woodward, P.; *Chemistry: The Central Science,* 12 ed., Pearson Prentice Hall, Upper Saddle River, NJ, 2013.
4. Abraham, M.R.; Pavelich, M.J *Inquiries into Chemistry,* 3 ed., Waveland Press, Long Grove, IL, 1999.

5. Nelson, J.H.; Kemp, K.C. *Chemistry: The Central Science, Laboratory Experiments,* 10 ed., Pearson Prentice Hall, Upper Saddle River, NJ, 2006.
6. Sørensen, S.P.L. *Meddelelsierfra. Carlsberg Laboratoriet* **1909**, *8*, 1-168.
7. Myers, R.J. *J. Chem. Educ* **2010**, *87*(1), 30-32.
8. Sillén, L.G. *Acta Chem. Scand.* **1962**, *16* (1), 159-172.
9. Ramette, R.W. *J. Chem. Educ.* **1989**, *2B* No. 2.
10. Ramette, R.W. *J. Chem. Educ.* **1998**, *75*(11), 1504.
11. Gutz. I.G.R. http://www2.iq.usp.br/docente/gutz/Curtipot_.html accessed 6/19/13.
12. Waser, J. *J. Chem. Educ.* **1967**, *44*, 274-276.
13. de Levie *J. Chem. Educ.* **1993**, *70*(3), 209-217.
14. Martell, A.E.; Smith, R.M. *Critical Stability Constants*, Plenum Press, New York, 1974.
15. Bates, R.G. *Anal. Chem*. **1954**, *26* (5), 871-874.
16. Butler, J.N. *Ionic Equilibria: Solubility and pH Calculations*, John Wiley, New York, 1998.
17. Harris, D. *Quantitative Chemical Analysis*, 8 ed., W.H.Freeman, New York, NY, 2011.
18. Clark, R.W.; White, G.D.; Bonicamp, J.M.; Watts, E.D. *J. Chem. Ed.* **1995,** *72*(8),746-750,.
19. Hasselbalch, K. A. *Biochemische Zeitschrift* **1917,** *78*, 112–144.
20. Guldberg, C.M.; Waage, P. *L. prakt. Chem.* **1879**, *19*(2), 69-114.
21. de Levie, R. *Chem. Educator* **2002**, *7*, 132-135.

Chapter 4
3-D Surface Visualization of Buffer Capacity Topos: Buffer Ridges, Equivalence Point Canyons and Dilution Ramps

4.1 Introduction

Buffers have two characteristics: 1) the pH that they establish and stabilize, and 2) the capacity to maintain that pH against additions of strong acids or bases and dilution. These are analogous to the two characteristics of energy measurements: 1) temperature, and 2) heat. A system's pH and temperature are intensive properties that are independent of sample size[1]. A thimble full of water and a lake full of water can both exhibit the same pH and temperature but will undoubtedly differ greatly in their total buffer capacity and heat content. This is because buffer capacity and heat are extensive properties that depend on sample size[2]. In practice, however, buffer capacity is converted to a "per liter" basis so that comparisons between systems can be made.

Buffer capacity is an important concept for students who need a comprehensive understanding of chemistry fundamentals – especially those majoring in chemistry [2-4], biochemistry [5-6] and geochemistry [7]. Buffers maintain the pH necessary for chemical analyses, physiological reactions and aquatic ecosystem health. As soon as a system's buffer capacity is exceeded, it no longer will have its pH stabilized at the desired level. Frequently, buffer capacity is at the heart of a situation. For example, the administration of IV fluids for patients who are in respiratory distress boosts the buffer capacity of the blood and prevents it from dropping too low [8]. The vulnerability of a freshwater lake hinges on its natural buffer capacity to counteract atmospheric deposition of sulfuric and nitric

acid from acid rain [9]. The accuracy of commercial buffers can be invalidated if the solution is diluted too far.

An earlier paper was aimed at generating 3-D surface "topos" for a system's pH behavior against additions of strong acid or base and dilution [3]. This paper adds new 3-D surface topos for buffer capacity behavior. It offers downloadable spreadsheet software that generates a clear visual connection between pH changes during a titration and the associated buffer capacity at each point. It should help beginning students see the inter-relationship between a buffer's two characteristics – the pH it establishes and its capacity to maintain it. At the same time, it can provide some new insights into buffer behavior that are of interest to more advanced students. Instructors and students in upper-division and graduate-level analytical, biochemistry and aquatic chemistry courses will find it particularly useful.

4.2 Computational approach

The quantitative expression of buffer capacity was introduced by Van Slyke in 1922 [4,9]. It addressed buffer capacity in a sample of a given volume with respect to the addition of strong base or strong acid. Since then, numerous papers have refined buffer capacity calculations. Bates (1954) defined buffer capacity on the basis of the pH change when the volume of a sample was diluted by a factor of two [10]. Olson (1977) graphically portrayed dilution conditions in a system where the buffer capacity of a sample was controlled by the contributions from the diluent water[11]. Michlowski and Parczewski (1978 Chemia Analityczna) tracked the influence of dilution on buffer capacity when performing experimental procedures that changed sample volumes[12].

Beginning in 1989, computer software to calculate buffer capacities became widely available. Ramette's DOS-based program entitled "The Acid-Base Package" was featured as a Journal of Chemical Education Software item[13]. A year later, Lambert created a Turbo-Pascal program BUFCALC[14]. In 1998 Ramette updated his earlier program to the Windows 95 environment and renamed it "Buffers Plus"[15]. Unfortunately, these comprehensive buffer calculation software packages are no longer available. At this writing, CurTiPot, a collection of spreadsheet programs that do many of the same functions, is provided as a free download from I.G.R. Gutz[16].

This paper introduces 3-D visualization of how buffer capacities change as the result of two very common procedures – titrations and dilutions. A composition grid is established with "volume of NaOH added" on the x-axis (as for a typical titration of an acid sample) and following the overall dilution of the system (log C_{dil}) on the y-axis. Plotted above this grid on the z-axis are the buffer capacities associated with each pair of grid coordinates. The 3-D surface topo that results depicts how these two variables affect buffer capacity. The macro-enabled Buf Cap Excel spreadsheet is provided as Supporting Information through which the reader can modify both the pH and buffer capacity topos to represent any desired mono-, di- or triprotic acid system by simply supplying the appropriate K_a value(s). The values for K_a's are taken from Martell and Smith's Critical Stability Constants.[17]

The buffer capacity calculations displayed in this paper assume that the analyte is a 100.0 mL aliquot of acid. For the dilution axis, the acid analyte and NaOH titrant are assigned identical concentrations, so equivalence points always occur at 100-mL intervals. For a monoprotic acid, the x-axis ranges in 5-mL steps from 0 to 200 mL, terminating 100 mL beyond the equivalence point. The y-axis is logarithmic and provides the starting concentration for both the analyte and titrant, C_a^0 and C_b^0. These values begin at 1.0 M and are reduced in 0.25 log-unit increments until a final concentration of 1×10^{-9} M is reached. In plots the dilution axis is labeled as "log C_{dil}" but in the mathematical equations below it corresponds to yC_a^0 where y is the dilution factor. The two axes establish a base that is 41 x 37 = 1517 total grid points.

At each grid point a polynomial equation was solved for the $[H_3O^+]$ to 16 significant figures. The polynomial forms used for strong acids, monoprotic acids, diprotic acids and triprotic acids are widely available in the literature[7]. The $[H_3O^+]$ is simply converted to a pH value to create a pH titration topo surface. Computation of the associated buffer capacity is not so easily accomplished. An equation was derived for the volume of base added as a function of $[H_3O^+]$ and the dilution factor (y) (Eq 4.1). The molar concentrations of the acid analyte and the base titrant before dilution, when y = 1, were C_a^0 = 1 M and C_b^0 = 1 M, specifically. Also appearing in the expression are K_w (the auto-dissociation constant of water), K_a (any acid dissociation constants), and V_a (the volume of acid with which each titration slice always starts). For a monoprotic weak acid, the equation is:

$$\mathcal{V}_b = \mathcal{V}_a \frac{\left(\frac{\mathcal{K}_w}{\left[H_3O^+\right]} + \left(\frac{\mathcal{K}_a}{[H_3O^+] + \mathcal{K}_a} \right) y C_a{}^0 - \left[H_3O^+\right] \right)}{\left(\left[H_3O^+\right] + y C_b{}^0 - \frac{\mathcal{K}_w}{\left[H_3O^+\right]} \right)} \qquad (4.1)$$

Traditionally, buffer capacity, β, Is a measure of how many moles of acid or base can be added to 1 liter of buffer until the pH changes by one unit. Mathematically, it is usually expressed as a differential [4] (Eq 4.2):

$$\beta = \frac{d\mathcal{C}_b}{d\text{pH}} = -\frac{d\mathcal{C}_a}{d\text{pH}} \qquad (4.2)$$

Where $\mathcal{C}_b$ and $\mathcal{C}_a$ are in mol/L. (Note that the $C_a{}^0$ and $C_b{}^0$ in Eq 4.1 and other equations in this chapter refer to the concentration of the titrant and analyte, NOT the buffer capacity definition in Eq 4.2.)

To relate each point in the titration curve to its corresponding buffer capacity, Eq 4.1 is first differentiated with respect to $[H_3O^+]$ (Eq 4.3)

$$\frac{\partial \mathcal{V}_b}{\partial \left[H_3O^+\right]} = \mathcal{V}_a \left(\left(\frac{1}{\left[H_3O^+\right] + y C_b{}^0 - \frac{\mathcal{K}_w}{\left[H_3O^+\right]}} \right) \left\{ \frac{-\mathcal{K}_w}{\left[H_3O^+\right]^2} + K_a y C_a{}^0 \left(\frac{-1}{\left(\left[H_3O^+\right] + \mathcal{K}_a \right)^2} \right) - 1 \right\} - \frac{\left(\frac{\mathcal{K}_w}{\left[H_3O^+\right]} + \left(\frac{\mathcal{K}_a}{[H_3O^+] + \mathcal{K}_a} \right) y C_a{}^0 - \left[H_3O^+\right] \right)}{\left(\left[H_3O^+\right] + y C_b{}^0 - \frac{\mathcal{K}_w}{\left[H_3O^+\right]} \right)^2} \left(1 + \frac{\mathcal{K}_w}{\left[H_3O^+\right]^2} \right) \right) \qquad (4.3)$$

then modified with implicit differentiation (Eq4) to transform it with respect to pH

$$\frac{d\left[H_3O^+\right]}{d\ \text{pH}} = -2.303\left[H_3O^+\right] \qquad (4.4)$$

The traditional definition of buffer capacity of a solution is presented as a "per liter" basis. To achieve this, the final expression must convert V_a to a 1-liter volume. The ($1/V_a$) that appears as the first term in Eq5 accomplishes this. For example, because the Buf Cap TOPOS program uses a default value of 100 mL (0.1 L) as V_a, the program will multiply the raw buffer capacity it calculates by (1/0.1), or 10, to convert it to the 1 liter buffer capacity definition.

$$\beta = \frac{\left(\frac{1}{\mathcal{V}_a}\right) yC_b \partial \mathcal{V}_b}{\partial \, \mathrm{pH}} = -\left(\frac{1}{\mathcal{V}_a}\right) yC_b{}^0 \, 2.303 [H_3O^+] \mathcal{V}_a \left(\left(\frac{1}{\left[H_3O^+\right] + yC_b{}^0 - \frac{\mathcal{K}_w}{\left[H_3O^+\right]}} \right) \left\{ \frac{-\mathcal{K}_w}{\left[H_3O^+\right]^2} + \mathcal{K}_a yC_a{}^0 \left(\frac{-1}{\left(\left[H_3O^+\right] + \mathcal{K}_a\right)^2} \right) - 1 \right\} - \frac{\left(\frac{\mathcal{K}_w}{\left[H_3O^+\right]} + \left(\frac{\mathcal{K}_a}{[H_3O^+] + \mathcal{K}_a} \right) yC_a{}^0 - \left[H_3O^+\right] \right)}{\left(\left[H_3O^+\right] + yC_b{}^0 - \frac{\mathcal{K}_w}{\left[H_3O^+\right]} \right)^2} \left(1 + \frac{\mathcal{K}_w}{\left[H_3O^+\right]^2} \right) \right) \quad (4.5)$$

Note that Eq 4.5 does not include V_b as an independent variable through which to calculate β. Instead, we use the value of $[H_3O^+]$ that is specifically attached to a pair of grid-point coordinates, *i.e.*, $[H_3O^+] = f(V_b, y)$. The β's that emerge from this procedure are plotted as log β values above grid-points so that a wide range of magnitudes can be captured simultaneously into a single plot. (The complete set of V_b and β equations for strong, diprotic and triprotic acids can be found in the Supporting Information.)

The validity of all buffer capacity equations was checked by using the raw pH data to compute finite difference approximations to the differential expression using the factor of 10 to force the 1-L definition (Eq 4.6).

$$\beta = \frac{10\gamma C_b{}^0 \partial V_b}{\partial \text{ pH}} \cong \frac{10\gamma C_b{}^0 \Delta V_b}{\Delta \text{pH}} \quad (4.6)$$

The surface resulting from the finite difference procedure was essentially indistinguishable from the exact expression surface except at the initial point and at the equivalence point where the finite difference procedure cannot access these specific grid point values.

4.3 Titration curves and buffer capacities

Often, but not always, buffer capacity is discussed as part of explaining titration curves [18-20]. It is logical to describe how a titration curve's flat spots, buffer plateaus, behave (Figure 4.1). As more base titrant is added, the pH of a buffer plateau eventually begins to change more rapidly because the protonated form of the buffering agent is being depleted, i.e., the buffer capacity has been reached. A few more mL of NaOH will cause the pH to rapidly rise in an equivalence point break. A plot of buffer capacity (β) vs. pH often accompanies the discussion. This set of axes is not directly related to the titration curve itself but is shown because of the explicit definition of buffer capacity that relates it to a 1-pH unit jump (namely, Eq 4.2). Figure 4.2 illustrates this type of plot for the acetic acid system. It demonstrates that buffer capacity is essentially directly proportional to the concentration of the buffer components in the vicinity of the buffer's pK_a. Acetic acid's pK_a is 4.75, so β reaches a local maximum at pH = pK_a = 4.75. As will be seen in a later section, this direct relationship between buffer capacity and concentration is eroded under continuous dilution procedures. Sometimes the buffer capacity vs. pH curve is even positioned underneath or on top of a $\mathcal{C}_b$ vs pH curve to illustrate that the derivative of the $\mathcal{C}_b$ curve generates the buffer capacity profile of the β curve.

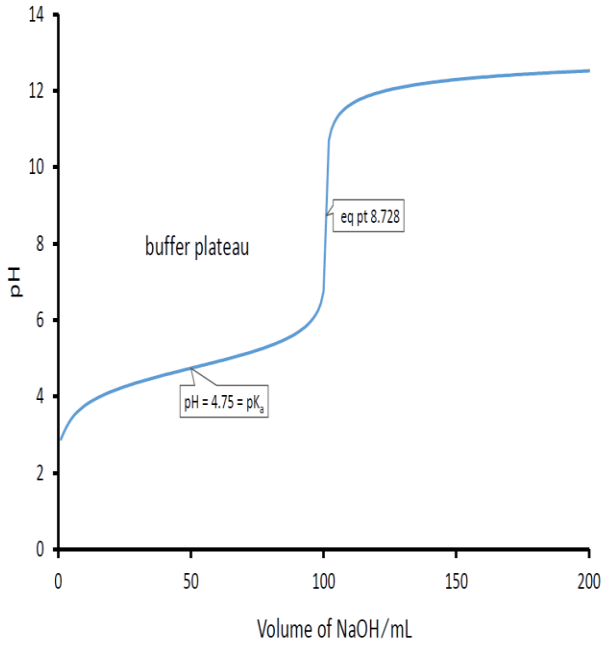

Figure 4.1. Traditional titration curve with buffer plateau and equivalence point labeled for 100 mL of 0.100 M acetic acid titrated with 0.100 M NaOH.

The same acetic acid system is used to illustrate this point in Figure 4.3. This representation also demonstrates that the maximum buffer capacity of acetic acid's buffer plateau is located at the spot where pH = pK_a = 4.75 and that the minimum buffer capacity occurs at the equivalence point where pH = 8.73. Although the $\mathcal{C}_b$ vs. pH trace is related to a titration curve (with the x- and y-axes interchanged), it does not permit the eye to associate the buffer capacity values point-for-point with the progress of a titration. Typically, data for this plot are generated by stepping at regular increments of pH, not by regular increments of volume of base added.

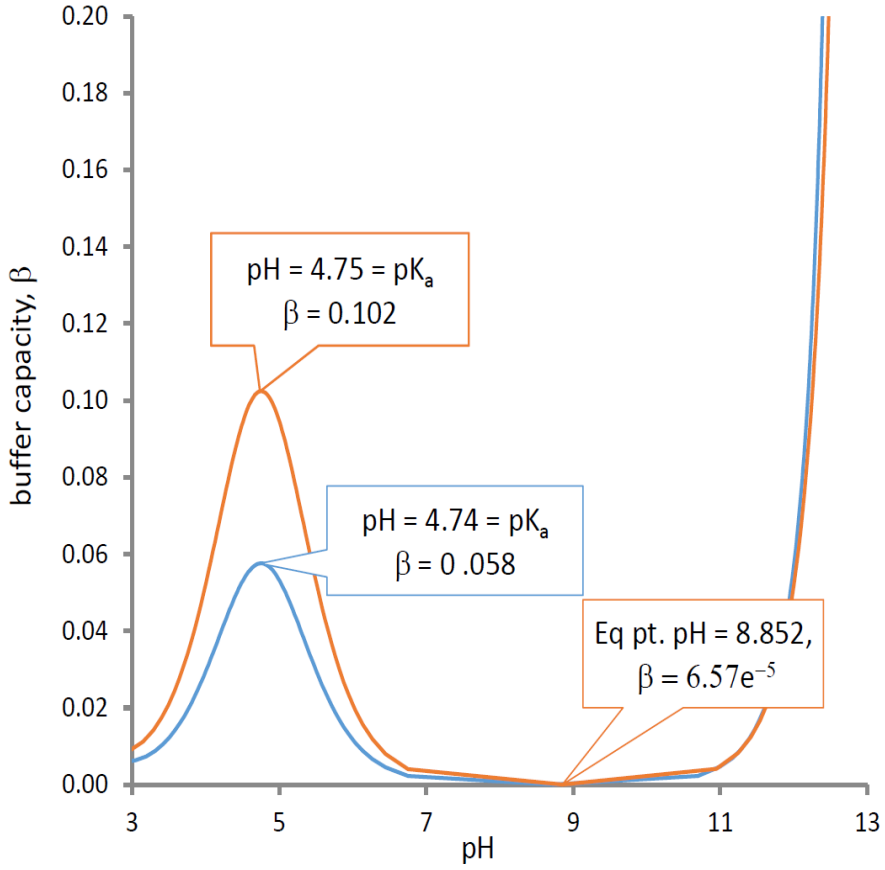

Figure 4.2. Buffer capacity vs. pH for acetic acid (pK_a = 4.75) at 0.1000 M and 0.1778 M concentrations.

With pH as a logarithmic x-axis, it is not possible to see the relationship between β and the linear volume of base added. To view this relationship directly, both pH and β must be plotted against "Vol of NaOH mL" as shown in Figure 4.4. A logarithmic y-axis is used to display both pH and β traces together.

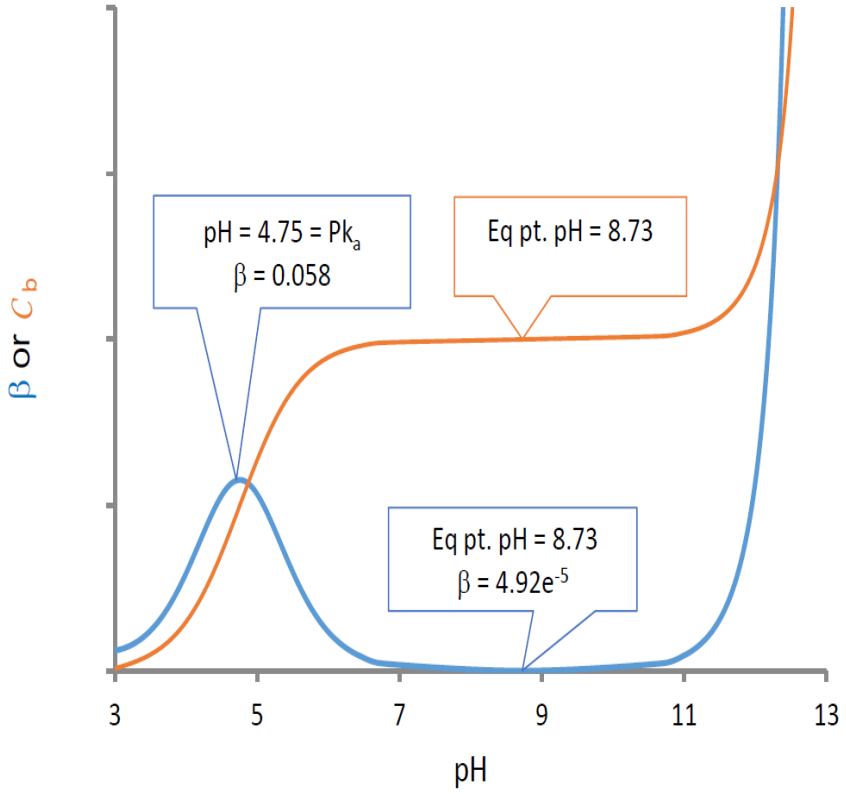

Figure 4.3. Buffer capacity, β, as the derivative of a C_b vs. pH curve.

Half-way to the equivalence point, the β-curve shows a maximum value at 50 mL that aligns with the pH trace at pH = pK_a = 4.75 for acetic acid. Note that the buffer capacity subsequently plunges to a minimum at the exact equivalence point, the same place where pH changes most dramatically. No comparable visual feature appears at the equivalence point in Figure 4.3 with the traditional graphic representation.

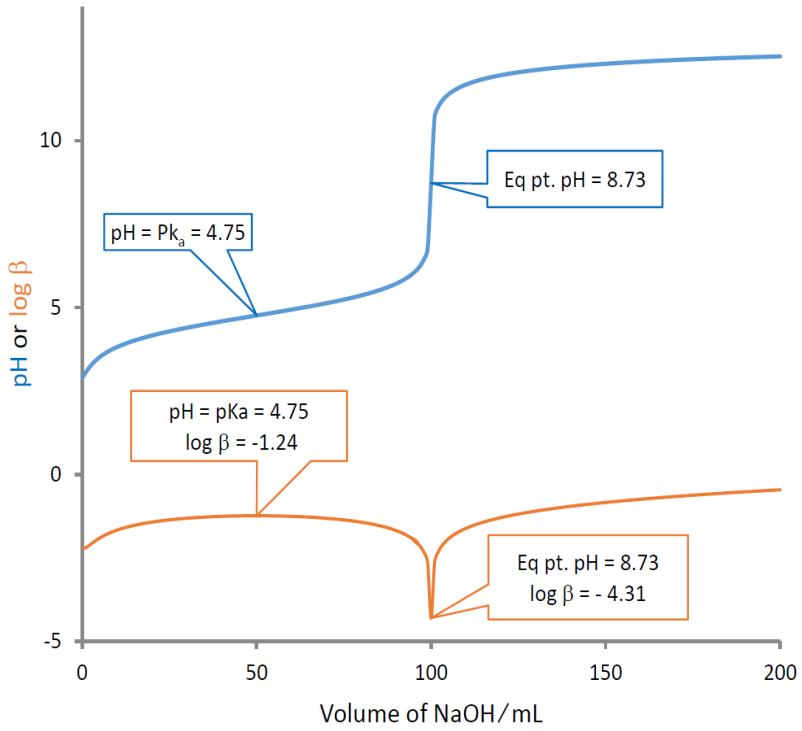

Figure 4.4. The relationship between buffer capacity and a titration curve for 100.0 mL of 0.100 M acetic acid titrated with 0.100 M NaOH.

4.4 pH and buffer capacity surfaces

A complete description of pH and buffer capacity behavior during acid-base titrations and dilution procedures can best be visualized by constructing 3-D topo surfaces above a V_b vs log C_{dil} composition grid. This is really just an extension of plots that have appeared in many previous discussions that show multiple traces based on concentrations. Figure 4.5 illustrates four concentration "slices" for both a titration curve (panel I) and the corresponding buffer capacity curves (panel II). If a multitude of dilution slices, 37 for the present paper, are stacked in the right manner, one can generate an overall topo trend surface. For example, the complete 3-D pH topo surface for acetic acid appears as Figure 4.6 [3]. Each

slice represents a 100 mL acid sample titrated with a NaOH solution at same concentration.

Panel I

Panel II

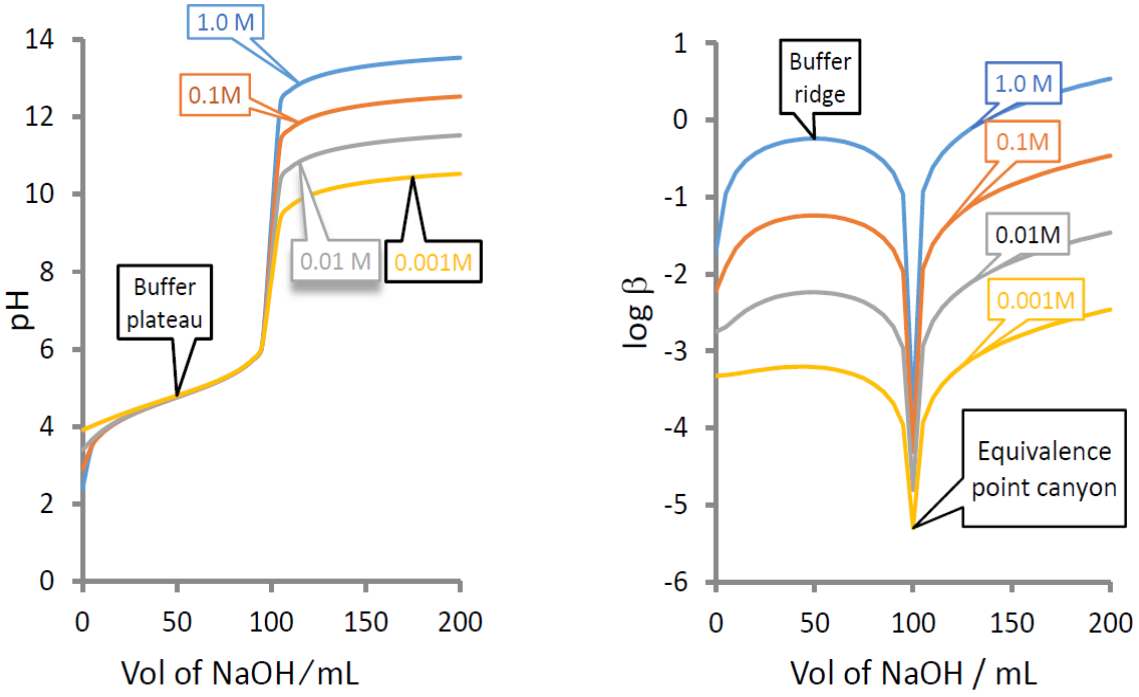

Figure 4.5. Multiple "slices" depicting dilution of the system. Panel I – acetic acid pH. Panel II – acetic acid buffer capacity

The right-hand edge of the surface is a profile of the first titration curve slice of Figure 4.5, Panel I. As one moves to the left along the log C_{dil} axis, progressively more dilute conditions are encountered. For the most concentrated system (i.e., the line that forms the right-hand edge of the surface), 1.0 M CH_3COOH is being titrated with 1.0 M NaOH. Successive lines in the dilution direction indicate repeating the titration with both the acid and base concentrations adjusted

identically. Thus, at the most dilute point (the left-hand edge of the surface), 1.0 x 10^{-9} M CH_3COOH is being titrated with 1.0 x 10^{-9} M NaOH.

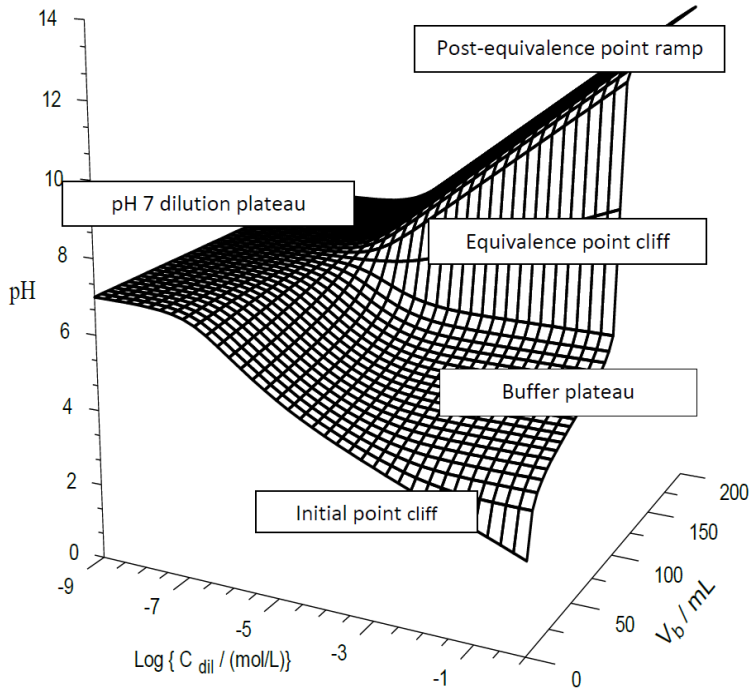

Figure 4.6. The acetic acid pH topo surface based on 100 mL aliquots of acid being titrated [3].

With the entire pH topo surface to view, one can discern a series of ramp, cliff and plateau features. Ramps are associated with grid regions where dilution alone dominates the system's pH. Cliffs occur at initial and equivalence points during a titration procedure. Plateaus are indicative of situations in which pH is somewhat stable against addition of NaOH titrant or dilution, i.e., buffer zones and extreme dilution conditions. These three surface features have been discussed in detail in a previous paper [3]. 3-D topo surfaces can also be generated for associated buffer capacities. Figure 4.7 introduces two varieties of buffer capacity surfaces.

Panel I is a linear buffer capacity surface that relates to the traditional pH vs. buffer capacity plots. Note, this surface is not plotted above a composition grid. Instead, it uses a system parameter, pH, as one of the axes rather than the concentration of a component solution. What is shown here for the first time is the buffer capacity vs. pH extended systematically in the dilution direction. Because the dilution axis is linear, so too is the buffer capacity axis. It is only feasible to see information from dilutions over one order of magnitude on this C_{dil} axis.

Panel II presents a logarithmic dilution axis, log C_{dil}. This corresponds to exactly the same (V_b, log C_{dil}) composition grid as the acetic acid pH topo of Figure 4.6. A logarithmic buffer capacity axis, log β, is employed to draw out values that cover many orders of magnitude of dilution. Note, however, that a different plotting angle is employed than in Figure 4.6 to promote easy viewing of as many surface features as possible. The linear buffer capacity surface essentially shows only one feature of the buffer system, namely, that buffer capacity is linearly related to the concentration of the buffer component. The height of the buffer capacity "ridge" at 4.8 (the grid point closest to the half-equivalence point) is 0.572714 mol/L for a 1.0 M buffer content and 0.286375 mol/L for a 0.5 M buffer content, a ratio of 1.99987:1. The "wings" at either edge of the linear surface represent additions of concentrated NaOH or HCl that are necessary to generate specific high or low logarithmic pH grid values. They are not related to the buffer component itself. They show large buffer capacities because of "chemical inertia" that must be overcome once the concentrated NaOH or HCl present under these conditions

Panel I

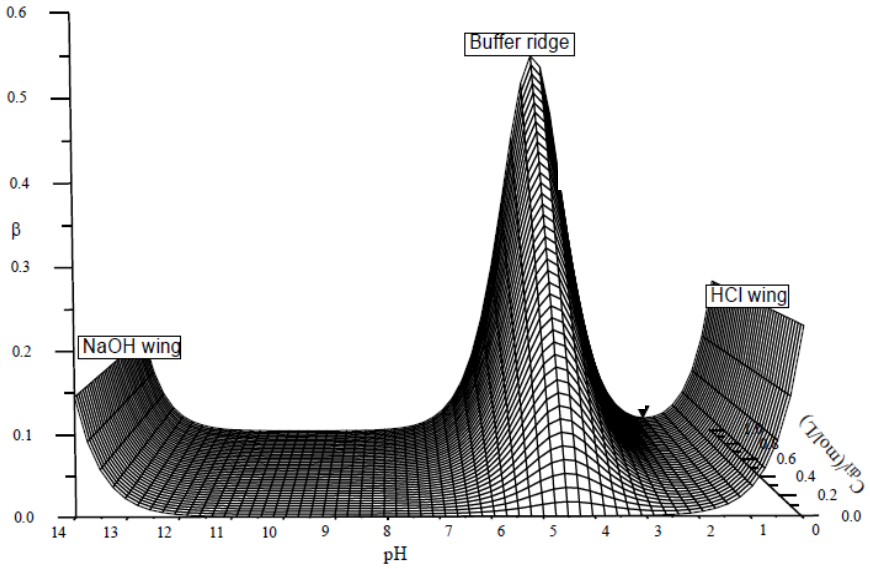

Panel II

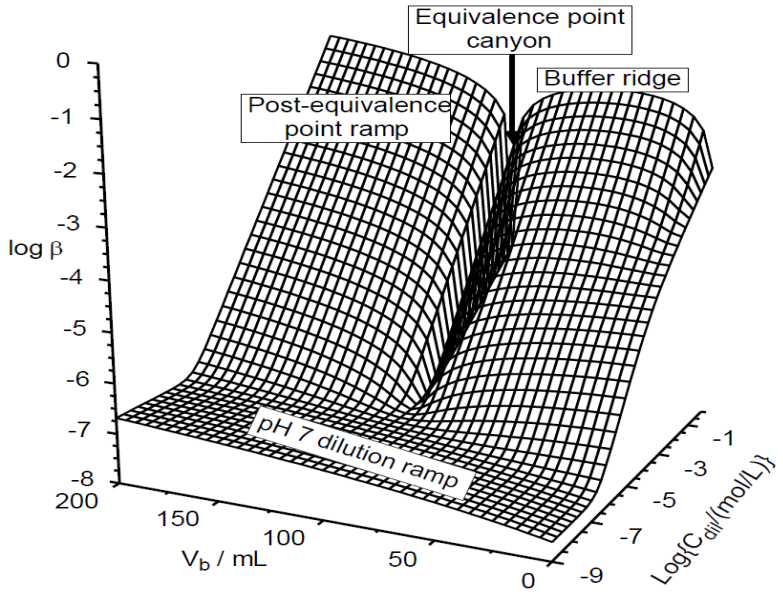

Figure 4.7. The buffer capacity topo surface for the same acetic acid system of Figure 4.6. Panel I. Linear; Panel II. Logarithmic.

The linear surface contains no feature that corresponds to a titration endpoint. The endpoint break is the indistinguishable lowest spot on the flat valley floor between the buffer ridge and the NaOH wing. Note in Figure 3 the location of the equivalence point labeled on the "sideways" plotted titration curve. The derivative buffer capacity curve is essentially flat beneath it between pH values of 7 and 10.5. Neither is there any surface features to show where the linear relationship between buffer capacity and buffer component concentration breaks down due to dilution-driven dissociation. The linear dilution scale compresses much interesting buffer behavior into the last grid interval. This only becomes visible if one expands the last linear interval with a logarithmic scale.

Panel II uses a logarithmic dilution scale to draw out additional buffer capacity behavior. For viewing clarity, the surface is oriented differently than the pH topo. The back edge of the surface is the most concentrated (1 M) "slice" for the buffer capacity topo (see top curve in Figure 4.5, Panel II). The most dilute conditions are found at the front of the surface. The logarithmic z-axis accommodates a wider range of buffer capacities. Most previous work with buffer capacity has only explored dilution to a minor extent [11] a factor of two or at most slightly more than an order of magnitude. In Figure 4.7, dilutions of eight orders of magnitude are displayed.

Logarithmic buffer capacity surface features fall into three general categories: ramps, ridges and canyons. Ramps are associated with pseudo-buffer situations where changes in conditions are mostly physical dilution processes as opposed to acid-base interactions[2]. Ridges correspond to true buffer situations where the ratio of acid to base forms plays a controlling role. Canyons represent

the equivalent point breaks and are the lowest buffer capacities observed during a titration.

There is a steep rise toward top of the “buffer ridge” from the initial point. Then, as one moves half-way to the equivalence point, the buffer capacity increases to a maximum value along the crest of the buffer ridge. The pH is quite stable here. Near the equivalence point, the system’s pH is highly sensitive to the addition of more NaOH and at the exact equivalence point, buffer capacity plunges to its lowest value in the bottom of the “equivalence point canyon”. Finally, the buffer capacity climbs up to high values as the system is essentially dominated by excess NaOH beyond the equivalence point. The extra NaOH adds “chemical inertia’ to changes in the system’s pH.

Moving in the log C_{dil} direction, all slices slope downwards toward the “pH 7 dilution ramp”. This is a manifestation of buffer capacity being an extensive property of the system, one that is directly proportional concentration. At half-equivalence points on buffer capacity topos there are no “buffer plateaus” extending in the dilution direction as are seen in the pH surfaces. The pH depends on the ratio of the buffer’s base to acid form whereas buffer capacity depends on concentrations. Dilution does not initially alter the ratio of base to acid but it does steadily decrease concentration. Eventually, dependent on the K_a of the buffer’s acid form, dilution will also shift the base to acid ratio and the pH “buffer plateau” tilts toward a pH of 7 [3].

When dilution reaches about 10^{-6} M, the auto-dissociation of water starts providing almost equivalent amounts of H_3O^+ and OH^- as the buffering agent itself. Beyond 10^{-7} M, the H_3O^+ and OH^- of water overwhelms what little buffering agents are present. Dilution no longer changes the buffer capacity because it is

the diluent itself that is determining it. It is not possible to dilute water with water. Thus the buffer capacity slices in the dilution direction become essentially horizontal beyond 10^{-6} M.

The entire "pH 7 dilution ramp" slopes gently upwards in the V_b direction. This is another instance in which the "chemical inertia" of the system is at play. Even though the NaOH titrant being added is very dilute, it still can slowly accumulate sufficiently to raise the pH a slight amount. For comparative purposes, it is useful to look at the pH and buffer capacity surfaces for a strong acid such as HCl. Figure 4.8 panel I displays the HCl pH topo. Figure 4.8 Panel IIa and 4.8 Panel IIb both hold the log buffer capacity topo and the linear buffer capacity surface respectively. Note that the log buffer capacity topo shows a distinct feature for equivalence point where buffer capacity plummets. The linear surface shows no internal feature; it simply has the HCl and NaOH wings at either edge.

Buffer capacity surface features correlate to topo features seen on the pH surface. The "initial point cliff" on the pH topo manifests itself as the rapid rise to the "buffer ridge" on the buffer capacity topo. This makes logical sense because wherever the pH is changing quickly, buffer capacities will be small. Whenever pH stabilizes, buffer capacities will increase. By the time a few 5-mL aliquots of NaOH have been added to the starting solution of acetic acid, a reasonably stable buffer system has been established.

Panel I

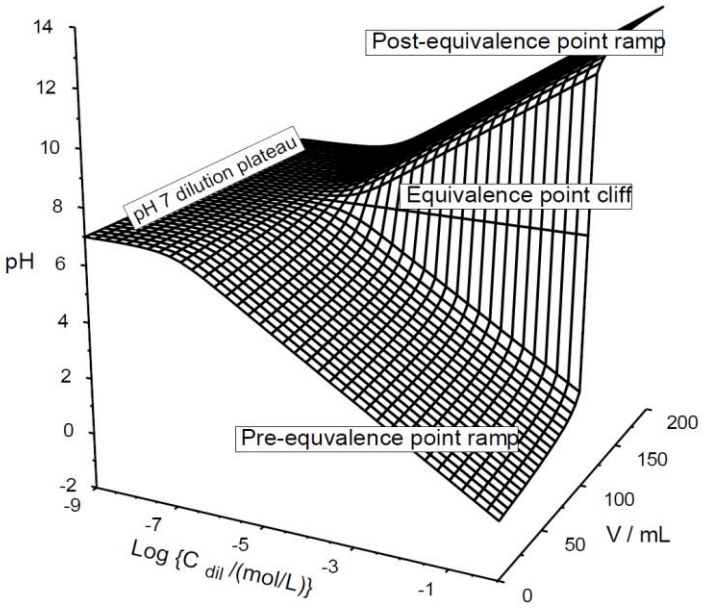

Panel II a

Panel IIb

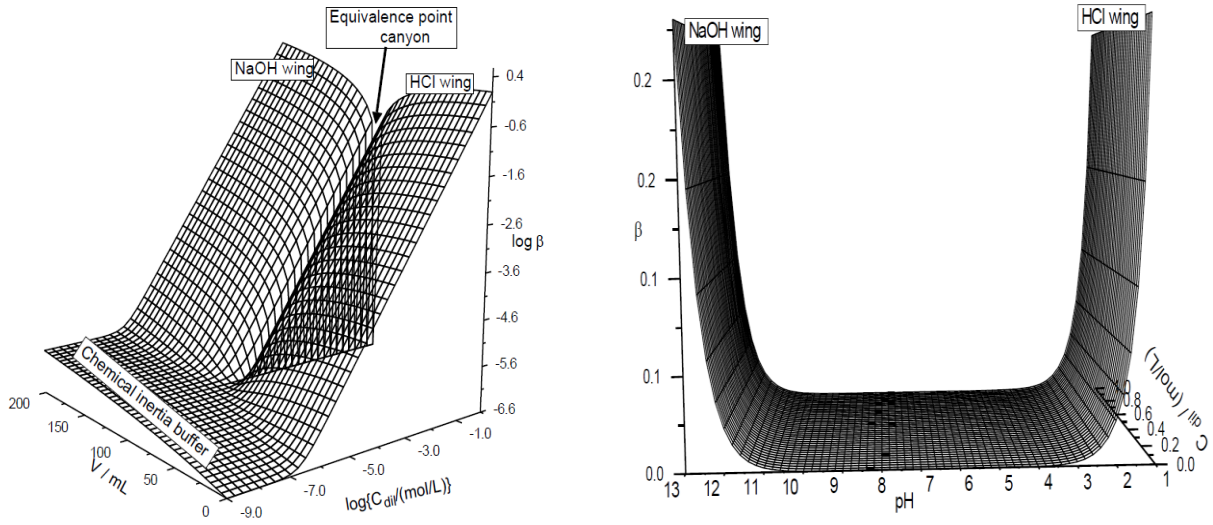

Figure 4.8. Trend surfaces for strong acid, HCl. Panel I – pH topo surface, Panel IIa – log buffer capacity topo, Panel IIb – linear buffer capacity surface.

4.5 Effect of pK_a and dilution on buffer capacity

The size of the initial point cliff is contingent on the pK_a of the buffer – the higher the pK_a of the buffer, the more dramatic the initial point cliff. The higher the pK_a of an acid is, the more dramatic the rise to its buffer ridge crest, too. This is illustrated in Figure 4.9. Shown are three traces of the buffer capacities during the titration of a 0.100 M acid solution with 0.100 M NaOH. HCl, a strong acid with a pK_a of about -6.0, has no initial point cliff. Correspondingly, there is no rise to a buffer ridge on its trace, the solid line in the figure. In fact, the buffer capacity is at a maximum at the initial point and then systematically declines until the equivalence point is reached. HCl exhibits pseudo-buffering behavior[2]. The dashed line (seen only at the beginning of the trace and in the middle of the equivalence point canyon) is for acetic acid with a pK_a of 4.75. A rise of about one order of magnitude is seen between the buffer capacity of the initial solution at a pH of 2.38 and the maximal value at 50 mL at a pH of 4.75. Finally, the dotted line is for phenol, a very weak acid with a pK_a of 9.98. The rise to the buffer ridge crest is about four orders of magnitude. The pH that it stabilizes as a buffer (9.98) is much higher than its starting pH value of 4.98. One insight that comes from observing the buffer capacity for titrations is that the pre-equivalence point buffer capacities are almost identical for all weak acids. While acetic acid and phenol differ greatly in their strength, once the initial point rise has occurred and a buffer ratio has formed, their traces lie atop one another. They have the same ability to consume added NaOH while maintaining the current pH value. The difference is that acetic acid will maintain the pH near 4.75 (its pK_a) while phenol will maintain the pH around 9.98. Acid is acid. As long as it will react with NaOH, there is no buffer capacity difference that is significant.

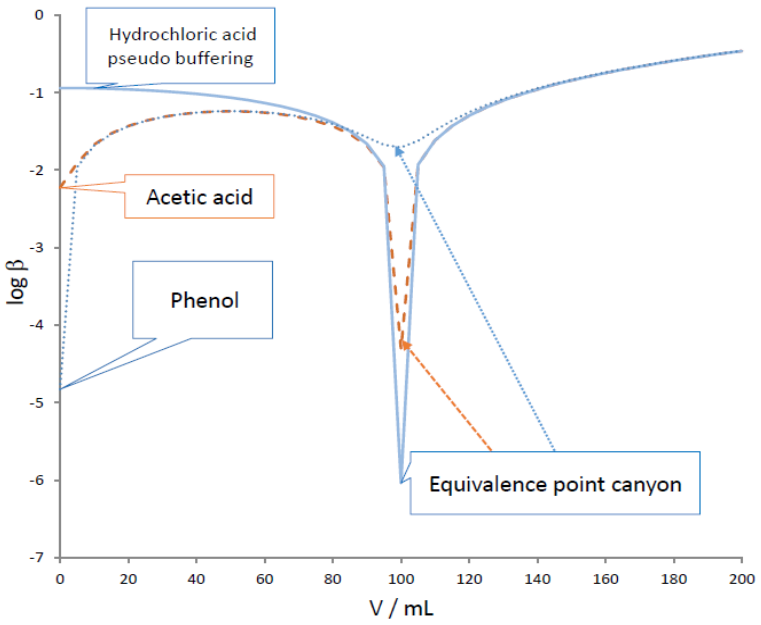

Figure 4.9. The effect of pK_a on the buffer capacity curve of three acids at 0.100 M.

The HCl buffer capacity tracks above the weak acid traces until about 60-mL of NaOH have been added. It is a "pseudo-buffer" situation, not really buffering controlled by a ratio of acid to base forms. Beyond the equivalence point, the traces for all three systems are superimposed on one another. They all exhibit the pseudo-buffer capacity of a NaOH solution. Note that the depth of the equivalence point canyon is dependent on the size of the equivalence point break. HCl's buffer capacity plunges much more than the two weak acids.

A second point worth making is that the initial point rise disappears as one goes to successively more dilute systems. Comparative plots for three acids are shown in Figure 4.10 hydrochloric, formic and acetic acids. At higher concentrations weak acids display differing amounts of dissociation according to their strength. In the upper group of traces for 0.100 M systems, acetic acid

displays the lowest initial buffer capacity since it is the weakest of the three that are plotted. It experiences the greatest jump between its initial pH (2.38) and its optimal buffered pH (4.75). The bigger the pH jump, the lower the buffer capacity. Formic acid undergoes a smaller pH jump from its initial pH (1.88) to its optimal buffer pH (3.745). Hydrochloric acid exhibits only pseudo-buffering. It's buffer capacity decreases monotonically with the addition of NaOH. The second tier of traces is for the three systems at 1.00 x 10^{-3} M. The dilution has cause both formic and acetic acids to dissociate some more. In fact, formic acid is so sufficiently dissociates that its buffer capacity trace is scarcely distinguishable from that for hydrochloric acid. For all intents it now, too, exhibits pseudo-buffering; there is no buffer ridge present. By the time the three systems are all diluted to 1.00 x 10^{-5} M, the weak acid buffer capacity curves fall on top of that for HCl. Sufficient dissociation has made their buffer capacities practically equivalent and all of a pseudo-buffering nature.

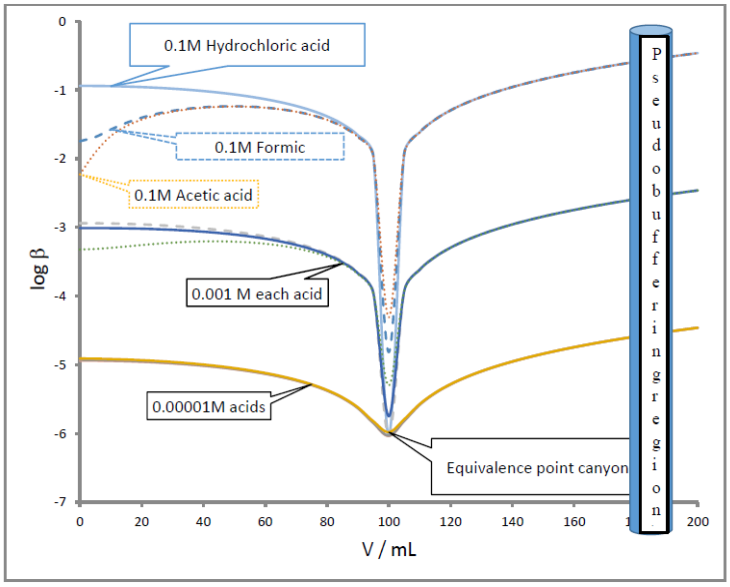

Figure 4.10. The effect of dilution on the buffer capacity curve for three acids at 0.100 M, 0.00100 M and 0.0000100 M.

4.6 Buffer capacity surfaces for polyprotic systems

Buffer capacity topos for polyprotic species can display multiple equivalence point canyons and buffer ridges. The depths of the equivalence point canyons are dependent on the size of the equivalence point breaks for the associated pH titration surface. Unless there is a difference of about three orders of magnitude in the pre- and post-equivalence point pHs, there will only be a shallow canyon on the buffer capacity surface. Our polyprotic surfaces extend the V mL axis twice as far – to 400 mL. Because of this, there will be a more noticeable sag in the far end of the pH 7 dilution ramps for the surfaces. This is a manifestation of the growing chemical inertia with respect to changing system concentrations through dilution by the tritrant. Panel I of Figure 4.11 which holds both the pH and log buffer capacity topo surfaces for oxalic acid.

The log buffer capacity topo surface nicely shows both buffer capacity minima. There is little initial point rise on either the pH or buffer capacity topo. The first equivalence point canyon is rather modest because pK_{a1} and pK_{a2} differ by just three orders of magnitude. The smaller the equivalence point break on the pH surface, the shallower the canyon on the buffer capacity topo. The second equivalence point canyon for oxalic acid is much more substantial in that there is an eight orders of magnitude jump in pH. Oxalic acid has a pK_{a1} of 1.252 and a pK_{a2} of 4.266. Panel II of Figure 4.11 shows the pH vs dilution buffer capacity surface. Since pK_{a1} is so small, the first buffer ridge of this plotting style is completely consumed in the “HCl wing”.

Panel I

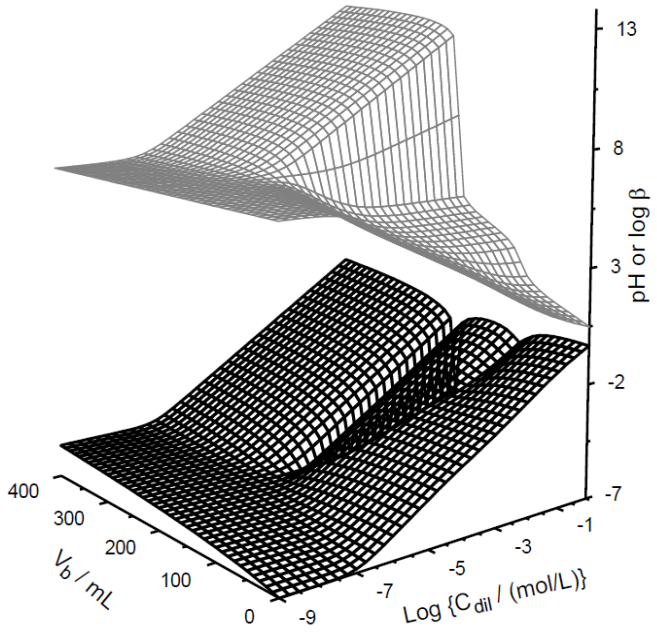

Panel II

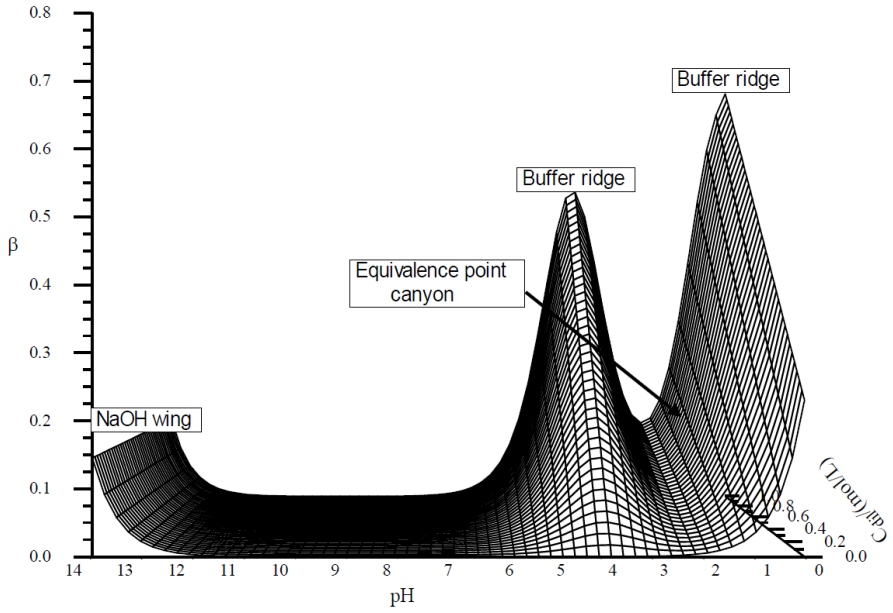

Figure 4.11. Topo surfaces for diprotic oxalic acid. Panel I, Upper – pH surface. Lower – buffer capacity. Panel II - linear buffer capacity surface that relates to the traditional pH vs. buffer capacity plots.

Figure 4.12 shows superimposed buffer capacity slices at 1.00 M for oxalic acid and 8-hydroxquinolie (8HQ). The pK_as for 8HQ are 4.91 and 9.81. Notice that the higher pK_{a1} leads to a more pronounced initial point rise. The smaller difference between its pK_{a1} and pK_{a2} reduces the depth of the second equivalence point canyon. Between the canyons of polyprotic systems are buffer ridges all of similar height. The maximum buffer capacity on most buffer ridges usually exhibits a log β value near -0.23. The maximum values for the 1.00 M slice of oxalic acid (log C_a = 0) is -0.16 halfway to the first equivalence point (50 mL) and -0.23 halfway between the first and second equivalence points (150 mL).

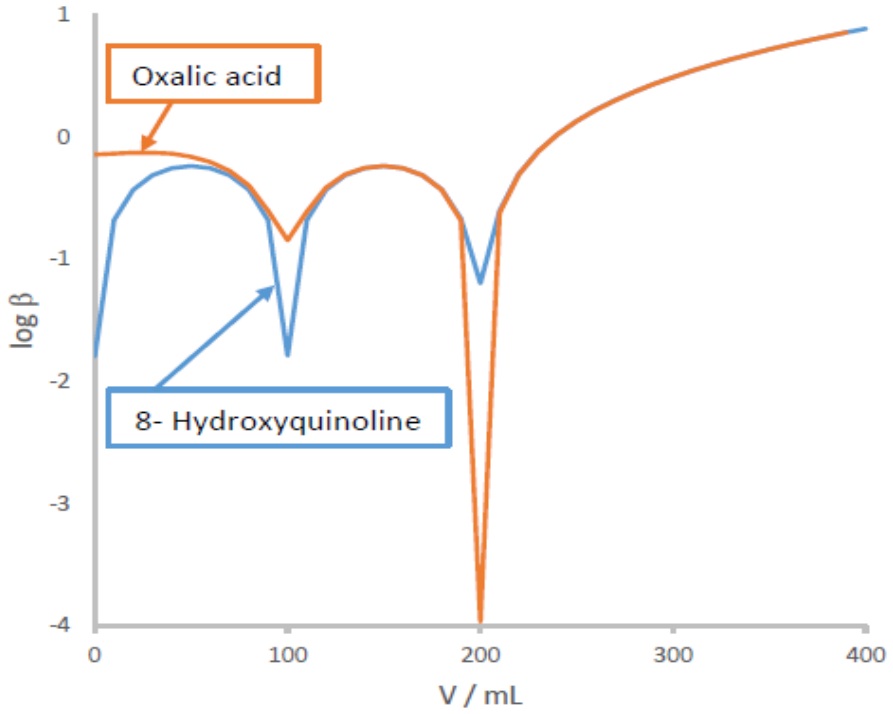

Figure 4.12. Buffer capacity curves for the 1.00 M slice of oxalic acid (solid line) and 8-hydroxquinoline (dotted line)

The first buffer ridge value for oxalic acid is higher than the typical -0.23 value for weak acids because K_{a1} is so large that near pseudo-buffering is seen. (Refer back

to the 1.00 M slice for HCl in Figure 9.) A weaker K_{a1} will lead to a first buffer ridge crest at -0.23. Both buffer ridges for 8HQ show a maximum of -0.23.

Example topos for a triprotic system, L-histidine dihydrochloride (L-his), are presented in Figure 4.13 – the pH topo in Panel Ia, logarithmic buffer capacity topo in panel Ib. The linear pH vs. dilution buffer capacity surface in Panel II. The K_a values used in their calculation were 2.2×10^{-2}, 9.5×10^{-7} and 8.3×10^{-10} with corresponding pK_a values of 1.7, 6.02 and 9.08, respectively. As with oxalic acid, the linear buffer capacity surface for L-his (Panel II) has only a partial first buffer ridge visible because its pK_{a1} is rather low. The logarithmic buffer capacity surface (Panel Ib) again gives a much clearer indication of the first equivalence point with a canyon feature. It is more pronounced than that of oxalic acid because the difference in pK_{a1} and pK_{a2} is 4.32 orders of magnitude, more than one unit larger than was found with oxalic acid. Hence, the first equivalence point canyon is deeper. The second and third equivalence point canyons are comparable in depth because their equivalence point cliffs are similar in magnitude. The extent of the equivalence point canyon in the dilution direction is a combination of the size of the equivalence point break and how close the pH of the equivalence point break is to the pH=7.00 for the diluent water. The second equivalence point canyon of L-his is fairly shallow because the difference between pK_{a2} and pK_{a3} is only 3.06 orders of magnitude. Shallow though it is, it extends almost all the way down the slopping surface to the pH 7 dilution ramp. Consider the three canyons present in Figure 4.12. Even though all are about the same depth, they have very different extents. The further away a pK_a is from 7.00, the more quickly dilution will cause its depth to decline.

Panel Ia

Panel Ib

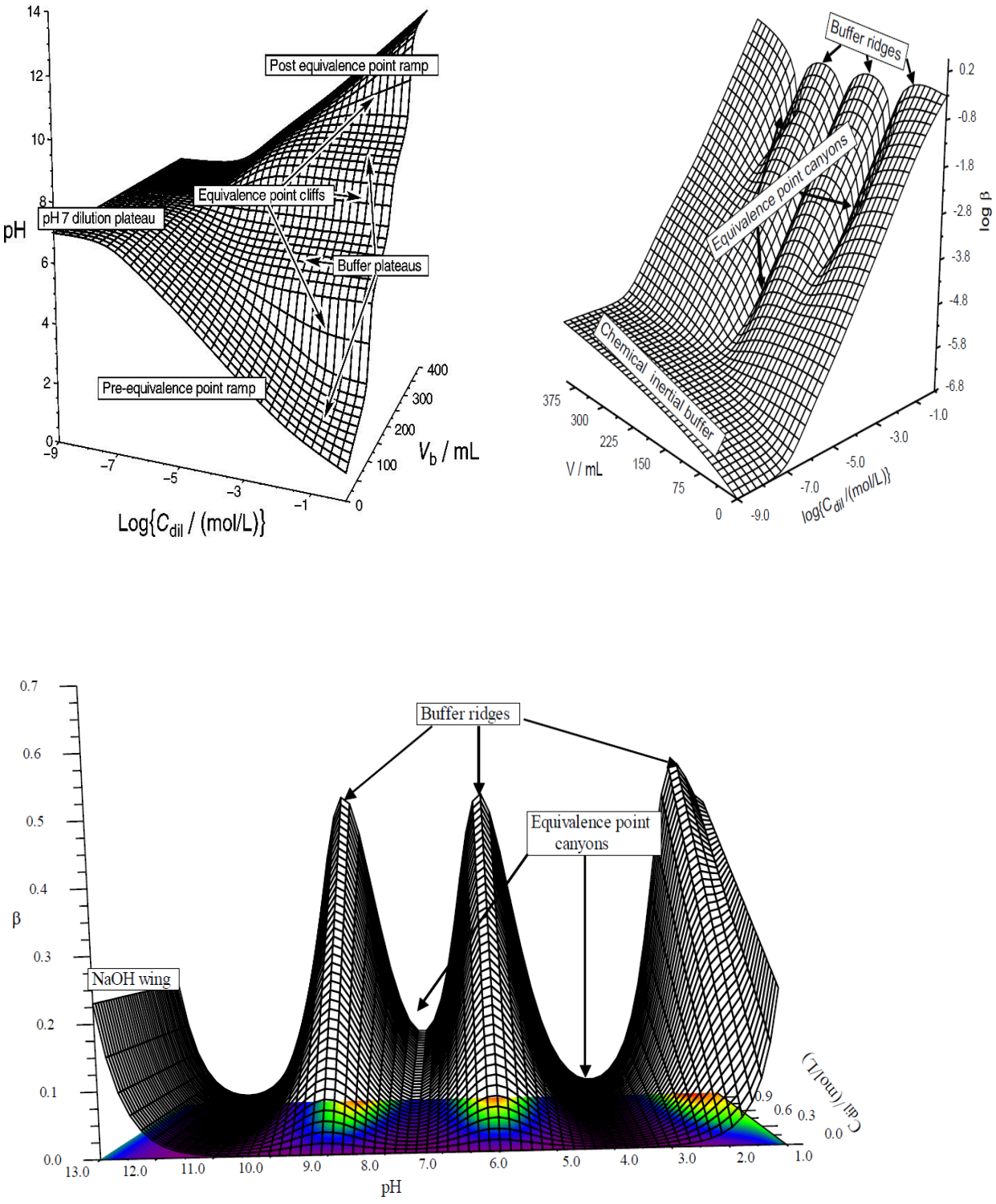

Figure 4.13. Trend surfaces for L- his. Panel Ia – pH surface, Panel Ib – log buffer capacity topo. linear pH vs. dilution buffer capacity surface in Panel II.

It is hydrolysis effects on the buffer agents that drive this process. Notice that the third canyon is the shortest of the three and that the middle canyon is about two times longer than the first. The only new feature seen with the L-histidine dihydrochloride surface is a third equivalence point above pH 7.

Table 4.1. Equivalence Point Canyon Parameters for L-his Buffer Capacity Topo

Equivalence Point	**Magnitude of break: ΔpH $\pm$ 50 mL of equivalence point**	**ΔpH_{ep}: Offset of equivalence point pH from 7.00**	**Extent of canyon (log dilution factor)**
Acetic acid 1st	13.30 – 4.75 = 8.55	9.23 -7.00 =2.23	6.0
Oxalic acid 1st	4.27 – 1.36 = 2.91	7.00 – 2.78 = 4.22	2.75
Oxalic acid 2nd	13.15 – 4.27 = 8.88	8.89 – 7.00 =1.89	6.0
1st equivalence point canyon @100 mL	6.03 - 1.75 = 4.28	7.00 - 3.87 = 3.13	4.5
2nd equivalence point canyon @200 mL	9.08 – 6.03 = 3.05	7.55 – 7.00 = 0.55	5.75
3rd equivalence point canyon @300 mL	13.05 – 9.08 = 3.97	11.23 – 7.00 = 5.23	2.25

The third buffer plateau (pH = pK_{a3} = 9.08) begins to degrade before the 10^{-3} level on the log C_a axis. In this instance, $K_{b1} >> K_{a3}$ so the diluent water is driving the hydrolysis reaction to reprotonate the his^{2-} species. From log C_a values of -3 to -7, mass action effects from diluent water drive the protonation of $Hhis^-$ and converts it to H_2his. At these alkaline starting pHs, very little H_2his is present to dissociate in opposition. From alpha species distribution calculations, the pH 7 dilution plateau shows a mixture that is roughly 90% $Hhis^-$ and 10% H_2his. For brevity, we omit surfaces and buffer capacity calculations for the titration of bases with a strong acid. Their chemical characteristics are analogous.

4.7 Conclusions

An Excel file that implements the calculations for buffer capacity surfaces is found in Appendix IIA. It contains embedded Visual Basic™ macro-enabled formulas for the buffer capacity equations -- a strong acid, and weak monoprotic, diprotic and triprotic acids titrated by NaOH. Each worksheet is populated with the weak acid examples presented in this chapter. To generate buffer capacity surfaces for any other acid, the user needs only to supply new K_as. By examining several example surfaces, anyone should be able to predict systematic trends in buffer capacities without resorting to detailed calculations.

References:

1. Scagnolari, F.; Lunelli, B. pH Basics. *J. Chem. Educ.*, 2009, *86* (2), p 246-250.

2. Clark, R.W., White, G.D., Bonicamp, J.M., Watts, E.D. From Titration Data to Buffer Capacities: A Computer Experiment for the Chemistry Lab or Lecture. *J. Chem. Educ*. **1995,** *72*(*8*), 746-750.
3. Smith, G. C.; Hossain, Md. M.; MacCarthy, P. 3-D Surface Visualization of pH Titration "Topos": Equivalence Point Cliffs, Dilution Ramps, and Buffer Plateaus. *J. Chem. Educ.*, **2014**, *91* (2), pp 225–231.
4. Chiriac, V.; Balea, G.; Buffer Index and Buffer Capacity for a simple Buffer Solution. J. Chem. Educ. 1997, 74, 937-939.
5. Curvale, R. A. BUFFER CAPACITY OF BOVIN SERUM ALBUMIN (BSA). The Journal of Argentine Chemical Society. 2009, 97 N^0 1, 174-180.
6. Alvarez-Nunez, F. A.; Yalkowsky, S. H. Buffer capacity and precipitation control of pH solubilized phenytoin formulations. Int. J. Pharm. Sci. 1999.185, 45-49.
7. Yong, R. N.; Warkentin, B. P.; Phadungchewit, Y.; Galvez, R. BUFFER CAPACITY AND LEAD RETENTION IN SOME CLAY MATERIALS. Water, Air, and Soil Pollution 1990, 53: 53-67.
8. Casiday, E.; Holten D.; Krathen, R.; and Frey R. F. Blood-Chemistry Tutorials: Teaching Biological Applications of General Chemistry Material. *J. Chem. Educ.*, 2001, *78* (9), p 1210-1215.
9. Faust, D. A.; McIntosh, A. BUFFER CAPACITIES OF FRESH WATER LAKES SENSITIVE TO ACID RAIN DEPOSITION J. ENVIRON. SCI. HEALTH, A18(1), **1983**, 155-161.
10. Van Slyke, D. D. *J. Biol. Chem.* **1922**, 52, 525– 570.
11. Bates, R. G. Measurement of Effect of Dilution upon pH Anal. Chem. 1954. 26(5), 871-874.

12. Michlowski, T.; Parczewski, A. A NEW DEFINITION OF BUFFER CAPACITY. CHEMIA ANALITYCZNA. 1978, 23, 959-963.
13. Ramette, R. W. The Acid-Base Package: A Collection of Useful Programs for Proton Transfer Systems *J. Chem. Educ. Software* **1989**, 2B, No. 2
14. Lambert, W. J.BUFCALC: A Program for the Calculation of Buffers of Specified pH, Ionic Strength, and Buffer Capacity. *J. Chem. Educ.* **1990**, 67, 150– 153.
15. Ramette, R. W. Buffers Plus. *J. Chem. Educ.* **1998**, 75 (11) 1504
16. Gutz, I. G. R. http://www2.iq.usp.br/docente/gutz/Curtipot.html(accessed June 6th 2014.
17. Martell, A.E.; Smith, R.M. *Critical Stability Constants*, Plenum Press, New York, 1974.
18. Cracolice, M.S. and Peters, E.I., *General Chemistry: An Inquiry Approach, Second Semester*, Cengage Learning, Mason, OH, 2009.
19. Chang, R.; Goldsby, K.A., *Chemistry,* 11 ed., McGraw-Hill, Columbus, OH, 2013.
20. Brown, T.E.; LeMay, H.E.H.; Bursten, B.E.; Murphy, C.; Woodward, P.; *Chemistry: The Central Science,* 12 ed., Pearson Prentice Hall, Upper Saddle River, NJ, 2013.

Chapter 5
Metal Anti-Buffering: A Situation in Which Aqueous Free Metal Activities Increase upon Dilution

5.1 Introduction

Metal ions in solution can display a form of buffer behavior similar to acid-base systems. Under the right conditions, the activity of a free metal ion can remain steady as the overall system is changed with respect to total metal, total ligand or dilution[1,2]. This is important in the stabilization and detection limits of some ion-selective electrodes as well as in biochemical experiments where constant metal activities are desired[3]. This chapter describes an unusual buffer situation that can occur with metal ions, but does not occur in acid-base systems. Termed "anti-buffering", it is an outcome of using a composition grid approach to look at all possible situations in which a metal ion (M^{n+}) could interact with a ligand (L) in aqueous solution under controlled conditions of temperature, pH and other interfering ligands. Species considered in the modeling below are the free metal ion itself along with its various hydroxo-complexes, free and protonated ligands, and all reported stoichiometries of mononuclear complexes. A composition grid was established to cover essentially all feasible ratios with which the metal and ligand could be combined. Free metal activities were plotted as pM^{n+} values on the z-axis above the grid to generate a 3-D topo trend surface[4]. A counterintuitive result was noted in that in some situations the free metal activity increased orders of magnitude as the overall system underwent dilution.

5.2 Theoretical Explanation

Metal anti-buffering is only observed when diluting systems of aqueous metal complexes where stoichiometries higher than 1:1 are dominant. It also

requires that excess ligand conditions exist and that the overall protonation constants for the ligand are greater than the formation constant for the 1:1 metal complex but less than the overall formation constant for the 1:2 complex. When a system with these properties is now diluted, some of the complex will dissociate but the metal released in this dissociation will be so significant, compared to what was there prior to dilution that the free metal activity will actually rise.

Table 5.1. Three scenarios that can occur when a metal-ligand system is diluted.

System condition:	Free metal sources:	Behavior
Excess ligand with 1:2 complex:	Contribution from dissociation > dilution	Metal Anti-buffering
Excess ligand with 1:1 complex:	Contribution from dissociation = dilution	Metal Buffering
Excess metal or very dilute:	Contribution from dissociation < dilution	Unbuffered

Consider a theoretical examination of a simplistic system where a strong 1:3 complex having an overall stability constant β_3 overwhelms any other effects. Under excess ligand conditions the major species in solution will be ML_3 and L. Only a trace of the free metal ion, M^{n+}, is present. (The development below will use M in place of M^{n+} for ease in viewing.) If a 10-fold dilution is made, the concentrations of both ML_3 and L will essentially drop by an order of magnitude.

$$M + 3\,L \Leftrightarrow ML_3 \qquad \text{(Eq 5.1)}$$

Before dilution: $$\beta_3 = \frac{[ML_3]}{[M]_{old}[L]^3} \qquad \text{(Eq 5.2)}$$

After dilution: $$\beta_3 = \frac{0.1[ML_3]}{[M]_{new}(0.1)^3[L]^3} \qquad \text{(Eq 5.3)}$$

Ratioing the before and after expressions and solving for $[M]_{new}/[M]_{old}$ yields:

$$\frac{[M]_{new}}{[M]_{old}} = 100 \qquad \text{(Eq 5.4)}$$

This clearly suggests that the small amount of complex that dissociates releases a significant amount of free metal compared to what was there before, a 100-fold increase. While the change in free trace metal activity is substantial, the ratio of ML_3 and L activities is essentially the same as before. Overall, the system was diluted by a factor of 10, and the free metal concentration went up by a factor of 100. This is an **"anti-buffering effect**" of 1000 = 100-fold increase x 10-fold expected dilution. A parallel mathematical treatment of a system with only a 1:1 complex present would show $[M]_{new}/[M]_{old} = 1$, namely, the traditional example of metal buffering systems[1].

5.3 Computational approach: 3-dimensional free metal topo surfaces

To demonstrate where metal anti-buffering will be found and to compare it to that of traditional metal buffer, a composition grid and associated pM^{n+} topo surfaces will be employed. The composition grids[4] used here plot the total concentration of metal (M_{tot}) on the x-axis and the total concentration of ligand (L_{tot}) on the y-axis (Fig 5.1). Any point on the two dimensional composition grid represents a particular composition from the mixing of metal ion and ligand. One is illustrated in Fig 5.1 for a system with $L_{tot} = 10^{-2}$ M and $M_{tot} = 10^{-7}$ M. Both the metal and ligand total concentrations span from 1M to $1x10^{-9}$ M. The axes are logarithmic with spacing intervals of 0.25 log units. This creates total of a 37 × 37= 1369 grid points. Addition of a third z-axis allows pM^{n+} or other system parameters (e.g., free ligand, individual complex stoichiometries, absorbance, etc.) to be examined as trend surfaces. These topo surfaces on the composition grid provide a comprehensive framework for

interpretation of the results from the equilibrium experiments. Free metal topo surfaces for six modeled systems will demonstrate the extent and magnitude of the metal anti-buffering.

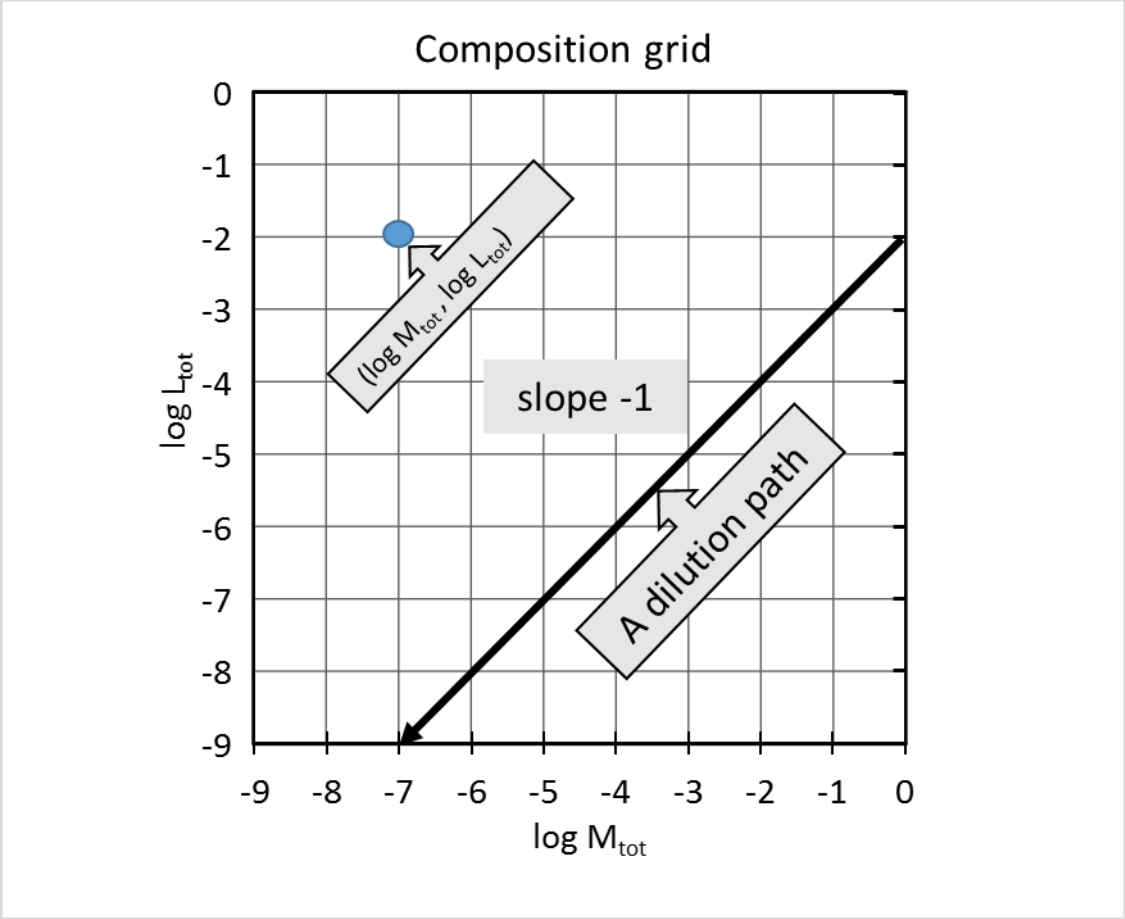

Figure 5.1: The metal-ligand composition grid.

Metal anti-buffering requires an examination of systems as they undergo dilution. Thus, it is necessary to identify what constitutes a dilution path on the two dimensional composition grid. A dilution path is defined by the sequence of compositions that are encountered during the procedure. Dilution procedures diminish the total concentration of both components at the same rate and are represented by paths that move down and to the left with a slope of +1 (refer again to Fig 5.1). Once a specific dilution path has been selected, the changes in any given species during the dilution procedure

can be depicted as the upward projection of the path onto the specie's 3-D topo surface above the grid. Complexation TOPOS software with macro-enabled Excel spreadsheets (see Appendix II.B) has been developed parallel to the pH and BufCap TOPOS from the acid-base studies.

5.4 A Sample system – Cu(II)-ethylenediamine

The copper(II) – ethylenediamine system we be used to illustrate how the modeling is done. A complete accounting requires inclusion of free metal, all stoichiometries of complexes and hydrolytic species of both metal and ligand. In addition, the activity effects are taken into account for all charged species. The ultimate goal of the modeling is to calculate the activity of metal and free ligand. We fix pH and ionic strength for all grid points. Thermodynamic formation constants for all possible interactions were obtained from the literature. Overall formation constants (βs) were used to reduce a large system of nonlinear equations into a pair of master variable expressions, *i.e.,* free metal (Cu^{2+}) and free ligand (ethylenediamine, or en for short). The concentration of all other species present in the equilibrium mixture can be expressed as a function of Cu^{2+} and en.

Table 5.2 Overall formation constants (βs) for the Cu/en system

Species	β	Reference
$Cu(OH)^{+}$	$10^{7.34}$	5
Hen^{+}	$10^{10.18}$	6
H_2en^{2+}	$10^{17.65}$	6
$Cu(en)^{2+}$	$10^{10.47}$	7
$Cu(en)_2^{2+}$	$10^{19.67}$	7

$Cu(en)_3^{2+}$	$10^{20.36}$	6

All constants were corrected to concentration constants using the Davies equation to compute activity coefficients for all charged species at 0.1 M KNO_3[8].

The mass balance for Copper is:

$$Cu_{tot} = [Cu^{2+}] + [CuOH^+] + [Cu(en)^{2+}] + \left[Cu(en)_2{}^{2+}\right] + \left[Cu(en)_3{}^{2+}\right]$$

$$Cu_{tot} = [Cu^{2+}] + K^o_{OH}[Cu^{2+}][OH^-] + \beta_1{}^0[Cu^{2+}][en] + 2\beta_2{}^0[Cu^{2+}][en]^2 + 3\beta_3{}^0[Cu^{2+}][en]^3$$

The corresponding mass balance for en is:

$$en_{tot} = [en] + K^o_{enH}[H^+][en] + K^o_{en2H}[H^+][en]^2 + \beta_1{}^0[en][Cu^{2+}] + 2\beta_2{}^0[en]^2[Cu^{2+}] + 3\beta_3{}^0[en][Cu^{2+}]^3$$

The pair of mass balance equations was solved for each grid point using a numerical method as described in Smith (1983)[9]. It is a modified continued fraction algorithm that was first applied to aqueous modeling by Perrin[10]. A detailed description and program listing is found in Appendix.

The Cu(II)-en system's free metal topo surface, as pCu^{2+}, is shown in two forms (Figure 5.2) for most clearly demonstrating metal anti-buffering. Anti-buffering occurs on the down-sloping "upper buffering ramp". A "stoichiometric cliff" runs diagonally across surface. This marks the boundary between excess ligand conditions and excess metal conditions. The anti-buffering is only seen under excess ligand compositions. Below and rising to the left of the stoichiometric cliff is the "lower normal dilution ramp". The stoichiometric cliff fades out when dissociation of complexed metal can no longer make up for dilution effects. Two dilution paths have been projected onto the pCu^{2+} topo, one for excess en conditions (red + blue trace) and one for excess copper conditions

Panel I

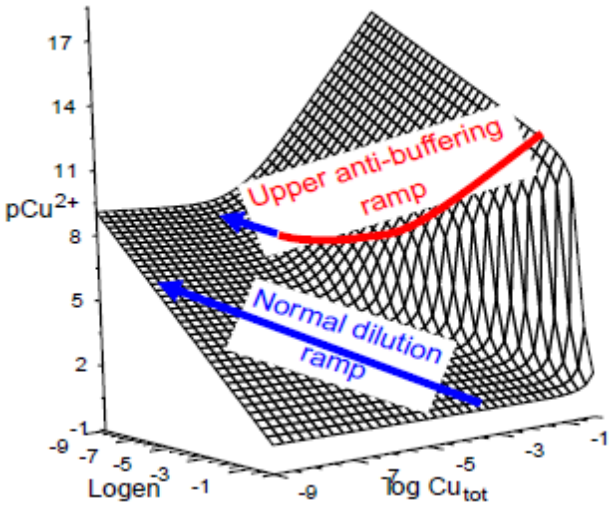

Panel II

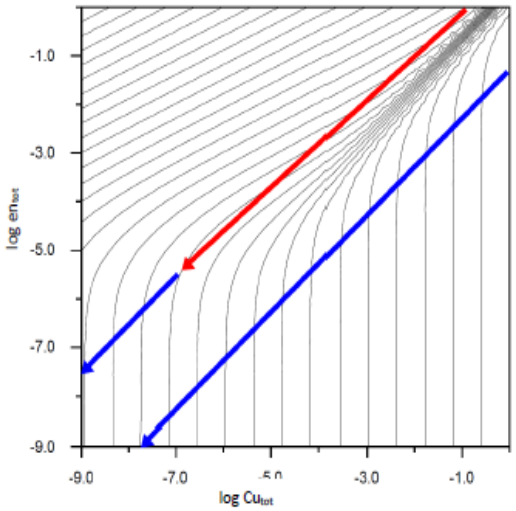

Panel III

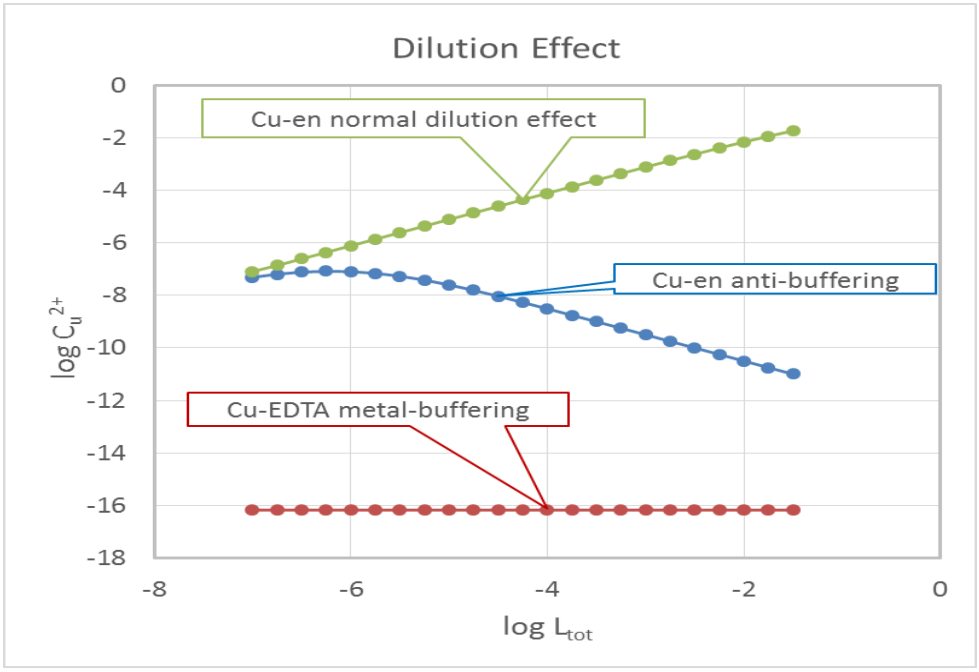

Figure 5.2. Anti-buffering vs. buffering vs. unbuffered systems. Panel I - pCu^{2+} topo surface in the bent-wire form with anti-buffering shown as a red dilution path and unbuffered behavior shown as a blue dilution path. Panel II, contour map version of Panel I. Panel III compares the the anti-buffering behaviour of Cu-en to the traditional buffering in the Cu-EDTA system.

Anti-buffering occurs where the path has been colored red and is **descending** diagonally across the upper buffering ramp. Eventually, dilution overtakes the anti-buffering effect whereupon the free Cu^{2+} activity begins to drop with dilution. This portion of the projected path is blue. The experimental path projection that is entirely blue, demonstrates that anti-buffering never occurs in the excess metal portion of the topo. The path monotonically rises diagonally across the lower normal dilution ramp.

If one selects a specific set of starting conditions and traces a dilution path through the composition grid data, the predicted anti-buffering effect can be calculated. For example, if one starts with the total en concentration at log -1.5 (0.031 M) and total copper concentration at log -2.5 (0.0031 M), there is a ten-fold excess of ligand and anti-buffering will occur. As one progresses through the series of grid points corresponding to system dilution, the pCu^{2+} value drops from 9.041997 to 6.093596, a difference of 2.948401 log units or a linear increase of 887.9755 times. At the same time, the system has been diluted from a starting ligand concentration of log -1.5 to log -5.25. This is a 3.75 log unit drop or a dilution of 5623.413 times. Total metal concentration has undergone the same 5623-fold dilution. Multiplying the two factors together yields an anti-buffering effect of 4, 993,453. Thus, while both the total en and copper concentrations dropped by more than 5000 times, the free metal activity went up about a 1000 times. This magnitude of anti-buffering is more than can be feasibly measured given limits of detection constraints of ion selective electrodes (ISE), the most direct means by which to measure Cu^{2+} activity.

Anti-buffering is easily seen on the contour map version of the topo. Here, anti-buffering shows up as an experimental path that crosses contour lines in the upper buffering ramp region. This is equivalent to saying that anti-buffering is found anywhere that the upper buffer ramp contour lines have a slope less than +1 and are not parallel to the stoichiometric cliff. Because of the nature of p-functions, the activity of free metal ion is rising wherever there is downward movement on the pCu^{2+} surface. Anti-buffering breaks down when the pCu^{2+} contour lines of the upper buffering ramp begin to curve towards the log Cu_{tot} axis. Notice that the completely blue trace under excess metal conditions shows a steady rate of crossing contours in an upward surface direction; there is a constant 45°-angle between the contour lines and the dilution path whenever normal dilution behavior is observed.

5.5 A Free metal topo surface for traditional metal buffering

Consider the pCu^{2+} topo surfaces for the Cu-EDTA system (Fig 5.3). Because only 1:1 complexes form in this system, there is no anti-buffering that occurs.

Panel I

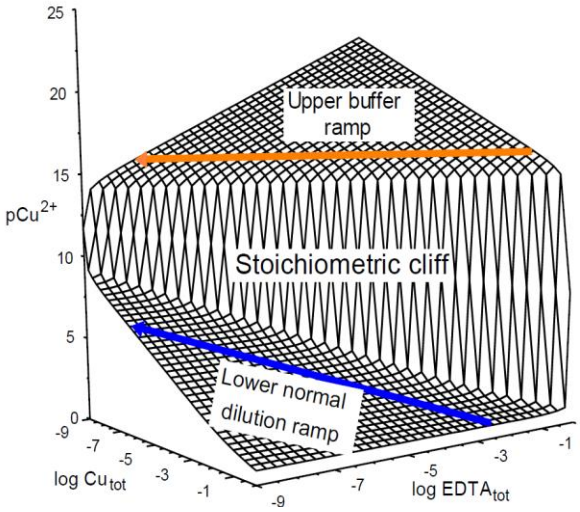

Panel II

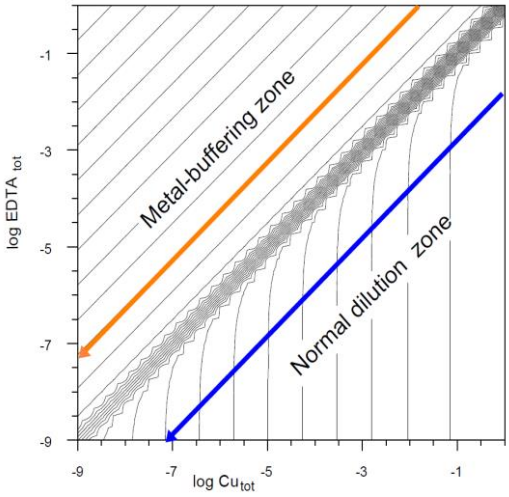

Figure 5.3. Metal buffering in the Cu-EDTA system. Panel I - bent-wire and Panel II- contour map versions of the Cu-EDTA pCu^{2+} topo surfaces at pH 5.5.

This provides an opportunity to visualize the difference between metal anti-buffering and traditional metal buffering. The same type of features are prominent for this topo surface, too: 1) an upper buffer ramp in the region of excess ligand; 2) a stoichiometric cliff; and 3) a lower normal dilution ramp
As was done for the Cu-en system, two dilution paths have been projected onto the pCu^{2+} topo surface. The orange trace illustrates traditional metal buffer behavior. The pCu^{2+} value does not change with overall system dilution. **Metal buffering** is characterized by a dilution path traversing the upper buffer ramp in a **horizontal** orientation. This is most easily seen on the contour map plot in that the orange dilution path is parallel to the contour lines of the upper buffer ramp. The dilution path is also parallel to the stoichiometric cliff that runs across the topo at a 45^o angle. Sample dilution in the region of excess metal is identical to the trace seen in the Cu-en system. Neither metal anti-buffering or metal buffering will be exhibited here. The blue dilution path steadily crosses contours in an upward surface direction; intersecting them at a 45^o-angle in all cases.

5.6 Other model systems that show the metal anti-buffering effect

The discovery of the anti-buffering phenomenon prompted an exploration for systems beyond Cu-en that display the same behavior. Complete thermodynamic data must be available before modeling can be performed. The compendiums of critically reviewed constants by Smith and Martell[11] offered a wide range of systems to evaluate. Because there was a desire to possibly conduct experimental confirmation of model results, ligands that form complexes with Cu^{2+} were examined first. It was not difficult to locate many.

Table 5.3 summarizes systems of ligands with Cu^{2+} that were modeled, the location of the selected dilution pate and the resultant anti-buffering effect.

Table 5.3. Metal Anti-Buffering Exhibited by Other Ligands with Cu^{2+}

Ligand	Log L_{tot}	Path (start-finish)	Anti-Buffering Effect
Pyrrolidine	-3.00	-5.00	2511
NTA monoamide	-2.50	-8.25	2.04×10^{18}
Ammonia (pH 9.0)	-4.00	-5.50	301,277
Methionine	-3.00	-7.25	7.07×10^{7}
2HMI	-2.50	-5.00	2.19×10^{6}

The pCu^{2+} topo surfaces for four of these systems are collected as Figure 5.4. Several nuances in anti-buffering behavior can be seen with these topos. The systems for Panels I, III and IV contain ligands that form stable higher stoichiometric complexes but have 1:1 formation constants lower than the ligand protonation constants. This is not true for the NTA monoamide topo in Panel II. For NTA monoamide the 1:1 copper(II) complex log formation constant is slightly higher than the ligand log protonation constant, 9.68 vs. 8.9. A consequence of this is that both anti-buffering and traditional metal buffering are seen on the upper buffer ramp. Under more concentrated conditions, anti-buffering occurs.

But as the system is diluted, the higher complex dissociates more and more. In the other three systems the protonation reaction is favored over the 1:1 complex and regular metal buffering never happens. But with NTA monoamide, the 1:1 complex slightly overpowers the protonation reaction so for a while the metal ion activity remains constant. The shift from anti-buffering behavior to simple buffering behavior is seen as a slight change in the steepness of the upper buffer ramp's slope.

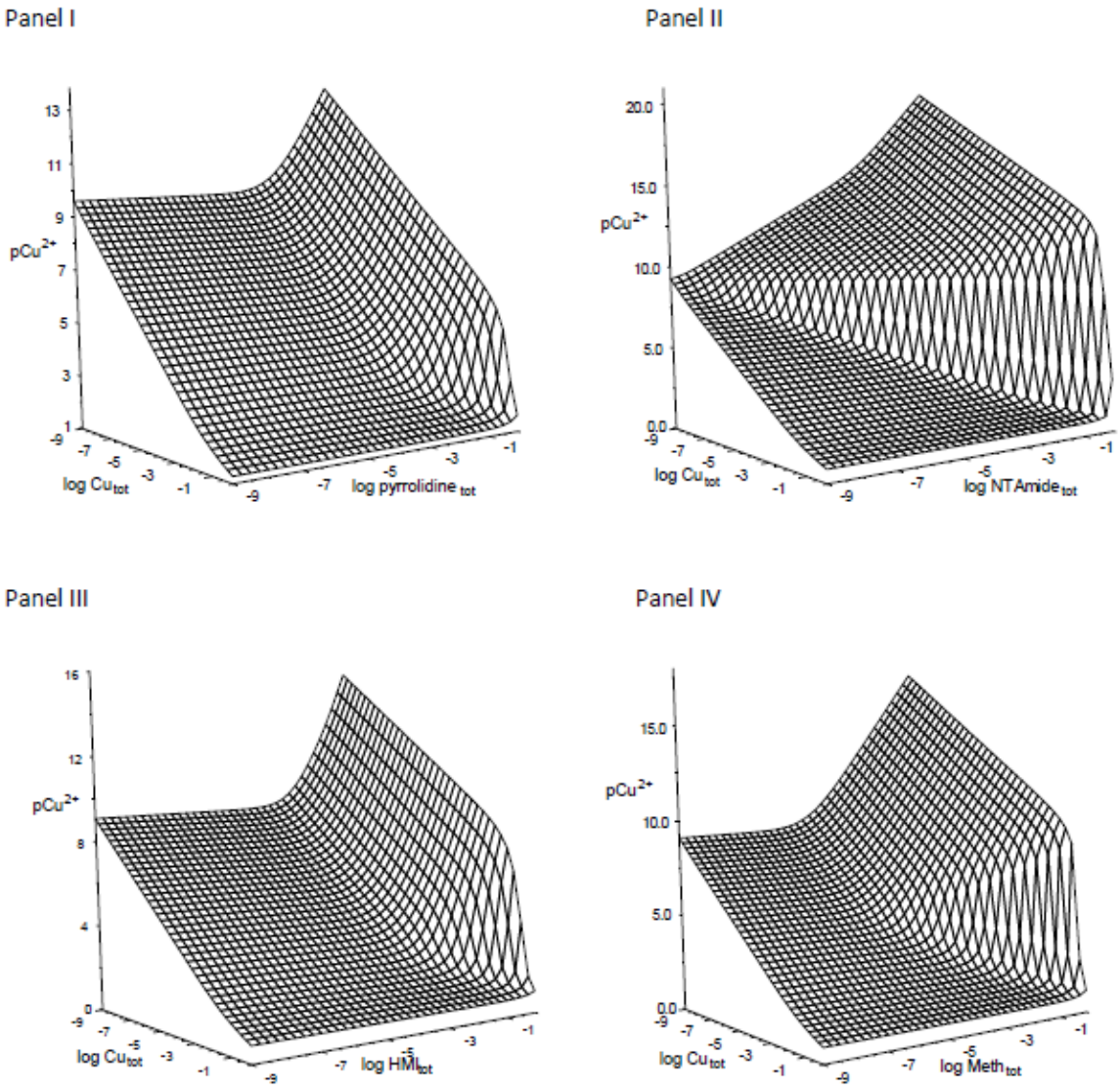

Figure 5.4. pCu^{2+} topo surfaces for four other systems. Panel I – pyrollidine; Panel II – NTAm; Panel III – 5-hydroxyimidazole; Panel IV – DL-methionine.

5.7 Experimental apparatus and protocols

Once the model systems had indicated the metal anti-buffering phenomenon, experimental confirmation of its existence was desired. A basic potentiometric apparatus was built to follow the activity of free metal ions as a metal ligand complexation system was diluted. The design followed was adapted from one originally described by Sposito *et. al.*[12] and modified for composition grid applications by Smith[9]. A Cu^{2+}-en aqueous equilibrium system was selected for

the initial anti-buffering demonstration because the expected Cu^{2+} activities were sufficiently inside the working range of commercially available cupric ion-selective electrodes.

A 400-mL PFTE beaker was used as the reaction vessel to minimize adsorption of trace metal ions. The reaction vessel was placed in a circulating water bath to maintain a constant temperature of 25.0 $\pm$ 0.5°C to avoid significant fluctuations in thermodynamic constants. A transparent acrylic disc was fabricated to cover the reaction vessel and prevent the influx of CO_2 into the solutions. Several holes were drilled in it to accommodate electrode bodies, two temperature probes, solution delivery tubes, and a tube that released N_2 bubbles to help stir the solution and prevent the influx of CO_2 by creating a positive pressure in the headspace above the bulk solution. A magnetic stir bar was placed at the bottom of the reaction vessel to assure complete mixing of all fluid contents.

All solutions, except 0.1M KNO_3 diluent and ion adjustor medium for all other solutions, were delivered to the reaction vessel from calibrated microburets (10.0 mL total volume, Model 03-701-26A, Fisher Scientific, Pittsburgh, PA) through plastic tubing to keep them out of contact with atmospheric CO_2. Delivery of 0.1M KNO_3 solution for dilution purpose was through a calibrated 25-mL Pyrex@ burette (Model 2122A 625 East Bunker Court Vernon Hills, IL 60061 USA.). Tubing was connected to the tip of each burettes by cementing it into a modified Leur hub which was then press-fit onto the burette tip. The tops of all burettes were fitted with Ascarite II® (CAS 1310-73-2 or CAS 1318-00-9, Thomas Scientific, Swedesboro, NJ) guard tubes to prevent uptake of CO_2 from ambient lab air. Any absorbed CO_2 would introduce carbonic acid and bicarbonate into the reagent solution. These

could both alter a solution's pH as well as potentially complex with copper ion. Experimental probes included a combination copper ion-selective electrode (EW-27504-10 Cupric Combination ISE, Cole-Parmer, and Vernon Hills, IL) and a pH combination electrode (WD-35801-00, Oakton Instruments, and Vernon Hills, IL). Measurements were taken by two pH/mV meters with attached temperature probe corrections (Model pH 6, Oakton Instruments, Vernon Hills, IL).

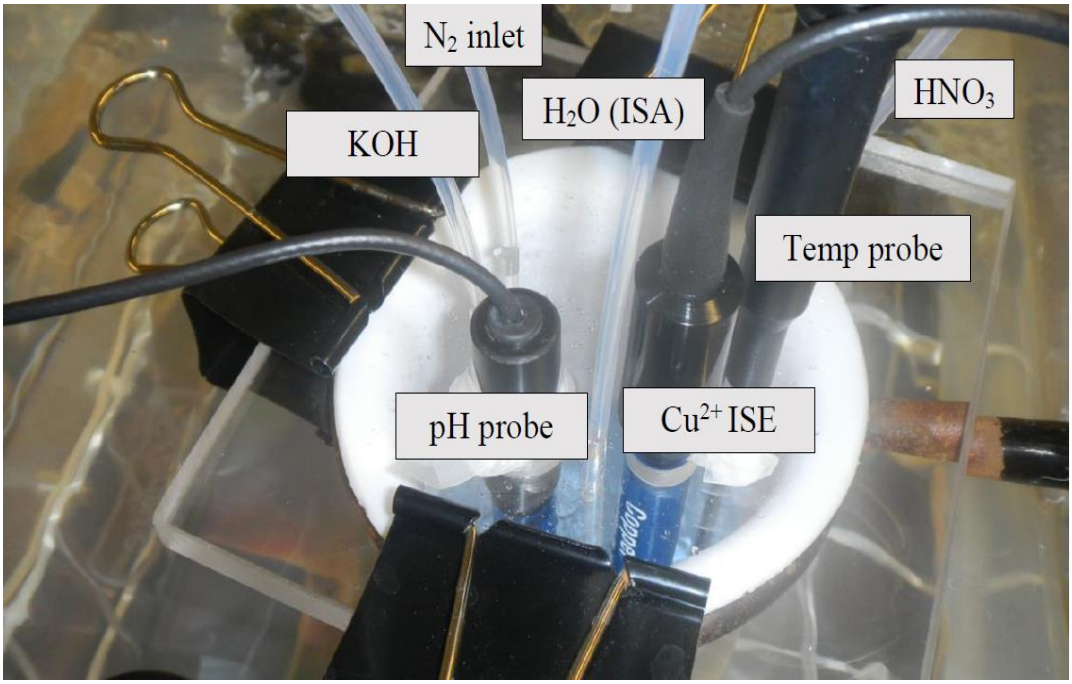

Figure 5.5 A Photograph of the reaction vessel.

Solutions were prepared from freshly degassed deionized water and stored in nitrogen-flushed bottles. The 1.0 M KNO_3 ionic strength adjusting (ISA) solution was diluted to a final working concentration of 0.1 M. The reaction vessel pH was maintained by small additions of 0.1 M HNO_3 (CAS 7697-37-2, Trace metal grade, Fisher Scientific, Pittsburgh, PA) and 0.1 M KOH (CAS 1310-58-3, ACS reagent grade, J.T. Baker, Phillipsburg, NJ). The pH adjusting

solutions needed to be diluted as the experimental path went to lower total concentrations for Cu and en. These more dilute solutions of HNO_3 and KOH were at concentrations of 0.01M, 0.001M.

The ionic strength of all solutions was kept constant by using 0.1 M KNO_3 as a background electrolyte to avoid fluctuations in activity coefficients of free Cu^{2+} ion during dilution experiments and other charged species. KNO_3 is an ideal ISA because K^+ and NO_3^- are essentially not involved in additional hydrolytic or complexation processes. ACS reagent grade KNO_3 has trace levels of iron (maximum of 3 ppm), heavy metals as Pb (maximum 5 ppm) and Cl^- (maximum 0.0002%). When employed as a 0.1 M ionic strength adjustor (ISA), these correspond to 30 ppb Fe, 50 ppb Pb and 200 ppb Cl.

5.8 Sample preparation

Stock solutions of Cu^{2+} (0.1 M Cupric Standard, CAS 3251-23-8 in CAS 7732-18-5, Thermo Fisher Scientific, and Beverly, MA) and en (0.1 M ethylenediamine, CAS 107-15-3, Fisher Chemical, Fair Lawn, NJ) were added to the Teflon reaction vessel such that the pre-dilution volume was about 50-mL containing 0.031 M en and 0.0031 M Cu^{2+}. These were selected to roughly correspond to composition grid points of -1.5 and -2.5, respectively such that there was a 10-fold excess of ligand. This quantity of mixture filled the reaction vessel to a depth of at least 1 cm so that the sensing membranes and liquid junctions of both electrodes were completely immersed. The reference half of the pH combination electrode in particular requires this depth for a proper liquid junction connection. A slow input of N_2 bubbles was used to help stir the solution and keep CO_2 from diffusing into the reaction cell. The 50.00-mL

mixture aliquot was diluted through diluent additions by a factor of about 7, the point at which the reaction vessel capacity had been reached. A 50.00 mL portion of the final solution was used to start a second 7-fold dilution sequence. This procedure was continued an additional two to three times to create an overall dilution maximum of about 7^5 = 16,800-fold. After each addition of diluent, the pH was adjusted to a pre-selected value (4.5, 5.0, 5.5, or 6.0).

Free copper ion activity, A_{Cu}^{2+}, was monitored via the cupric ion-selective electrode. No mV readings from the cupric ISE were recorded until the meter readings were stable for at least one minute. The dilution experiment for each pH was run at least two times to ascertain its reproducibility. Temperature data were also logged to assure that constant temperature conditions had been maintained.

5.9 Cu ISE electrode calibration

The Cu ISE was calibrated by sequential additions of an analytical standard solution of 0.1M Cu $(NO_3)_2$ (0.1 M Cupric Standard, CAS 3251-23-8 in CAS 7732-18-5, Thermo Fisher Scientific, Beverly, MA) into 0.1M KNO_3 solution to match the matrix between the calibration medium and the experimental solution. Separate calibration runs for each pH value that was investigated. Electrode potential (E) vs. pCu^{2+} (-log Cu^{2+}) calibration plots were constructed and subjected to a linear regression procedure to determine the slope, intercept and uncertainties of the electrode response.

Dilution experiments were conducted at pH of 4.5, 5.0, 5.5 and 6.0. At pH lower than 4.5, protons begin to dominate control of ligand binding sites

and anti-buffering becomes less significant. Above a pH of 6.0, solid $Cu(OH)_2$ begins to precipitate from the solution[13-14](Burgess, 1978 Metal Cations in Solution) and compete with aqueous complexes.

Table 5.4. Cupric Ion-Selective Electrode Calibration Parameters

pH	r^2	slope	intercept (mV)	std. dev. in y (mV)
4.5	1.000	28.81 ± 0.23	317.1 ± 0.70	± 0.54
5.0	0.998	28.98 ± 0.41	317.2 ± 1.3	± 1.0
5.5	0.999	28.50 ± 0.40	320.9 ± 1.5	± 1.7
6.0	0.999	28.52 ± 0.40	319.6 ± 1.6	± 1.4

5.10 Results and discussion

The data used to construct metal anti-buffering plots were A_{Cu2+} vs. log en tot. Each A_{Cu2+} value was obtained by using the linear regression parameters from the ISE calibration curve for the pH of interest (Table 5.3). The corresponding log en_{tot} value was calculated by summing the additions from all three burets (diluent water with ISA, acid and base) to produce a total dilution factor that was then applied to the starting total ligand concentration.

The most dramatic metal anti-buffering effect was observed at a pH of 6.0 (Figure 5.6). The x-axis records the progress of dilution in the Log en_{tot} values. A 10-fold dilution of the system corresponds to a 1-log unit step on the x-axis to the left. Since the first experiment data point was log en = -1.50 and the final data point was -5.71, the overall dilution achieved during the experiment was $10^{(5.71-1.50)}$ = 16,200 fold. But the copper(II) anti-buffering does not persist over the entire dilution process. It stops when the activity of Cu^{2+} reaches its maximum level at a log en_{tot} value of -4.62. Thus, the dilution factor

used to compute the anti-buffer effect is $10^{(4.62-1.50)}$ = 1318-fold. Over this same dilution range, the log activity of Cu^{2+} went from -8.75 to -6.74 for an increase of $10^{(8.75-6.74)}$ = 102 times higher. Putting the two factors together yields a combined anti-buffering effect (abf) of 1318 x 102 = 134,896 ≈135,000 times. This indicates that in diluting the system by more than three orders of magnitude, the activity of copper(II) ion has increased two order of magnitude. The anti-buffering phenomenon at pH 6.0 is not a small effect when it is present. The match between the model and experimental data is not perfect, but the general shape and magnitude of the anti-buffering effect is quite similar on both curves. Small offsets between the two curves are no surprise as there is quite a range of reported formation and protonation constants in the literature from which to choose. Sometimes the differences are nearly a factor of two. Another source that can cause discrepancies in the fits lies in the activity coefficients for charged species and activity corrections in the model. At this juncture, the model still needs refinement in that regard. The next generation of programming should help tighten the agreement. Lastly, some earlier experiments with a cupric ion-selective electrode have shown that the sensing membrane can experience interfering side-reactions that affect its readings[9].

Anti-buffering is a consequence of the Law of Mass Action as well as an illustration of Le Chatelier's Principle. Under excess ligand conditions and stable 1:2 $Cu(en)_2^{2+}$ complexes, very little free Cu^{2+} can be found in solution. As the system is diluted, the equilibrium is perturbed and some of the complex dissociates.

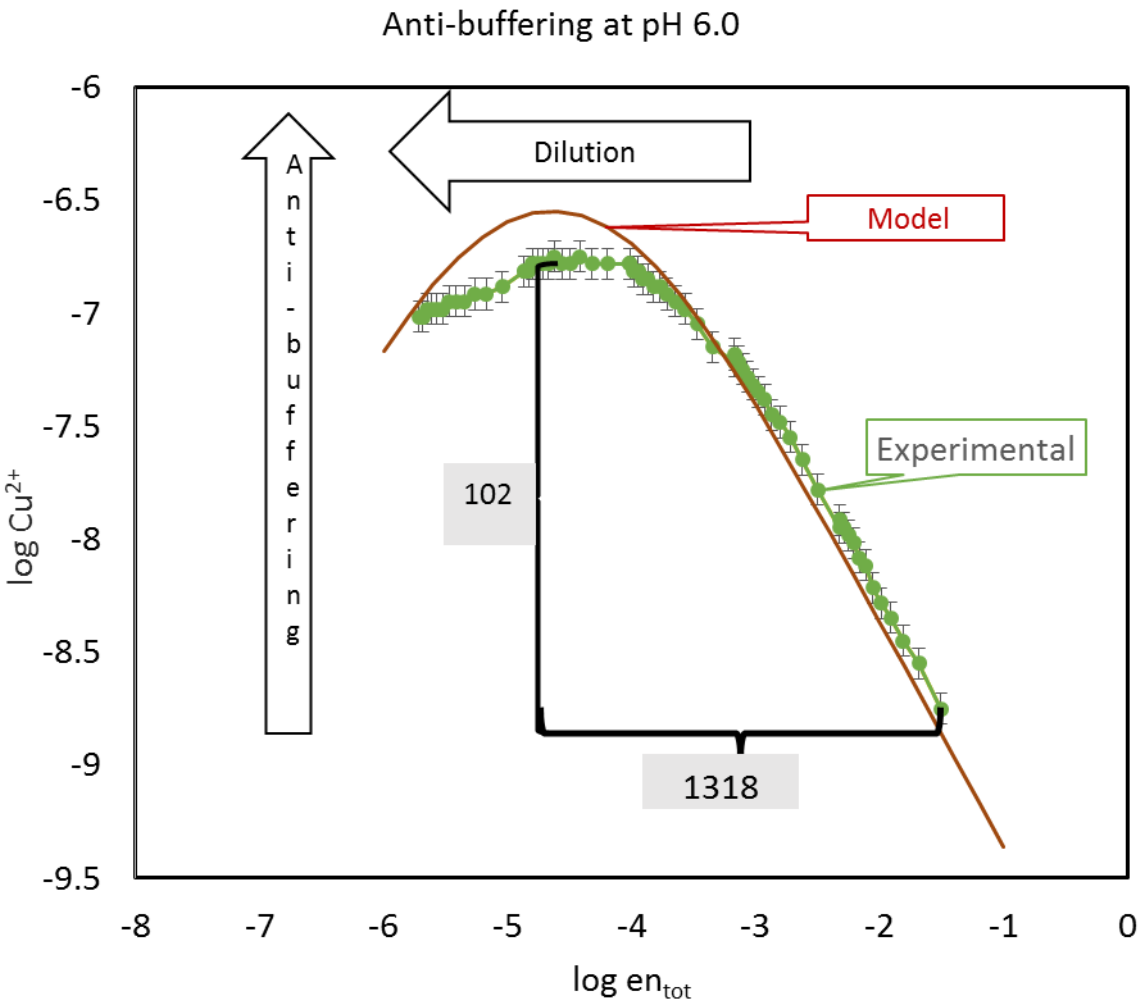

Figure 5.6. Anti-buffering in Cu-en system at pH 6.0. There is 1318x factor from dilution and 102x factor from anti-buffering for an overall anti-buffer effect of ~135,000.

The amount of Cu^{2+} released by the dissociation is so much greater than the free Cu^{2+} in the original solution, that the overall A_{Cu}^{2+} goes up. This continues until sufficient free copper has been released through dissociation that new releases are no longer so much greater in size, *i.e.*, complexed Cu ≈ free Cu^{2+}. Figure 5.7 presents a schematic diagram to help visualize this point. The lower the pH of the system, the less dramatic the metal anti-buffering becomes. This is evident in looking at the experimental vs. modeled behavior of the Cu-en system at pHs of 5.5, 5.0 and 4.5, respectively (Figure 5.8). These runs all used the same starting value of log en_{tot} = -1.5 for comparative purposes. The

observed anti-buffering factors for the three systems were 1290-fold, 16.4-fold and 2.74-fold, respectively. Cu^{2+} ion and H^+ are both Lewis acids and compete for base, *i.e.,* ethylenediamine here in the solution. More ethylenediamine is now bonded with hydronium ion to produce Hen^+ and H_2en^{2+}. At lower pH's, the number of protons that compete with Cu^{2+} for binding to en increases dramatically, a factor of 10 for each pH unit.

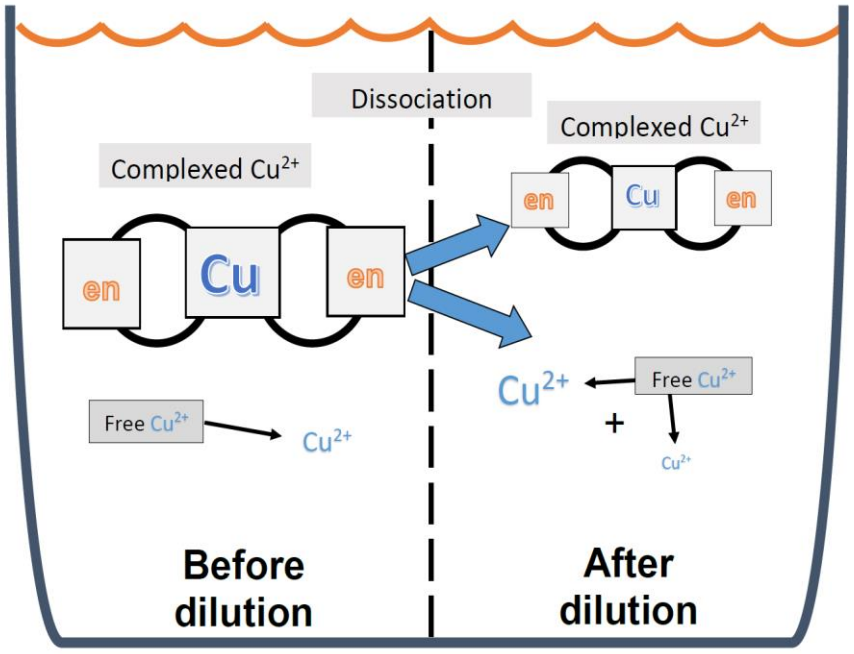

Figure 5.7. Schematic diagram of metal anit-buffering. Font size indicates relative magnitude. The Cu^{2+} released via dissociation is greater than the Cu^{2+} that was previously free.

There is a 31-fold increase of protons at a pH 4.5 compared to pH 6.0. Furthermore, pH 6.0 is no too distant from pK_{a1} of 6.848 for the en system. This is another indication that the fraction of available binding sites will be dropping as the pH wanders to lower values. While the effect seems small, it is actually much larger when the dilution is started at a higher concentration. For a system like Cu-en where a 1:2 complex dominates under excess ligand

conditions, Equation 5.4 indicates that the anti-buffering factor will increase by 100 times with each order of magnitude of dilution. Had the cupric ion-selective electrode been capable of sensing lower than 10^{-9} M of Cu^{2+} activity, greater anti-buffering factors would have been recorded. We could have measured factors of 13,500,000-fold at pH 6.0, 129,000-fold at pH 5.5, 1640-fold at pH 5.0, and 274-fold at pH 4.5.

Panel I

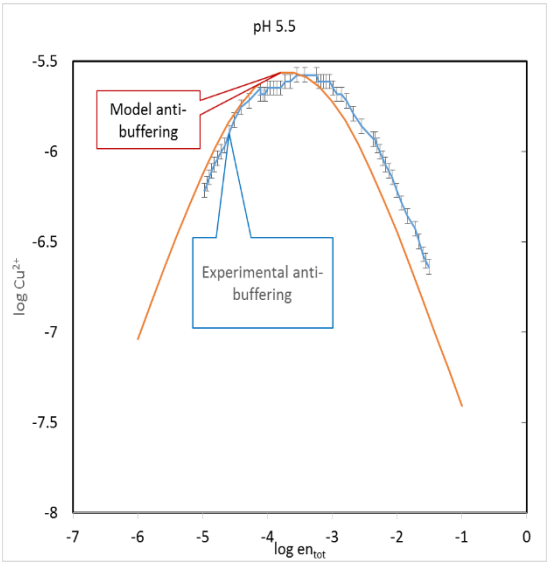

Panel II

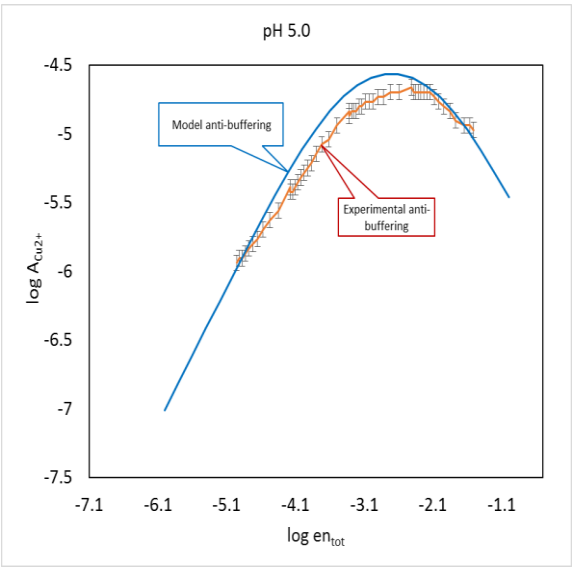

Panel III

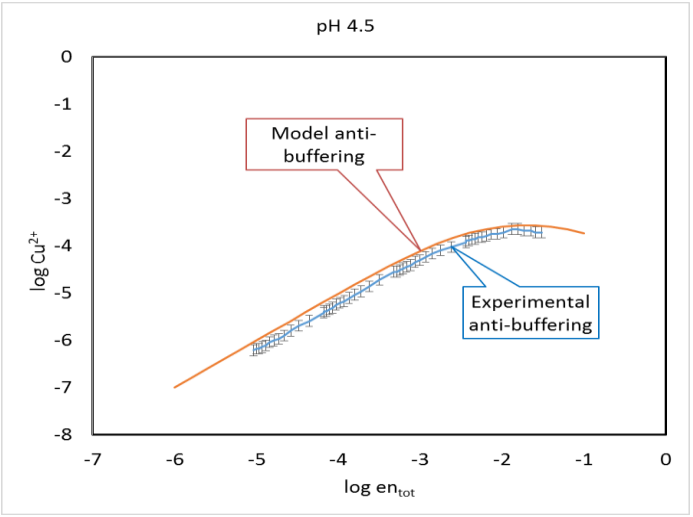

Figure 5.8. Experimental vs. model behavior for the Cu-en system at pH 5.5 (panel I), pH 5.0 (panel II) and pH 4.5 (panel III).

An operational limit on the starting value of en_{tot} was the requirement to maintain the ionic strength of the system. This becomes increasingly difficult above 0.1 M. The behavior of activity coefficients begins to be problematic, too.

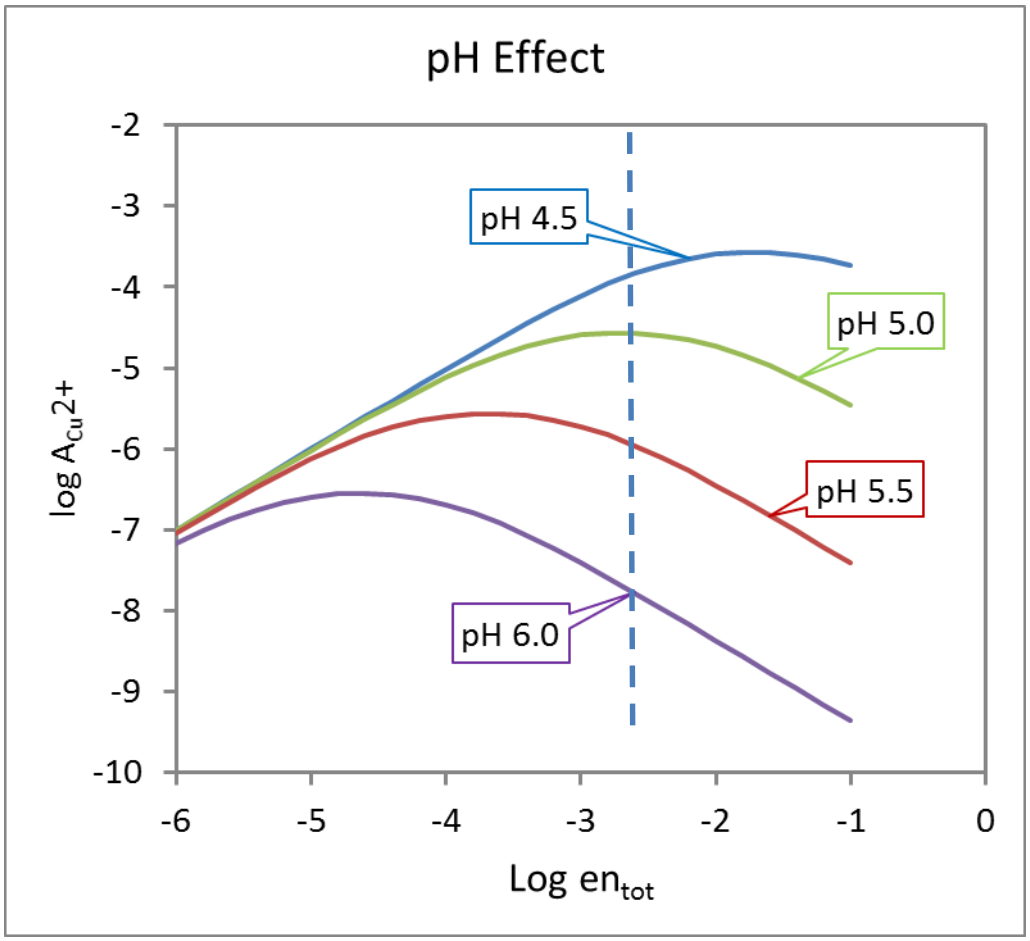

Figure 5.9. The effect of pH and the log en_{tot} starting point on metal anti-buffering. The dashed line indicates the log en_{tot} value used in the actual experiments.

5.11 Conclusions

Using the composition grid approach to examining metal-ligand complexation systems led to the discovery of an unanticipated phenomenon which has been named metal anti-buffering. Its existence suggested a series of dilution

experiments that could be conducted to confirm its existence. The experimental results nicely followed the model's predicted behavior with respect to both overall shape and extent of the behavior. Some further refinement in thermodynamic constant selection, activity corrections and electrode behavior are needed to optimize agreement between experiment and model traces.

Anti-buffering is not a behavior that is seen over a wide range of possible solution compositions. It is restricted to situations in which the ligand is present in excess over the metal and where higher stoichiometries dominate the protonation constants for the ligands. Where it does occur, however, the effect can be dramatic. Modeling of the Cu-NTA monoamide system, for example, predicted an anti-buffering effect of 18 orders of magnitude. This would be difficult to demonstrate in an experiment, however, because the levels of free Cu^{2+} are far too low to measure with anything other than nuclear methods.

Could anti-buffering ever be observed in a real-world setting? Modeling the Cu-ammonia system suggests that it could happen. If a small influx of acid mine drainage entered a larger body of water that was strongly buffered and had a high natural ammonium ion content, anti-buffering could occur. Furthermore, this could impact the partitioning of a toxic metal into an organism if it is the uncomplexed form that transports through cell membranes.

Irrespective of it possible significance in the real world, anti-buffering is a strong example of how the composition grid topo approach helps reveal new and unexpected chemical behavior in aqueous systems.

References

1. Wanninen, E.V.; Ingman, F. Metal buffers in chemical analysis: Part I-Theoretical considerations pure & Appl. Chem. 1987, 59, 1681-1692.
2. Wanninen, E.V.; Ingman, F. Metal buffers in chemical analysis: Part II-Theoretical considerations pure & Appl. Chem. 1991, 63(4), 639-642.
3. Perrin, D. D.; B. Buffers for pH and Metal Ion Control'', Chapman and Hall, London, 1974, Ch. 7, pp77-103.
4. MacCarthy, P.; Smith, G.C. Stability Surface Concept- A Quantitative Model for Complexation in Multiligand Mixtures Chemical Modelling in Aqueous Systems, ACS Symposium series, 1979, Ch. 10, 201-222.
5. Baes, C. F., Jr. and Mesmer, R. E. (1976) The Hydrolysis of Cations: John Wiley & Sons, New York, pp269.
6. Paoletti, P. Formation of Metal Complexes with Ethylenediamine: A Critical Survey of Equilibrium Constants, Enthalpy and Entropy Values, pure & Appl. Chem. 1984, 56(4), 491-522.
7. Silva, J. A.; Felcman, J.; Merc, A.L.R.; Mangrich, A.S.; Lopes, R.S.C.; Lopes. C. C. Study of binary and ternary complexes of copper (II) with some polyamines and adenosine 5' triphosphate Inorg. *Chim. Acta*, 2003, p. 155-166.
8. Davies, C.W. Ion Association. London: Butterworth, 1962, pp. 37–53.
9. Smith, G.C., Quantification of Metal Ion Complexation in Multiligand Mixtures, Ph.D. Thesis, Colorado School of Mines, 1983.
10. Perrin, D. D. Dissociation Constants of Organic Bases in Aqueous Solution, 1965**.**
11. Martell, A.E.; Smith, R.M. Critical Stability Constants, Plenum Press, New York, 1974.

12. Sposito, G.; Holtzclaw, K.; LeVesque-Madore, C. S. Calcium ion complexation by fulvic acid extracted from sewage sludge-soil mixtures. Soil sci. Soc. Am. J. 1978, 42(4), 600-606.
13. Burgess, John Metal Ions in Solution. Chichester: Ellis Harwood, 1978.
14. Stella, R., Ganzerili-Valentini, M. T. Copper Ion-Selective Electrode for Determination of Inorganic Copper Species in Fresh waters, Analytical Chemistry, 1979, 51(13), 2148-2151.

Chapter 6

Why Batteries Deliver a Fairly Constant Voltage until Dead

6.1 Introduction

Have you ever wondered why batteries seem to be working fine right up to the moment that they fail? You get a warning “low battery” and shortly thereafter your flashlight or electronic device quits working. Hopefully, you have some spare batteries to install and you backed up your data. Once you are close to failure, batteries slip from “weak” to “dead” in a very short time. So how can the batteries be okay one minute and not the next? To understand how batteries behave, one must understand how the Nernst equation describes the voltages produced in a Galvanic cell. After all, batteries are a nothing more than a type of Galvanic cell. This paper shows how the voltage behaves over the lifespan of a battery. The voltage is fairly constant until it suddenly plummets as one of the component species is exhausted.

6.2 The Nernst Equation Viewed as a Surface

The Nernst equation (Equation 6.1) for a half-reaction is typically given as:

$$E = E^0 + \frac{RT}{nF}\ln\frac{A_{Ox}}{A_{Red}} \qquad (6.1)$$

where E is the half-cell potential expressed in volts, E^0 is the half-cell standard reduction potential for unit activity and 298.15 K, R is the universal gas constant, T is the absolute temperature, n is the number of electrons transferred in the half-reaction, F is the Faraday constant, A_{Ox} is the activity of the oxidized form of the redox couple, and A_{Red} is the activity of the reduced form of the redox couple. The

two most important terms in eq 6.1 on which to focus are (1) the half-cell standard reduction potential, E^0 and (2) the logarithmic term, $\ln(A_{Ox}/A_{Red})$. The E^0 largely controls the voltage of the half-reaction while the battery is "doing fine". As the battery is "going dead", the logarithmic term suddenly dominates. The interplay between the two terms becomes easy to see when you view a three-dimensional plot of the Nernst equation using linear axes that extend to relatively high activities. Its appearance also depends on whether the species involved in the half-reaction are in aqueous solution versus in a solid or pure liquid state. We will begin with a wet cell that corresponds to half-reactions for which both the oxidized and reduced forms of the redox couple are present in the aqueous phase.

To look at all possible voltages that an aqueous redox couple could generate, we need to build a grid that holds the full range of activities for both forms. The range of the oxidized form's activity will be indicated on the y axis and the range of the reduced form's activity on the x axis. The two axes represent the balance between oxidized and reduced forms of the substance comprising the redox couple (not the reactants). Substituting a specific ratio of A_{Ox}/A_{Red} into the Nernst equation generates a single voltage, E. A systematic substitution of many A_{Ox}/A_{Red} ratios that cover the full activity range of both forms yields a collection of voltages that can be plotted on a z axis above the grid. This set of voltages collectively describes a three-dimensional picture of the Nernst equation behavior. Figure 6.1 illustrates the Nernst potential surface for the half-reaction $Fe^{3+} + e^- \rightleftarrows Fe^{2+}$ with $E^0 = 0.770$ V[3]. What is compellingly obvious in looking at the Nernst potential surface in Figure 6.1 is that a large portion of it is flat. What is more, the voltage corresponding to the flat region is essentially equal to 0.770 V,

the E^0 value! (The definition of E^0 is shown as the grid point at the right-hand back corner of the surface, that is, the point at which both A_{Fe}^{2+} and A_{Fe}^{3+} are at unit activity.) Given the linear axes of the grid, the voltage for a redox couple never moves far from the E^0 value over most ratios of Fe^{3+} to Fe^{2+}. It is only when either A_{Fe2+} or A_{Fe3+} approach extremely small values that the potential begins to change. Once there, however, the change is dramatic; it rises or falls at an exponential rate.

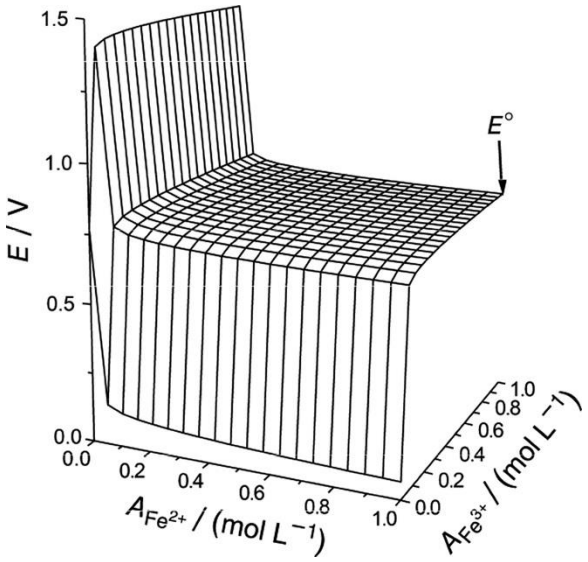

Figure 6.1. The Nernst potential surface for the $Fe^{3+} + e^- \rightleftarrows Fe^{2+}$ aqueous redox couple. All E0 values for this paper are from ref 3. Note that E values plotted for zero activity correspond to 10^{-12} M to avoid ±∞.

In fact, the surfaces along both axes have been artificially truncated by using an activity of 1.0×10^{-12} M instead of 0.0 M. At activities of 0.0 M, the surface would theoretically rise to +∞ along the y axis and drop to −∞ along the x axis. The Nernst equation basically says that E^0 is the predominant contributor to the potential for a linear surface half-cell everywhere except immediately adjacent to the two axes. As will become apparent later in this paper, the flatness of the linear grid Nernst potential surface for most A_{Ox}/A_{Red} ratios is responsible for the

relatively steady voltage delivered by a battery during its working life. The second term on the right-hand side of eq 6.1, $(RT/nF)\ln(A_{Ox}/A_{Red})$, is an "adjustment factor" for fluctuations in the ratio of the oxidized and reduced forms. It does not have much impact on the computed value of E when the A_{Ox}/A_{Red} ratio is fairly close to unity. With linear axes, the impact is small for most grid points. Because the activity ratio is preceded by a natural logarithm operator and the natural logarithm of 1 is equal to 0, not much voltage adjustment is needed until the ratio departs significantly from 1. Furthermore, the coefficient preceding the logarithmic term is equal to 0.05917 at 298.15 K. Unless the A_{Ox}/A_{Red} ratio has changed greatly, its impact is further attenuated by this small coefficient. A detailed examination of the plateau region reveals that equipotential lines radiate outward from the origin like spokes on a wheel because these denote constant values for the A_{Ox}/A_{Red} ratio. In fact, the line between the origin and E^0 is the locus of points for which $A_{Fe2+} = A_{Fe3+}$ and the second term of the Nernst equation goes to zero. Points to the right of that line are slightly lower than E^0 and points to the left are slightly higher. As soon as one form of the redox couple is nearly depleted, the "adjustment factor" suddenly becomes an important determiner of the half-cell potential. The act of discharging a Galvanic cell corresponds to moving diagonally toward one axis or the other at a steady rate. Thus, when the left-hand "wall" or the front "face" is approached, any additional movement quickly changes the half-cell potential. This rapid change in potential is responsible for the quick demise of a failing battery.

6.3 Galvanic cells

A Galvanic cell involves two half-reactions, one for the anode half-cell and one for the cathode half-cell, so two Nernst surfaces are needed to display the sequence of potentials that occur as a totally aqueous cell operates. For purposes of illustration, consider a wet-chemistry-based Galvanic cell in which Fe^{3+} at unit activity in one half-cell oxidizes Cu^{+} at unit activity in the other half-cell (Figure 6.2).

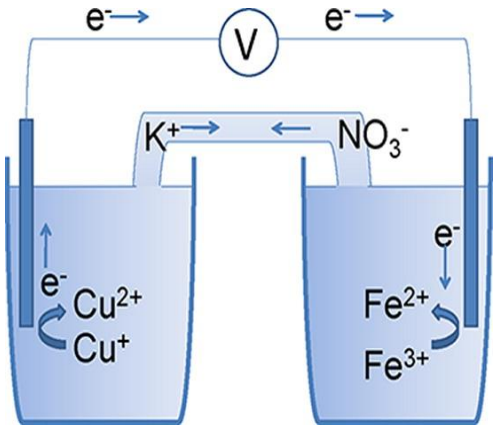

Figure 6.2. Diagram for a wet Galvanic cell with aqueous iron and copper species.

The cathode reaction is given by the same iron redox couple cited earlier, namely, $Fe^{3+}+e^{-} \rightleftarrows Fe^{2+}$ (E^0 = 0.770 V). The anode reaction (which runs in reverse as it has the lower E^0) is given by the standard reduction potential $Cu^{2+} +e^{-} \rightleftarrows Cu^{+}$ (E^0 = 0.158 V). Just as it takes two half-cells to form a Galvanic cell, it takes two Nernst surfaces to illustrate the behavior of the half-cell potentials that accompany its operation (Figure 6.3). The upper Nernst surface represents iron. The reduction path (shown in green) starts with the Fe^{3+} at unit activity and Fe^{2+} essentially absent. As the Fe^{3+} is consumed, it is converted to Fe^{2+}. Thus, the ratio of A_{Fe3+}/A_{Fe2+} moves diagonally down and to the right on the composition grid. The potential drops instantaneously from an initial high value on the left-hand wall

down to a value near E^0 on the flat plateau area of the Fe surface. The lower Nernst surface represents the copper half-cell. The oxidation path (shown in red) starts with Cu^+ at unit activity and Cu^{2+} essentially absent. As the cell operates, the Cu potential rapidly ascends to the plateau region of the Cu surface. The Fe^{3+} reduction reaction continues to be spontaneous as long as the iron half-cell potential is greater than that in the Cu half-cell. Because the entire Fe^{3+}/Fe^{2+} plateau is well above that for Cu^{2+}/Cu^+, the reaction path moves diagonally across the surface until it hits the front face. When the Fe^{3+} is nearly depleted, the potential quickly plummets.

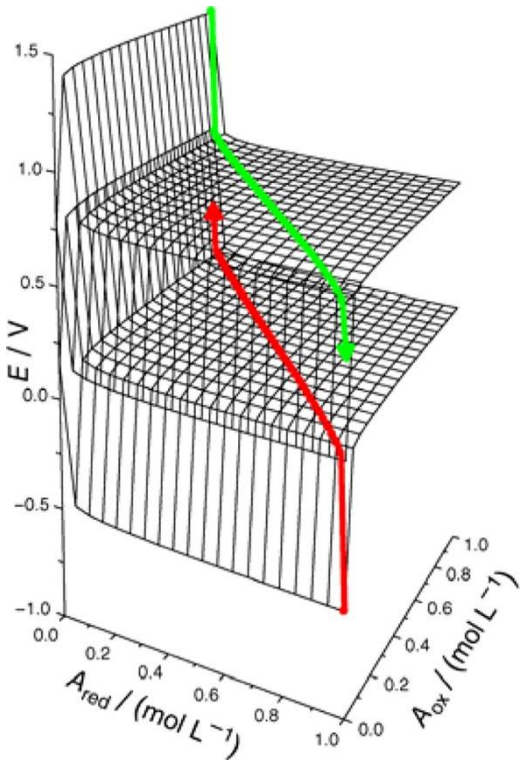

Figure 6.3. Nernst surfaces for a wet Galvanic cell shown in Figure 2 with iron (upper) and copper (lower). The reduction half-reaction is tracked on the iron surface; the oxidation half-reaction is tracked on the copper surface. The cell dies when the two paths are at the same z value.

The Cu^{+} oxidation path rises from its start on the front face, progresses diagonally across its plateau to its left-hand wall, and then begins to rapidly climb when the Cu^{+} is nearly gone. The Galvanic cell reaction stops ("dies") when the dropping Fe^{3+} path and the rising Cu^{+} path achieve the same potential. Given the symmetry of these two hypothetical half-cell reactions, the equilibrium point corresponds to a potential exactly half way between the two plateaus, that is, $E_{Fe} = E_{Cu} = (0.770 + 0.158)/2 = 0.464$ V. Figure 6.3 is a visual depiction of the two explanations promised in the title of this paper: Why Batteries Deliver a Fairly Constant Voltage until Dead. The voltage delivered by an operating cell is dictated by Ecell, the vertical spacing between the two colored discharge reaction paths. Because the paths traverse essentially horizontal planes, the voltage difference is nearly constant. The reason batteries suddenly die is a result of the discharge path leaving the planar portion of the Nernst surface. When a reduction path drops over the front face or an oxidation path rapidly rises up the back wall or both, the voltage difference rapidly diminishes to zero and the cell dies. Given a constant current draw on the cell, the rapid voltage change happens over a very short stretch of the reaction path. It is a "sudden death" phenomenon.

6.4 Batteries utilizing solid or pure phase redox species

Nernst potentials for dry cell batteries are vastly simpler in appearance than those for wet cells. This is because the variables in the logarithmic term of the Nernst equation are restricted to aqueous species. The activity of a solid phase or a pure liquid phase is always unity. The Nernst potential for these reactions is often a function of only one redox species. Thus, a single trace captures the series of potentials that are encountered during a discharge event. A surface is not

needed. As an illustrative example, consider the mercury oxide battery that was commonly used for watches, cameras, and pacemakers until environmental disposal concerns led to its being phased out[4]. The half-reactions for a mercury oxide cell are typically given as[5]:

$$\text{Anode: } Zn(s) + 2\ OH^-(aq) \rightarrow Zn(OH)_2(s) + 2\ e^- \qquad (6.2)$$

$$\text{Cathode: } HgO(s) + H_2O(l) + 2\ e^- \rightarrow Hg(l) + 2\ OH^-(aq) \qquad (6.3)$$

Both reactions are really net reactions for two-step processes (Figure 6.4). Even though these batteries are referred to as dry cells, they usually have some liquids present in a paste or gelled state. This is apparent from the presence of the $OH^-(aq)$ species in both eqs 6.2 and 6.3. The anode reaction involves a redox step:

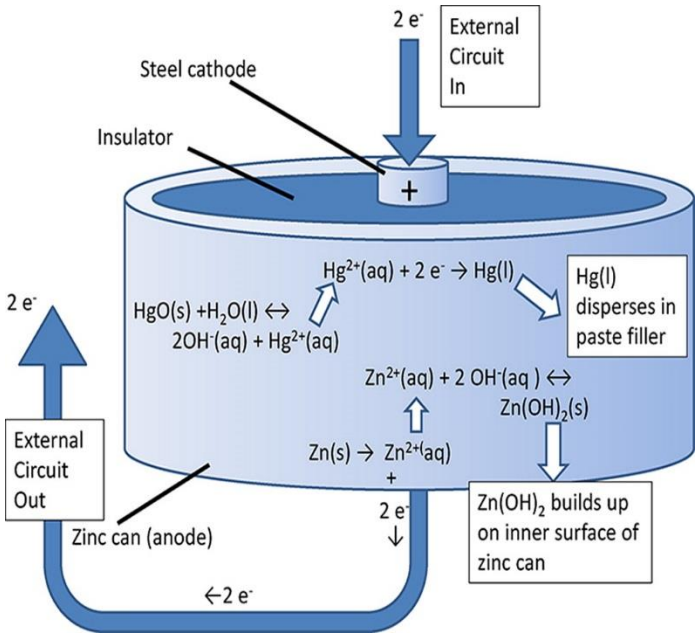

Figure 6.4. Diagram for a mercury oxide dry cell battery. Chemical reactions illustrate the two-step process at each electrode.

$$Zn(s) \rightarrow Zn^{2+} + 2\ e^- \qquad (E^o = -0.763\ V) \qquad (6.4)$$

Followed immediately by a precipitation event:

$$Zn^{2+} + 2\ OH^-(aq) \rightarrow Zn(OH)_2(s) \qquad (6.5)$$

The cathode reaction involves a dissolution step:

$$HgO(s) + H_2O(l) \rightarrow Hg^{2+}(aq) + 2\ OH^-(aq) \qquad (6.6)$$

And then a reduction step:

$$Hg^{2+}(aq) + 2\ e^- \rightarrow Hg(l) \qquad (E^o = 0.851\ V) \qquad (6.7)$$

As the battery discharges, the zinc "can" of the battery is converted into zinc hydroxide (or zinc oxide) that coats the inside of the remaining zinc can.

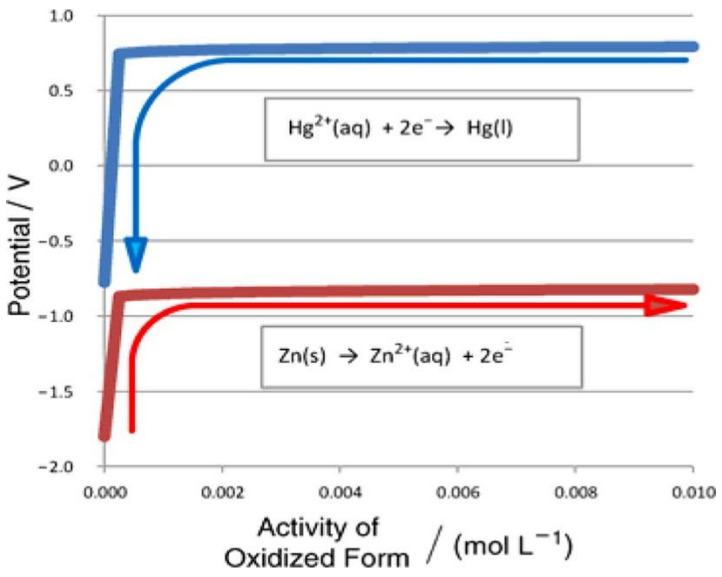

Figure 6.5. Nernst potential traces for a mercury oxide dry cell battery. Traces are based on the redox reactions of eqs 6.4 and 6.7 using an activity range of 0.000−0.010 M. The lower end of each trace was artificially truncated to avoid a −∞ V result from the Nernst equation.

Mercuric oxide dissolves to a slight extent and the Hg^{2+} ions formed can then pick up electrons from the cathode and change into liquid mercury. The liquid mercury

disperses throughout the paste or gel filled core of the battery. (If the mercury did not disperse, the cell would be rechargeable.)The Nernst potentials are predominantly regulated by the two redox half-reactions shown in eqs 6.4 and 6.7. A plot with two traces is sufficient to display the series of potentials that occur during a mercury oxide battery discharge (Figure 6.5).

The upper trace represents the reduction half-cell potentials whereas the lower trace follows the oxidation half-cell potentials. The theoretical voltage available between eqs 6.4 and 6.7 is (0.851 V) − (−0.763 V) = 1.614 V. Generally, mercury cells deliver an open circuit voltage of about 1.4 V due to resistance losses, differences in ion mobilities, accumulation of species at the metal electrode surfaces, and circuit over-potentials. Once again, the trends in the two traces provide a visual explanation for the cell behaviors incorporated into the title of this paper. First, as there is essentially a constant vertical difference between the two traces over most activities, the cell output voltage will be relatively constant. Second, the battery will die suddenly because the upper mercury trace exponentially drops when Hg^{2+} is depleted. As the plunging upper mercury trace hits the slowly rising potential of the lower zinc trace, the cell dies.

6.5 Some additional teaching points with Nernst surfaces

Galvanic cells are a frequently encountered topic in chemical education.[6–10] Their use typically falls into one of two categories: use as a source of energy as batteries[11] or use in analytical measurements via pH or ion selective electrodes.[12–15] The Nernst surface approach provides a nice way to contrast how the potentials are used in the two applications by illustrating the difference

between displaying the Nernst equation on linear versus logarithmic scales. Battery applications are best understood using a linear composition grid; analytical measurements employing electrodes are best under-stood using a logarithmic composition grid. The surface shown in Figure 6.1 has linear grid axes that extend to 1.0 M, a large value compared to those found in most real solutions. This was done expressly to illustrate the grid-point that defines the E^0 conditions. The Nernst surface looks the same for smaller ranges of activities as long as it is still plotted on a linear set of axes. Restriction of the activity range to a maximum value of 0.01 M makes essentially no perceptible difference in the appearance of the Nernst surface (Figure 6.6).

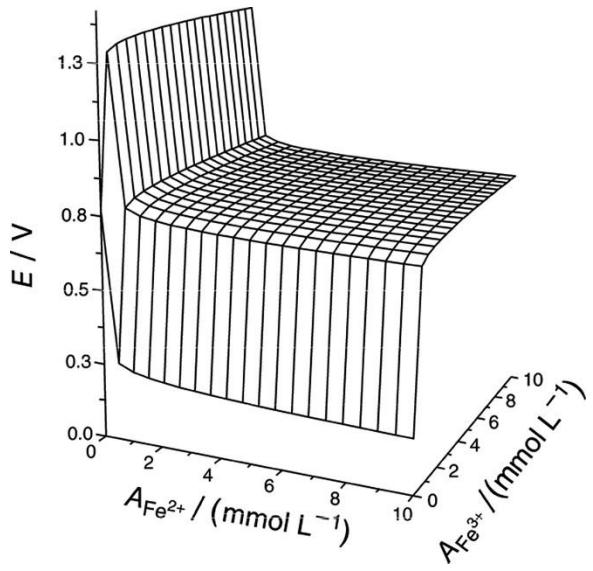

Figure 6.6. Linear-grid Nernst surface with maximum activity of 0.01 M.

The region of rapid change is still completely contained within the first grid interval. The potentials generated by the Nernst equation will be dominated by E0 whenever they are plotted on linear scales and are associated with the relatively high levels of ions that are present in batteries. The logarithmic term is only a

minor contributor until battery failure. An analogous effect is seen in acid−base chemistry with the Henderson−Hasselbalch equation[16] and the pH value of a buffer solution:

$$pH = pK_a + \log\frac{[base\ form]}{[acid\ form]} \qquad (6.8)$$

When significant quantities of both an acid and its conjugate base form are present, it is largely the pK_a value that determines a buffer pH, not the logarithmic term that contains the ratio of acid- to base-forms. A buffer possesses a relatively stable value until its capacity is exceeded. Then, it, too, shows rapid pH changes.

Plotting the Nernst surface over a logarithmic grid reveals an entirely different look. The logarithmic axes yield a sloped surface that is perfectly planar (Figure 6.7). The planar behavior is the basis for another extremely useful application of the Nernst equation, namely, using the observed potential of a sensing electrode to measure the activity of an aqueous analyte. The logarithmic scales permit useful information to be extracted over many orders of magnitude. We selected 1×10^{-9} M to 1 M in Figure 6.7 to include the working range of most commercial ion selective electrodes. Electrodes for determining pH, for example, depend on a linear response of 59.17 mV for each order of magnitude change in H^+ activity. The sensing electrode is one half-cell in a Galvanic cell. The other half of the Galvanic cell is maintained at a constant potential by means of a reference half-cell, typically Ag/AgCl. All change in the overall cell potential is attributable to the change in the analyte activity.

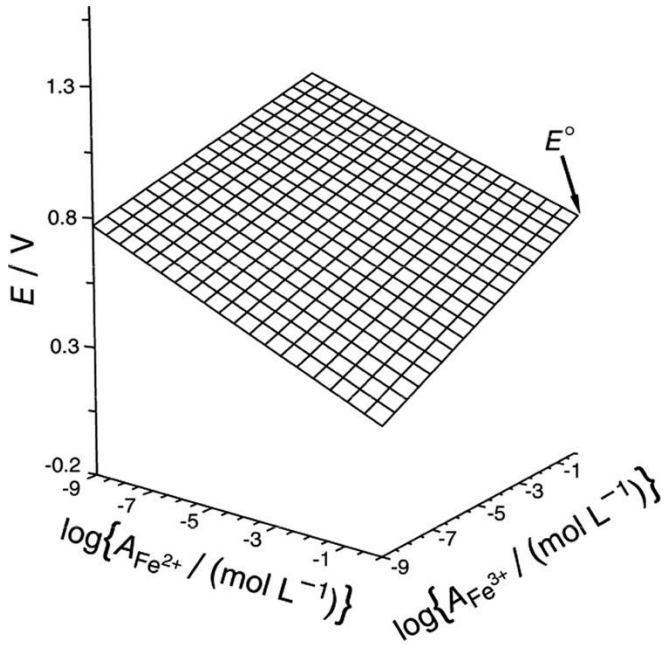

Figure 6.7. Logarithmic-grid Nernst surface with maximum activity of 1.0 M.

Other ion selective electrodes have been developed to follow the activities of a number of charged species in solution such as Cl^-, F^-,Cu^{2+}, and Ag^+. For upper-level analytical courses, the linear surfaces give a unique visualization of exactly what E^0 represents. The conditions that define E^0 are not a very practical solution and it is unlikely that they will be encountered in an actual experiment. On the other hand, it is quite likely that a potential equal to E^0 will be encountered when equal activities of the oxidized and reduced forms are present, such as half way to an equivalence point in a redox titration. Students should realize that the diagonal locus of points from the origin to E^0 (at the 1.0 M, 1.0 M grid point) are all equipotential. Finally, the concept of mapping experimental paths onto a composition grid forces students to consider the sequence of compositional changes that relate to procedures carried out on a system.[17] The redox paths shown in this paper that correspond to cell discharges form paths that angle

across the grid with negative slopes. They are easy to understand because there are no volume changes that accompany the redox reactions. If you ask the students to characterize what happens during a dilution procedure on the linear grid, they should respond with a path that tracks from its starting coordinates and proceeds straight toward the origin. Because the ratio of oxidized to reduced form does not change, all points will be at an equipotential voltage. A more challenging exercise would ask students to plot the experimental path for a redox titration. The use of composition grids helps students visualize the behavior of an aqueous equilibrium concept over a universe of possible concentrations. Realizing how compositions of a system change during experimental procedures such as titrations or dilutions will deepen their appreciation of some subtle points. Papers exploring composition grids for acid− base, metal complexation, and solubility equilibrium in aqueous solution are in preparation. Shows essentially two types of features. Parts of it are flat spots and the other parts are cliffs. Flat spots are responsible for the near constancy of the voltage. The voltage for a half-cell remains quite close to its E^0 value over most of its useful life because drawing a current (a linear process) only makes small changes in species' activities. Furthermore, the impacts of these small changes are damped by the logarithmic nature of the second term in the Nernst equation (eq 6.1) and its small coefficient of 0.05917. It is only when a redox species is nearly depleted, that drawing a current can suddenly change its activity by orders of magnitude. Under these conditions, the logarithmic term quickly goes from being inconsequential to being dominant. These are cliff events on the plots. The cell dies as the difference between the two half-cell potentials diminishes. Equilibrium, another term for a dead battery, is rapidly approached.

References

1. Nernst, W. Z. Phys. Chem. 1889, 4, 129−181.
2. Peters, R. Z. Phys. Chem. 1898, 26, 193−236.
3. Weast, R. C., Ed. Handbook of Chemistry and Physics, 53rd ed; CRC: Cleveland, OH, 1972; pp D−111.
4. Smith, M. J.; Gray, F. J. Chem. Educ. 2010, 87, 162−167.
5. McMurry, J.; Fay, R. Chemistry, 3rd ed.; Prentice Hall: Upper Saddle River, NJ, 2001; p 784.
6. Chambers, J. Q. J. Chem. Educ. 1983, 60, 259−262.
7. Ciparlck, J. D. J. Chem. Educ. 1991, 68, 247.
8. Probst, D. A.; Henderson, G J. Chem. Educ. 1996, 73, 962−964.
9. Mills, K. V.; Herrick, R. S.; Guilmette, L. W.; Nestor, L. P.; Shafer, H.; Ditzler, M. A. J. Chem. Educ. 2008, 85, 1116−1119.
10. Peckham, G. D.; McNaught, I. J. J. Chem. Educ. 2011, 88, 782−783.
11. Treptow, R. S. J. Chem. Educ. 2002, 79, 334−338.
12. Lamb, R. E.; Natusch, D. F. S.; O'Reilly, J. E.; Watkins, N. J. Chem. Educ. 1973, 50, 432−434.
13. Light, T. S.; Cappuccino, C. C. J. Chem. Educ. 1975, 52, 247−250.
14. Meyerhoff, M. E.; Kovach, P. M. J. Chem. Educ. 1983, 60, 766−768.
15. Li, G.; Polk, B. J.; Meazell, L. A.; Hatchett, D. W. J. Chem. Educ. 2000, 77, 1049−1052.
16. Harris, D. Quantitative Chemical Analysis. 8th ed.; Freeman: New York, 2010; p 172.
17. MacCarthy, P J. Chem. Educ. 1984, 63, 339−343.

Chapter 7

Visualizing the Nernst Equation and Galvanic Cells via 3-D Surfaces

7.1 Introduction

Most introductory and analytical chemistry courses apply the Nernst equation to calculate potentials in redox problems. But many subtle aspects of aqueous redox equilibria are missed by simply looking at the calculated results for a single set of solution conditions. Take, for example, the difference between calculating the potential for a single solution composition versus the series of potentials in a redox titration curve. The titration curve possesses much richer information for the reader to understand as the solution composition systematically approaches and passes an equivalence point. Even more insights are available by adding a third axis for an even wider set of conditions. The additional axis allows the behavior of aqueous systems to be displayed over all possible ratios of the oxidized and reduced forms of the redox couple. The calculated potentials for the entire set of possible compositions (a composition grid) generate a three-dimensional surface. This paper uses three-dimensional surfaces to demonstrate how the Nernst equation behaves over a broad range of solution conditions. It shows how paths across the surface correspond to cell reactions as Galvanic cells operate. It also illustrates the effect of varying each parameter in the equation.

7.2 The Nernst Equation and the Redox Composition Grid

The Nernst equation (Equation 1), as typically used, should probably be called the Peters equation:

$$E = E^0 + \frac{RT}{nF}\ln\frac{A_{Ox}}{A_{Red}} \quad (7.1)$$

Where,

E is the potential expressed in volts,

E^0 is the standard reduction potential for unit activity and 298K,

R is the universal gas constant,

T is temperature in kelvin,

F is the Faraday constant,

and n is the number of electrons transferred in the reaction.

V.A. Shaposhnik[1] traces the role that Nernst played in developing the form of the equation that appears in most textbooks. In 1877 Helmholtz, Nernst's mentor, derived an equation for a Galvanic concentration cell – one in which both electrodes are identical and the electrolytes in the two half-cells differ only in concentration. In 1889 Nernst published a formula in which he replaced an empirical factor in the Helmholtz equation with one containing the familiar R, T, n and F parameters[2]. The equation conventionally called "the Nernst equation" first appeared in an 1898 paper by Rudolf Peters[3]. Peters and Nernst both worked for Ostwald at Leipzig University. The Peters equation is applicable not only to concentration cells, but also to cells in which the two half-reactions are completely distinct from one another.

Use of a novel, redox composition grid helps visualize the overall behavior of the Nernst equation. While composition grids have appeared in past papers discussing large-scale trends in aqueous equilibria, they have generally been associated with complexation reactions. They recorded the concentration of ligands on one axis and the concentration of metal on the other [4-7.] The redox

composition grid introduced here is different in that the two axes represent not two reactants, but the balance between oxidized and reduced forms of the substance comprising the redox couple. Figure 7.1, for example, displays the redox composition grid for the couple involving the single electron transfer between Fe^{3+} and Fe^{2+}. Any single calculation involving the Nernst equation corresponds to substituting in a specific pair of x,y-coordinates from the grid. The x-coordinate signifies the activity of the reduced form (A_{Fe}^{2+}) and the y-coordinate signifies the activity of the oxidized form (A_{Fe}^{3+}).

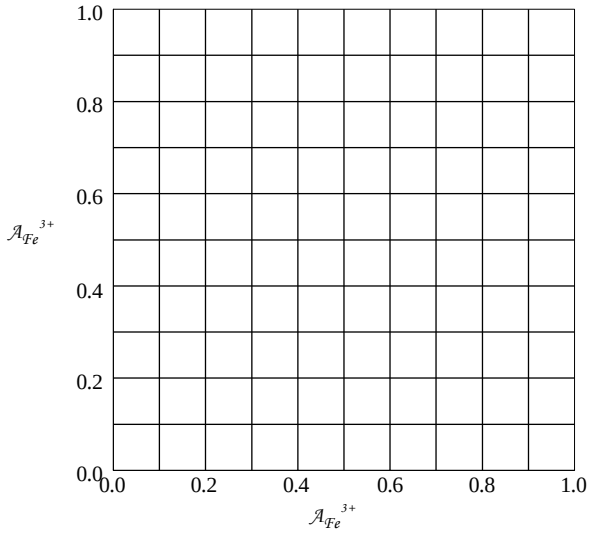

Figure 7.1. The redox composition grid for the $Fe^{3+} + e^- \rightarrow Fe^{2+}$ redox- couple.

7.3 Nernst Equation Surfaces for Single Redox Couples

Substituting every pair of (A_{Fe}^{2+}, A_{Fe}^{3+}) grid coordinates into the Nernst equation generates the third value needed as the z-coordinate to construct the Fe^{3+}/Fe^{2+} surface plot. Two versions of the redox grid are possible – one in which the x- and y-axes are linear (Figure 7.2, panel I) and the other in which the x- and y-axes are logarithmic (Figure 7.2, panel II). Each has its merits.

The linear-axis surface illustrates that the potential for a redox couple never moves far from the E^0-value over most ratios of Fe^{3+} and Fe^{2+}. The definition of E^o itself is associated with the grid point at the right-hand back corner of the surface, *i.e.,* the point at which both A_{Fe}^{2+} and A_{Fe}^{3+} are at unit activity. It is only when either A_{Fe}^{2+} or A_{Fe}^{3+} approach small levels that the potential begins to change. Once there, the change is dramatic. In fact, we have artificially truncated the surfaces along both axes by using an activity of 1.0×10^{-12} instead of 0. At activities of 0 the surface would rise to $+\infty$ along the y-axis and drop to $-\infty$ along the x-axis. The Nernst equation basically says that E^0 is the predominant contributor to the potential for a half-cell. The second term in the equation is a "correction factor" to adjust for fluctuations in the ratio of the oxidized and reduced forms. Note that the majority of the linear axis surface is essentially a plane at the level of E^0, namely, 0.771 V for the Fe^{3+}/Fe^{2+} example here. A detailed examination of the plane reveals that equipotential lines radiate outward from the origin like spokes on a wheel. The line between the origin and E^0 is the locus of points for which $A_{Fe}^{2+} = A_{Fe}^{3+}$ and the second term of the Nernst equation goes to zero. Points to the right of that line are slightly lower than E^0; points to the left are slightly higher. The logarithmic-axis surface is not quite as rich in new insights, but it does demonstrate the logarithmic variation in potentials as activities change over many orders of magnitude. The redox composition grid has been rotated in Figure 7.2, panel II to place the E^0-point at the front. This is necessary to make the rest of the surface easily visible. All but the nearest ten grid points of this surface correspond the x,y-coordinates on the linear-axes plot that are in the front face that drops toward $-\infty$ or the left-hand wall that rises toward $+\infty$.

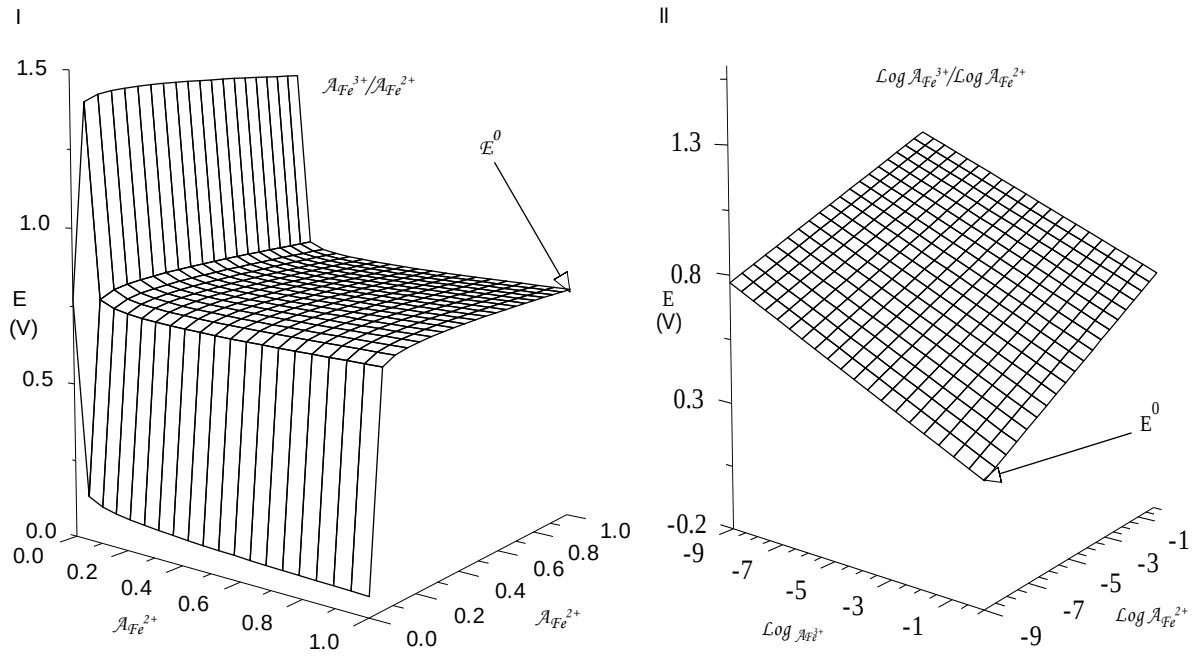

Figure 7.2. The Nernst surface for the $Fe^{3+} + e^- \rightarrow Fe^{2+}$ redox couple. Panel I – linear axes. Panel II – logarithmic axes. E^o values used here and in other plots are from Reference 8.

In other words, most grid-points on the logarithmic axis surface are nearly depleted in at least one form of the redox couple.

The Nernst equation surface on a linear set of axes looks largely the same no matter what the range of activities is employed. The axes for the redox composition grid of Figure 7.1 extended to activities of 1.0, a large value compared to those found in most real solutions. It was done expressly to illustrate the grid-point that defines the E^0 conditions. Restriction of the activity range on the linear axes to a maximum value of 0.1 or even 0.01 makes an almost imperceptible difference in the appearance of the Nernst surface (Figure 7.3). The only differences reside in the left-hand wall and the front face. These differences are mostly an artifact of maintaining an activity or 1.0×10^{-12} as a cut-off equivalent to zero. All other grid points retain the same $A_{Fe^{3+}}/A_{Fe^{2+}}$ ratio, so

the corresponding correction term values are identical. What does change, however, is the capacity of the system to respond to e^- fluxes. This point will be discussed further in the next section which addresses reaction paths on Nernst surfaces.

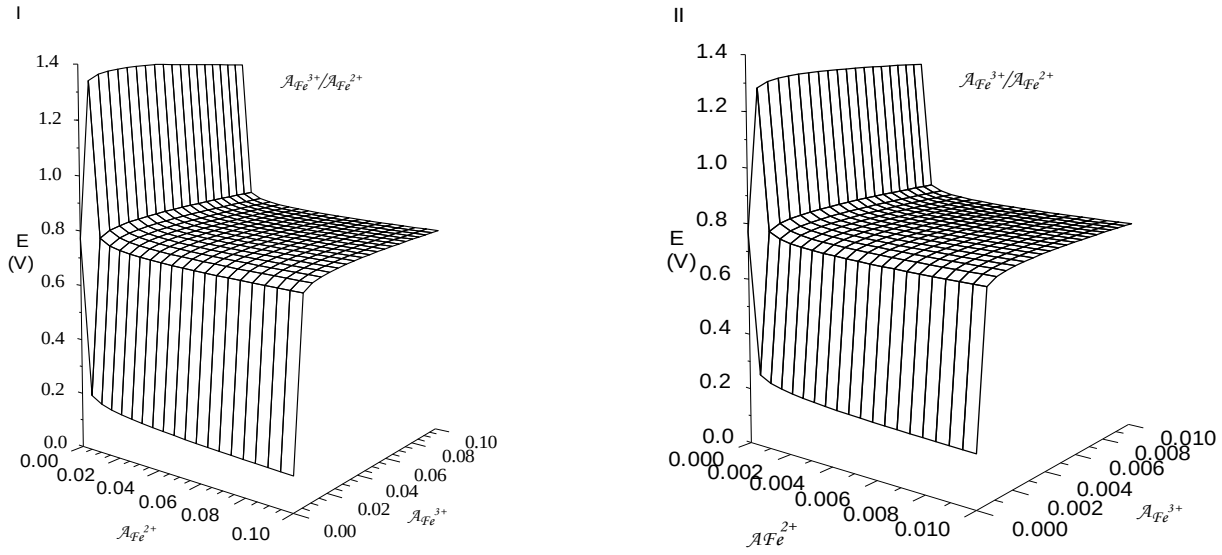

Figure 7.3. The Nernst surface for more dilute systems of the $Fe^{3+} + e^- \rightarrow Fe^{2+}$ redox couple. Panel I – 0.1 maximum activity. Panel II – 0.01 maximum activity.

Since the Nernst equation is written in terms of activities, how would a potential surface look when concentrations are used instead? Electrodes respond to activities, but real systems may contain significantly higher amounts of dissolved materials in them. Figure 7.4 represents an attempt to illustrate the differences in potentials that would be exhibited by building the redox composition grid on concentration axes rather than activity axes. The maximum concentration for both the reduced and oxidized forms was set at 0.001 M. A constant ionic strength was imposed on the system at 0.2 M. Experimentally this could be accomplished by using an ionic strength adjusting solution at all points. Thus,

activity coefficients are constant for each of the two species involved. The activity coefficient for Fe^{2+} at 0.2 M is given by Kielland's classic table[9] as 0.405. For Fe^{3+} the activity coefficient is 0.18. Because the activity coefficient is so much smaller for the trivalent Fe^{3+} ion, the ratio of Fe^{3+} to Fe^{2+} in the correction term of the Nernst equation has been reduced. The calculated potential for the corresponding grid point is lower than that of the activity surface. Beyond that, the overall shape of the surface is basically unchanged. There is a constant gap between the two plateaus and the left-hand wall and front face are correspondingly displaced.

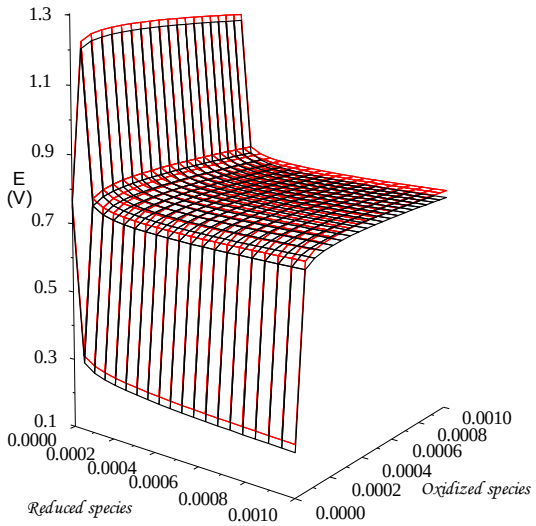

Figure 7.4. Comparison of the Nernst surfaces for $Fe^{3+} + e^- \rightarrow Fe^{2+}$ redox couple: concentration-based axes (lower - black) and activity-based axes (upper - red). For the concentration axis surface ionic strength was fixed at 0.2 M. Activity coefficients are from reference 9.

Use of 0.2 M as the ionic strength probably represents about the maximum discrepancy between an activity-based potential versus a concentration-based potential. If one were to calculate a surface for a system in which the ionic strength changes with the extent of reaction, there would be a slight downward

slope to the plateau. The end result is that the concentration-based system will have long-term trends that are not greatly different from the idealized activity surfaces.

7.4 Reaction paths

The richness of insights provided by viewing Nernst equation surfaces emerges when potentials for the series of points corresponding to a redox reaction are tracked across the grid. The section defines reaction paths for redox processes and then employs them to illustrate Galvanic and concentration cell reactions. It provides a visual depiction of a redox reaction's equilibrium point and a method for determining which direction for a cell reaction is spontaneous.

Given the manner in which the redox composition grids are constructed, any half-reaction that occurs will generate a slanted line across the grid with a negative slope. Reduction half reactions will proceed downward and to the right; oxidation half reaction will proceed upward and to the left. For a single electron transferred in a half reaction, the slope of the lines will always be -1.0 (Figure 7.5, Panel I) This is a result of the half-reaction stoichiometry. In the Fe^{3+}/Fe^{2+} redox couple, *i.e.,* $Fe^{3+} + e^- \rightarrow Fe^{2+}$, the coefficient for both Fe^{3+} and Fe^{2+} is one. For each Fe^{3+} that disappears in a reduction process, a Fe^{2+} appears. The converse is true in the oxidation reaction, for each Fe^{2+} that disappears, a Fe^{3+} appears. Half reactions that contain stoichiometries other than 1:1 will yield lines at other negative slopes (Figure 7.5, Panel II).

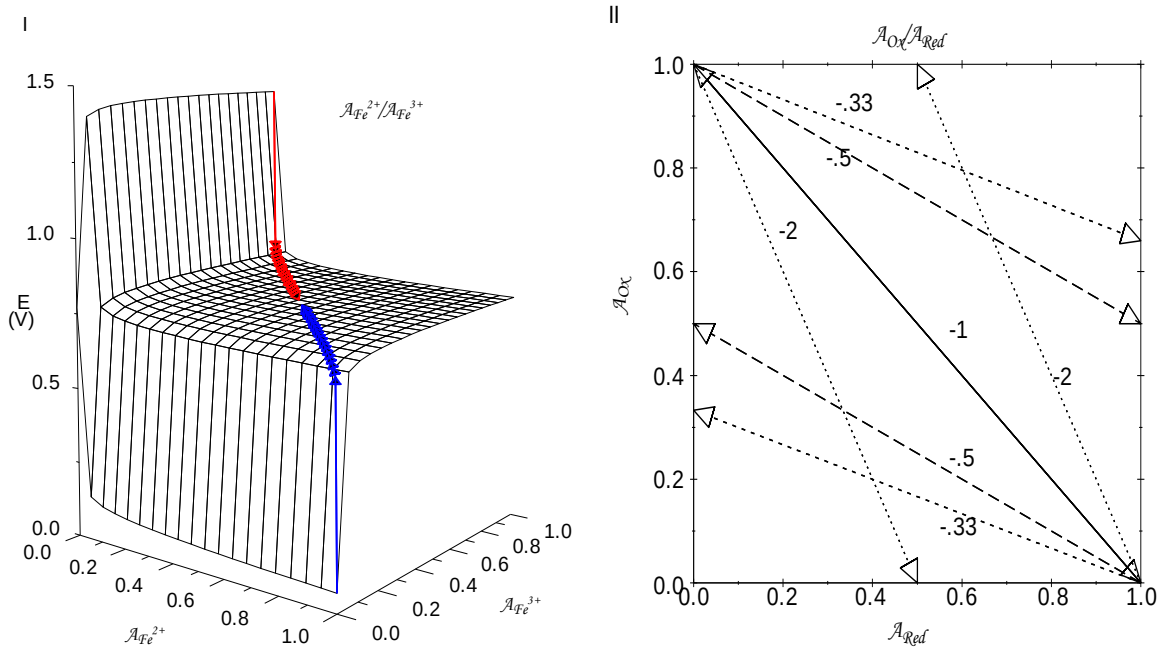

Figure 7.5. Reaction paths. Panel I – Reaction paths for $Fe^{3+} + e^- \rightarrow Fe^{2+}$ reduction (red) and $Fe^{2+} + e^- \rightarrow Fe^{3+}$ oxidation (blue) plotted on the Fe^{3+}/Fe^{2+} Nernst surface. Panel II – Projections of the reaction paths for various stoichiometries on the redox grid. Sample half reactions: $Br_3^- + 2\ e^- \rightarrow 3\ Br^-$ (slope -0.33); $Br_2(aq) + 2\ e^- \rightarrow 2\ Br^-$ (slope -0.5); $Fe^{3+} + e^- \rightarrow Fe^{2+}$ (slope -1.0); $2\ Rh^{3+} + 2\ e^- \rightarrow Rh_2^{4+}$ (slope -2.0).

A Galvanic cell involves two half reactions, one for each half-cell, so two Nernst surfaces are needed to display the sequence of potentials that occur as the cell operates. For purposes of illustration, consider a Galvanic cell in which Fe^{3+} at unit activity in one half-cell oxidizes Cu^+ at unit activity in the other half cell (Figure 7.6). As the Fe^{3+} is consumed, the potential drops from the left-hand wall down onto the Fe plateau area. The Fe^{3+} reduction reaction continues to be spontaneous as long as its potential is greater than that in the Cu half-cell. As can be seen in the figure, the entire Fe^{3+}/Fe^{2+} plateau is well above that for Cu^{2+}/Cu^+, so the reaction path moves diagonally across the surface until it hits the front face. As the Fe^{3+} is nearly depleted, the potential quickly plummets. At the same

time, the Cu^{+} oxidation path rises from its start on the front face, progresses diagonally across its plateau to its left-hand wall and then begins to climb as the Cu^{+} is nearly gone. The Galvanic cell reaction stops when the dropping Fe^{3+} path and the rising Cu^{+} path achieve the same potential. Given the symmetry of the two half-cell reactions, this corresponds to a point exactly half-way between the two plateaus.

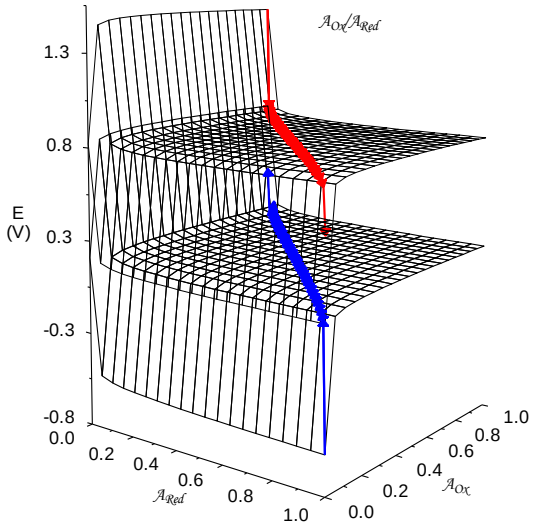

Figure 7.6. Galvanic cell. The upper surface represents the $Fe^{3+} + e^{-} \rightarrow Fe^{2+}$ redox path for a starting point with Fe^{3+} at unit activity and Fe^{2+} essentially absent. The lower surface represents the $Cu^{+} \rightarrow Cu^{2+} + e^{-}$ redox path for a starting point with Cu^{+} at unit activity and Cu^{2+} essentially absent. The Galvanic cell ceases to operate when the two path potentials are equal. For this symmetric pair of half-cell reactions, $E_{cell} = 0$ V halfway between the two E^{0} values ($E_{Fe\ path} = E_{Cu\ path} = 0.466$ V).

The Nernst surface approach nicely illustrates how concentration cells work, too. As noted earlier, these are the cells with which Nernst originally worked. They are a particular type of Galvanic cell, one in which both electrodes are identical and

the electrolytes in the two half-cells are also identical except in concentration. Only one Nernst surface is needed here.

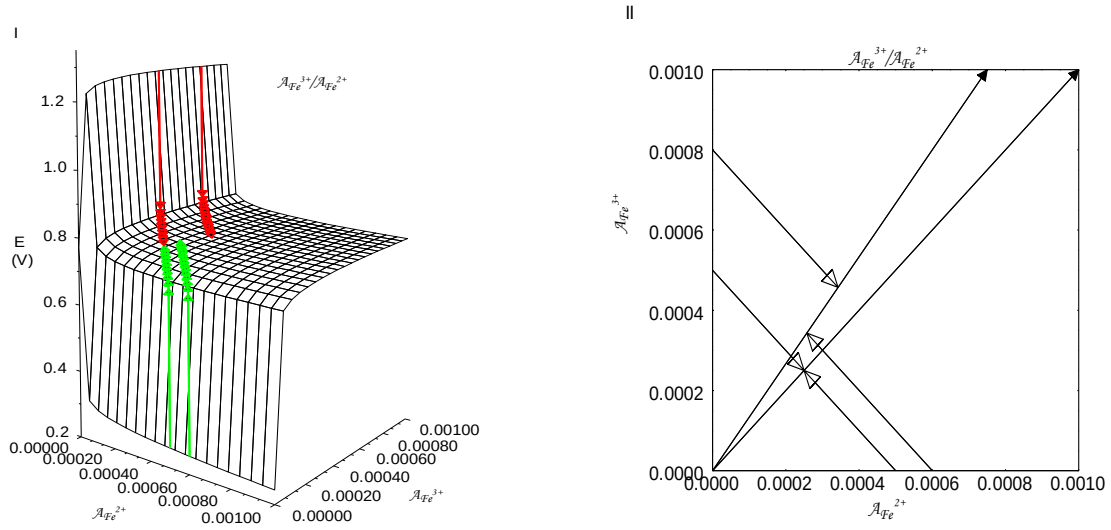

Figure 7.7. Concentration cell reaction paths for the Fe^{3+}/Fe^{2+} surface. The pair of reaction paths starting at an activity of 0.5 are for a symmetric system – both starting activity and volumes are the same magnitude. These meet at the surface diagonal where $E_{Red} = E_{Ox} = E^0$. The other pair of paths illustrate an asymmetric reaction. Both half-cells had identical volumes, but different activity levels. They meet at a non-diagonal point, but all other surface points with this E value define a line emanating out from the origin.

The driving force for the cell comes from choosing a pair of starting coordinates on the redox grid that have substantially different potentials. This generally means one half-cell will be enriched in the oxidized form of the couple (high on the left-hand wall) and the other half-cell predominantly holds the reduced form (a point low on the front face). Two pairs of starting points are illustrated in Figure 7.7. As the concentration cell operates, the two opposing reaction paths approach each other on the plateau. If the two half-cells started

with the same concentration and volumes of the active species, the two paths will meet on the plateau's diagonal where each half-cell will exhibit an E^0 voltage. If the two half-cells are different in starting concentrations or volumes of the active form, then the cell reaction will stop as the paths meet on another equipotential line that emanates out from the origin.

7.5 Varying "Correction Term" Parameters

The "correction term" of the Nernst equation, namely, $RT/nF \ln(A_{Ox}/A_{Red})$, includes a number of parameters that can affect the overall look of the resultant surface. These include n (the number of electrons transferred), T (the temperature), pH (if hydronium or hydroxide ions are included in the half-reaction) and solid/pure phases. This section details the changes imparted to the Nernst surface as each parameter listed above is changed.

The number of electrons transferred in the half reaction, n, appears in the denominator of the correction term. Its effect on linear surfaces is to alter the slope of the plateau. This is particularly noticeable where the plateau rises up against the left-hand wall or drops off of the front face. The higher the n-value, the flatter the plateau is as it approaches the left and front edges. In Figure 8, surfaces for two half reactions with different n-values are superimposed. The black surface for the single electron transfer between Fe^{3+} and Fe^{2+} exhibits a less abrupt curvature as is approaches the left wall and front face. It rises up at a distinctly faster rate at the back left edge of the plot. The flatter red surface for the three electron transfer between Cr^{6+} and Cr^{3+} can be seen below it.

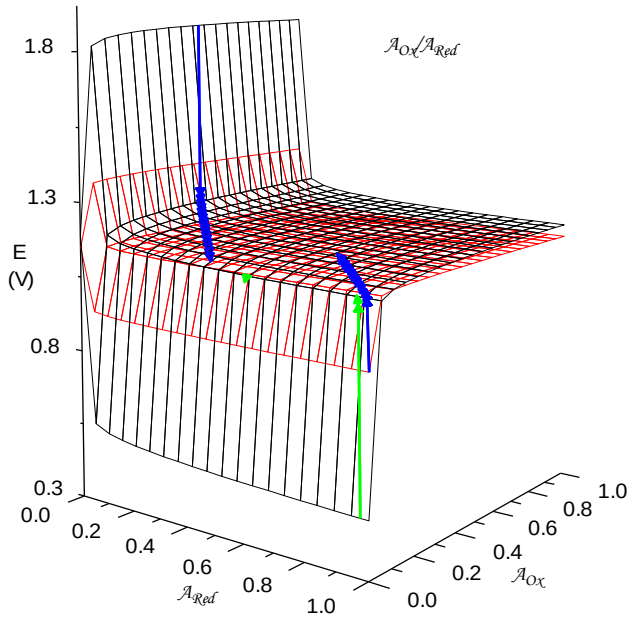

Figure 7.8. The effect of n on the Nernst surface plateau slope. The black surface corresponds to the $Fe^{3+} + e^- \rightarrow Fe^{2+}$ couple. The red surface corresponds to the $Cr^{6+} + 3e^- \rightarrow Cr^{3+}$ (in 2 M H_2SO_4) couple. The blue pair of reaction paths follows a spontaneous reaction between Fe^{3+} and Cr^{3+}. The red pair of reaction paths follows a spontaneous reaction in the opposite direction between Cr^{6+} and Fe^{2+}.

A close look at the right edge of the two surfaces reveals that the black surface curls down through the flatter red surface such that the black surface is below the red one at the front right corner. This leads to an interesting consequence for the direction of spontaneity in the cell. Over most possible half-cell compositions, the black Fe-surface is above the red Cr-surface so the spontaneous reaction will be Fe^{3+} oxidizing Cr^{3+} (e.g., blue reaction path pair). For a limited set of half-cell compositions, however, the spontaneous reaction is briefly in the other direction. Here Cr^{6+} oxidizes Fe^{2+} (green reaction path pair).

Changing the temperature of a half cell has two effects with respect to the Nernst surface. First, E^0 itself is a function of temperature, so the E^0 used for the

surface must be adjusted. Second, the appearance of T in the numerator of the "correction term" conveys a slight increase in the slope of the plateau portion of the surface. Both of these effects are seen for the Cu^{2+}/Cu^{+} couple in Figure 7.9. An upper limit of 100^0C was selected to accentuate the maximum effect of temperature changes in a aqueous medium. The E^o was corrected from its value of 0.161 V at 25^0C to 0.219 V at 100^0C. Since the E^0 at 100^0C is larger, the entire surface is displaced upward by the more dominating E^o-term of the equation.

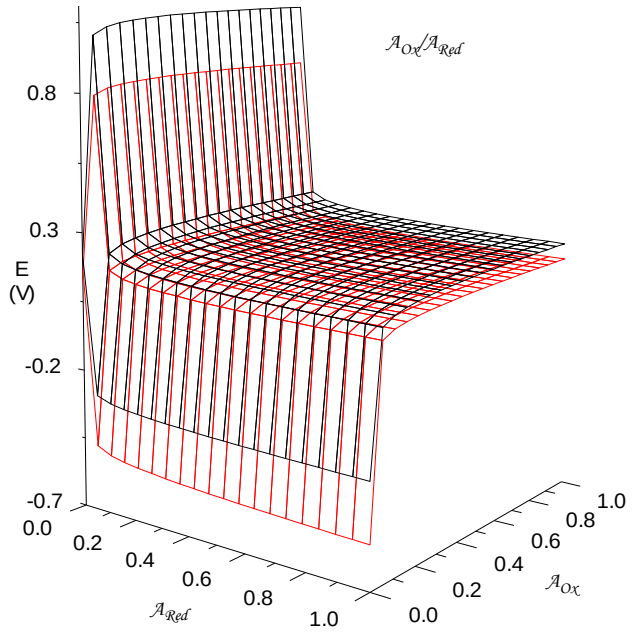

Figure 7.9. The effect of T on Nernst surfaces. Both surfaces represent the half reaction $Cu^{2+} + e^- \rightarrow Cu^+$. The lower red surface corresponds to a temperature of 25^0C (298.15 K). The upper black surface corresponds to a temperature of 100^0C (373.15 K). The E^0 was corrected for temperature using the relationship $E^0(T) = E^0 + (dE^0/dT)\Delta T$ [8].

The smaller, second effect of T in the "correction term" is seen in the slope of the upper surface's plateau. It is most easily seen at the back left corner where the 100-degree surface rises faster on its approach to the wall and in the front right corner where it rolls off sooner into the front face.

Many half-reactions include species that can undergo changes in activity other than the actual redox couple itself. The most common additional species are hydronium ion, H_3O^+, or hydroxide ion, OH^-.

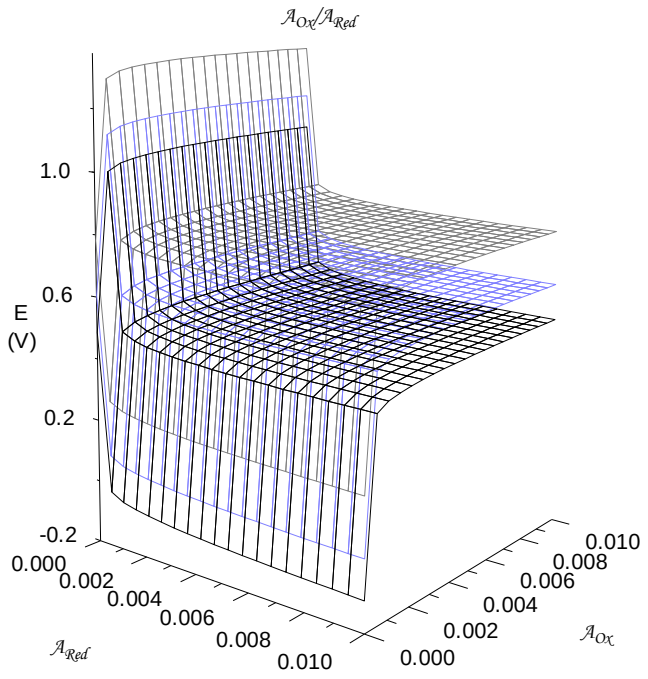

Figure 7.10. The effect of pH on a Nernst surface for a half-reaction containing H_3O^+. The half-reaction used here is $Fe(OH)^{2+} + H_3O^+ \rightarrow Fe^{2+} + 2\ H_2O$. Half-cell conditions fixed pH = 7.00 (lower surface), pH = 5.00 (middle surface), and pH = 2.00 (upper surface).

Their activities appear as extra terms in the logarithmic portion of the "correction term". Consider as an example the reduction of a $FeOH^{2+}$ complex ion. The half reaction is $FeOH^{2+} + H_3O^+ \rightarrow Fe^{2+} + 2\ H_2O$ with an $E^0 = 0.9$ The "correction term" for this reaction at 25^0C and with $\log_{10}$ is 0.05917 log ($A_{FeOH2+}A_{H3O+}/A_{Fe2+}$). At a fixed pH, the A_{H3O+} can be factored out as a second constant alongside the E^0 term, i.e., 0.05917 log A_{H3O+}. Because the A_{H3O+} will be less than 1.0, this term will always carry a negative sign and be more significant in magnitude as the pH rises. This is easily seen in Figure 7.9 where the surfaces for pH=2.0 (upper surface),

pH=5.0 (middle surface) and pH=7.0 (lower surface) are superimposed on the same axes. The surfaces are identical except for the added constant offset. In an experimental setting for which pH was not fixed, the potential would change 0.059 V for each pH-unit shift that the half-cell solution experiences. An additional complication would be the shift in complex ion activities, i.e., alpha coefficients for fractional composition diagrams, occasioned by any hydrolytic ligand interactions.

Nernst surfaces for cell reactions with a redox couple species that is a solid or pure liquid phase are less complicated than those already discussed. They will simply be missing the left wall or the front face depending on which species comprises the pure phase. Figure 7.10 shows an example of each. The upper surface is for a half-cell with a solid reduced form. Since its Nernst equation has no activity term in the denominator of the logarithm, it never increases toward $+\infty$ to form the left wall feature. In a similar fashion, the lower surface relates to a half-cell with a solid oxidized form. The Nernst equation for it has no activity term in the numerator of the logarithm. The ratio of species never goes to zero and its logarithm never plummets to form the front face. While pure phase surfaces carry no new information on the pure phase axis, they are still useful to view when interacting with other half cells that have both left walls and front faces.

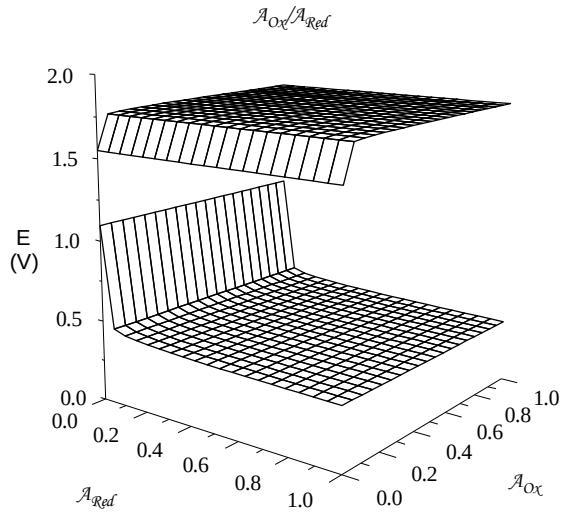

Figure 7.11. Nernst surfaces for half-reactions containing solids or pure liquid species. The upper surface is for a redox couple with a solid reduced form: $FeO_4^{2-} + 3\ H_2O + 3\ e^- \rightarrow FeOOH(s) + 5\ OH^-$ at pH = 10.00. The lower surface is for redox couple with a solid oxidized form: $FeOOH(s) + 3\ H_3O^+ + e^- \rightarrow Fe^{2+} + 5\ H_2O$ at pH = 2.0.

7.6 Conclusion

Use of composition grids to visualize equilibrium concepts holds much value to enhance the understanding of overall trends and subtle influences. This was personally experienced by the authors during the preparation of this manuscript. We originally envisioned about half of the figures that are included in this paper, but each surface prompted new questions and yielded new insights. This suggests that even more Nernst surface nuances are yet to be discovered. We are currently employing similar composition grid studies to investigate other aqueous equilibrium concepts.

7.7 Note

The calculations for each individual redox topo included in this chapter were performed through an Excel file named Redox TOPOS (Appendix II.C.). Sliders allow the use to select the half-reaction's E^o, n or T from which to compute the surface. Other user inputs can include H^+ or OH^- species (with the pH specified) and pure phases (solids or liquids). Figures with superimposed surfaces were generated with the PSI-Plot (Version 9.01) commercial software package (Poly Software International, Pearl River, NY).

References

1. Shaposhnik, V. *J. Anal. Chem.* **2008**, *63*, 199-201.
2. Nernst, W. *Z. Phys. Chem.* **1889**, *4*, 129-181.
3. Peters, R. *Z. Phys. Chem.* **1898**, *26*, 193-236.
4. Rossotti F.; Rossotti H. *The Determination of Stability Constants*; McGraw-Hill: New York, 1961, pp. 39-41.
5. Beck, M. Determination of Stability Constants of Metal Complexes. In *Essays on Analytical Chemistry*; Wanninen, E., ed; Pergamon, New York, 1977, pp 59-79.
6. MaCarthy, P.; Smith, G. Stability Surface Concept. In *Chemical Modeling in Aqueous Systems*; Jenne, E. ed;ACS Symposium Series 93; American Chemical Society: Washington, DC, 1979, pp 201-222.
7. MacCarthy, P. *J. Chem Educ* **1986**, *63*, 339-343.
8. Harris, D. *Quantitative Chemical Analysis. 8th Edition*; Freeman: New York, 2010, pp AP20-AP27
9. J. Kielland *J. Am. Chem. Soc.* **1937**, *59*, 1675-1678.
10. Shaposhnik, V. *J. Anal. Chem.* **2008**, *63*, 199-201.
11. Nernst, W. *Z. Phys. Chem.* **1889**, *4*, 129-181.
12. Peters, R. *Z. Phys. Chem.* **1898**, *26*, 193-236.
13. Rossotti F.; Rossotti H. *The Determination of Stability Constants*; McGraw-Hill: New York, 1961, pp. 39-41.

14. Beck, M. Determination of Stability Constants of Metal Complexes. In *Essays on Analytical Chemistry*; Wanninen, E., ed; Pergamon, New York, 1977, pp 59-79.
15. MaCarthy, P.; Smith, G. Stability Surface Concept. In *Chemical Modeling in Aqueous Systems*; Jenne, E. ed;ACS Symposium Series 93; American Chemical Society: Washington, DC, 1979, pp 201-222.
16. MacCarthy, P. *J. Chem Educ* **1986**, *63*, 339-343.
17. Harris, D. *Quantitative Chemical Analysis. 8th Edition*; Freeman: New York, 2010, pp AP20-AP27
18. J. Kielland *J. Am. Chem. Soc.* **1937**, *59*, 1675-1678.

Chapter 8

3-D Surface visualization of aqueous solubility of sparingly soluble salts

8.1 Solubility of Ionic Salts

The solubility product expression, $K_{sp,}$ was first introduced by Walther Nernst in 1889[1]. When the solubility phenomenon of slightly soluble salts is introduced in general chemistry courses, it is traditionally it taught from the standpoint of simple K_{sp} expression[2]. This is an inadequate description of the rich chemistry that can occur in solution. Ion pairing, dissolved aqueous complexes, hydrolysis reactions, and polynuclear species are all possibilities (Figure 8.1). 3-D visualization of solubility topo surfaces above a cation-anion composition grid can systematically address each of these complicating side-reactions and reveals the conditions under which they become significant. This chapter only includes detailed topo surfaces and analysis for the simplest K_{sp}-only case due to time constraints. It does, however, set the framework for future developments in which the more complicated interactions can be compared to the limitations of the K_{sp}-only model.

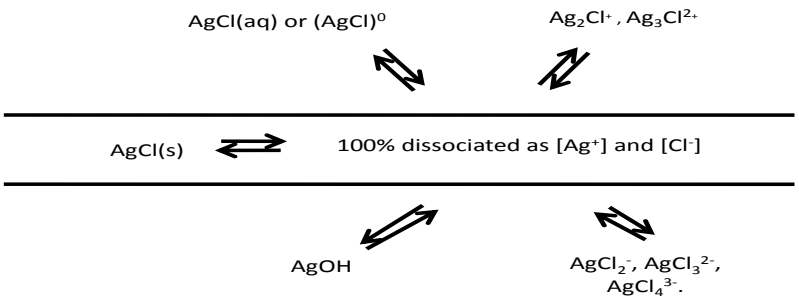

Figure 8.1. Some possible interactions in the AgCl system.

The composition grid for solubility topo surfaces shows the total analytical concentration of the anion on the y-axis and the total analytical concentration of the cation on the x-axis. The principal z-axis for solubility systems will represent the overall solubility of the salt of interest, often in the presence of common ions. Because compositions for the surface include more than just adding a solid ionic salt to water, a broad view of solubility must be kept in mind. The dissolution of AgCl in water corresponds to a limited series of mixtures that define a simple diagonal trace across the composition grid from the upper right corner of the grid to the lower left. The topo treatment here also considers all the off-diagonal combinations of Ag^+ and Cl^- ions that could be formulated. This broader investigation of the AgCl system can be visualized as mixing various combinations of $AgNO_3$ and NaCl solutions to produce one of the two components in excess.

The definition of solubility shifts from one region of the topo surfaces to another to take into account those situations in which common ions are present. Without common ions, i.e., a stoichiometric mix, the solubility of the salt can be determined from either of its component ions. With common ions around, however, their influence on solubility equilibrium must be taken into account. Consider, for example, the simple K_{sp}-only case for AgCl in which only a 1:1 salt exists. Under excess Cl^- conditions, e.g., AgCl is dissolved in NaCl, the solubility will be defined by the $[Ag^+]$ concentration. Under excess Ag conditions, e.g., AgCl is dissolved in $AgNO_3$, it is the $[Cl^-]$ that determines the solubility.

Stoichiometric mix:	solubility = $[Ag^+] = [Cl^-]$	(Eq 8.1)
Excess Ag:	solubility = $[Cl^-]$	(Eq 8.2)

Excess NaCl : solubility = $[Ag^+]$ (Eq 8.3)

8.2 Computational approach for solubility topo surface calculations

The log-log composition grid used for solubility topos contains 1369 grid points (37 x 37) where each axis covers a range from 1 $x10^{-9}$ M to 1 M in 0.25 log unit increments. This permits modeling of a wide range of compositions, essentially most that are feasible. It is essentially the same grid as was used for the metal-ligand complexation grid (see Figure 5.1). A Microsoft Excel™ spreadsheet, Solubility TOPOS has been created with embedded Visual Basic™ macros to automatically compute and plot the solubility topos for many K_{sp}-only systems. They only required inputs are a choice of the salt's stoichiometry and the associated K_{sp} value. The version included here is incomplete in that no aqueous species other than the bare component ions are included.

For illustrative purposes, the AgCl system is chosen as it has numerous applications ranging from photography to the most widely employed reference electrodes. Because it has been extensively studied, there is a large body of available thermodynamic and experimental data. For the simple model presented here, a K_{sp} value of 1.8 x 10^{-10} was adopted[3]. In order to calculate the complete solubility topo surface, six different solubility assignment procedures were employed depending on the region of the composition grid (Figure 8.2). Three regions, 1 through 3, are associated with unsaturated solutions and three others, 4 through 6, correspond to saturated conditions. Separating the two groups of regions is the diagonal saturation boundary that is determined by the K_{sp} value. It intersects both axes at log (1.8 x 10^{-1} M) = -.74. For Regions 1 through 3 no solid AgCl is present. For a stoichiometric mix,

when AgCl is dissolved in pure water, either $Ag_{tot} = [Ag^+]$ or $Cl_{tot} = [Cl^-]$ provides the solubility value. Region 2 contains all compositions where AgCl completely dissolves in a NaCl solution. Since Cl^- can come from two sources, either AgCl or NaCl, we determine the amount of AgCl that has dissolved from $Ag_{tot} = [Ag^+]$. The complementary case occurs over Region 3 as AgCl completely dissolves in a solution of $AgNO_3$. These assignments generate two ramps that are inclined at 45° and meet in a ridge over the Region 1 stoichiometric mix line (Figure 8.3).

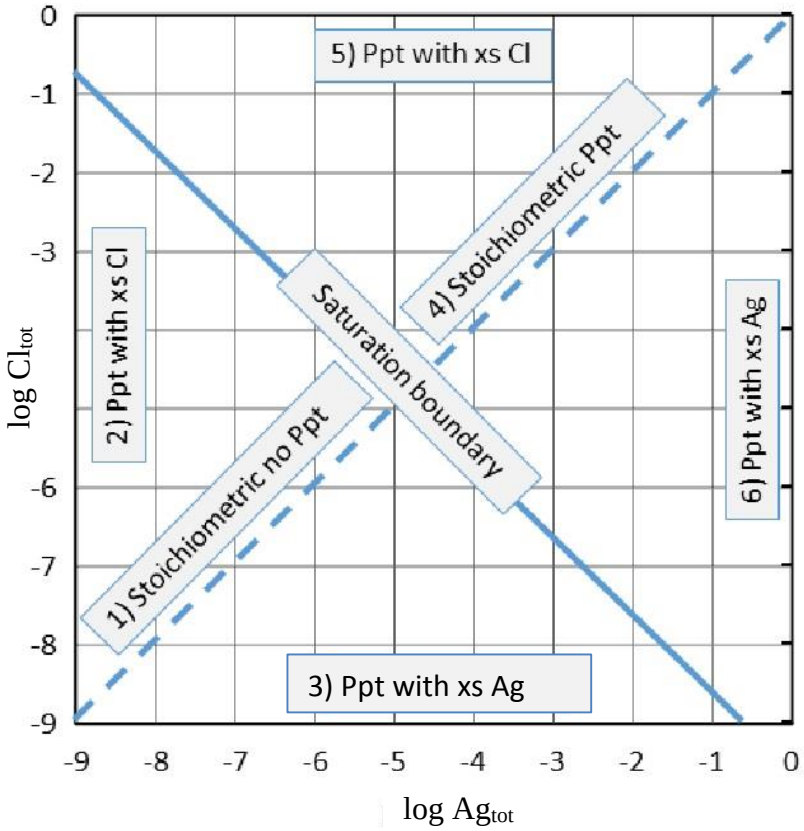

Figure 8.2. Solubility assignment regions for the AgCl system.

Color filled surfaces are presented for the solubility topos because their pyramidal structure is difficult to perceive in an open wire-frame plot. The pyramid faces on the back side from the viewer make too much visual clutter.

In Regions 4 through 6 the solution is saturated with respect to AgCl and solid is present. The solubility of AgCl along the Region 4 stoichiometric mix line uses the familiar solubility = $K_{sp}^{0.5}$ formula for a 1:1 salt[4]. Regions 5 and 6 are complementary. In both cases one begins with the assumption that the free species of interest is equal to its excess amount. This is then successively substituted into the K_{sp} expression and refined until no additional changes are noted within the allowed precision. Because the contributions from the solubility of sparingly soluble salts are small in comparison to the excess levels, not many iterative refinement cycles are needed.

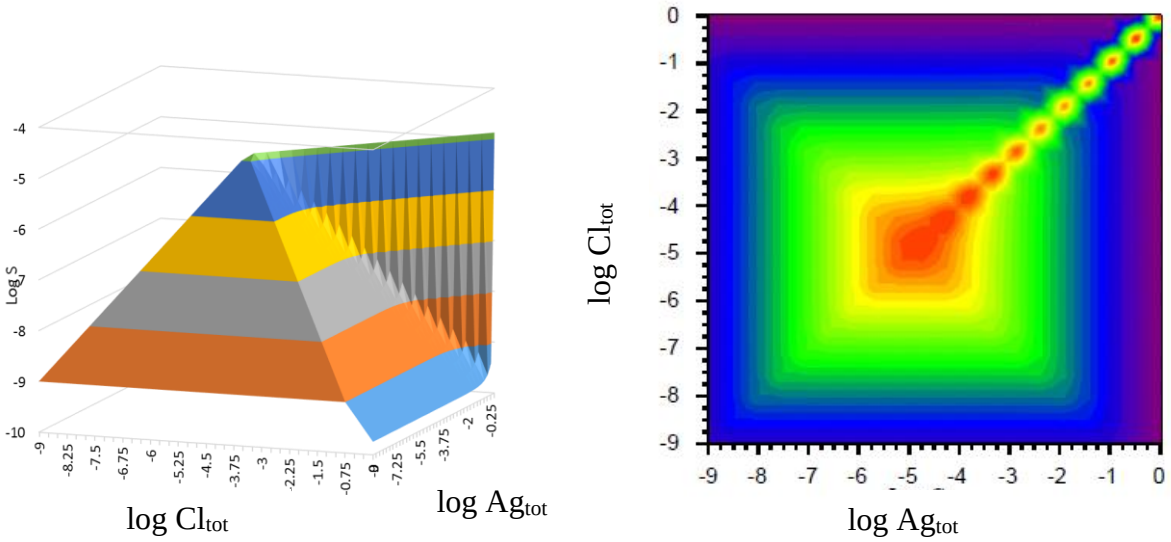

Figure 8.3. Wire frame (left) and contour (right) versions of the AgCl solubility topos for the K_{sp}-only model.

A default value of 8 cycles is built into the program but can be easily altered if necessary. The Region 4 through 6 portions of the 1:1 AgCl surface shows a "stoichiometric spine" running from the middle of the saturation boundary to the (0,0) point at the upper right corner of the grid. The spine is horizontal without any breaks. An artifact of the Excel routines that draw three-dimensional surfaces makes it appear as a series of individual, toothy peaks. Finer grid point increments would confirm its smooth horizontal character. To

either side are sloping ramps that complete an overall pyramid shape elsewhere.

8.3 Surfaces for other stoichiometries

Sparingly soluble salts with stoichiometries beyond a 1:1 ratio show similar solubility topos. Figure 8.4, for example, illustrates the solubility topo surface for lead (II) iodide, PbI_2 with a K_{sp} of 7.9×10^{-9}. While the overall surface still has a pyramidal shape, it is not symmetric. The two faces visible in the wire-frame view below are tipped toward the high point at an incline of 45°. The face for excess ligand in the saturated regions is tipped more steeply at 60°. That is why the colored contours are less wide in the right-hand figure panel. The face for excess metal in the saturated regions is more shallowly sloped at 30°.

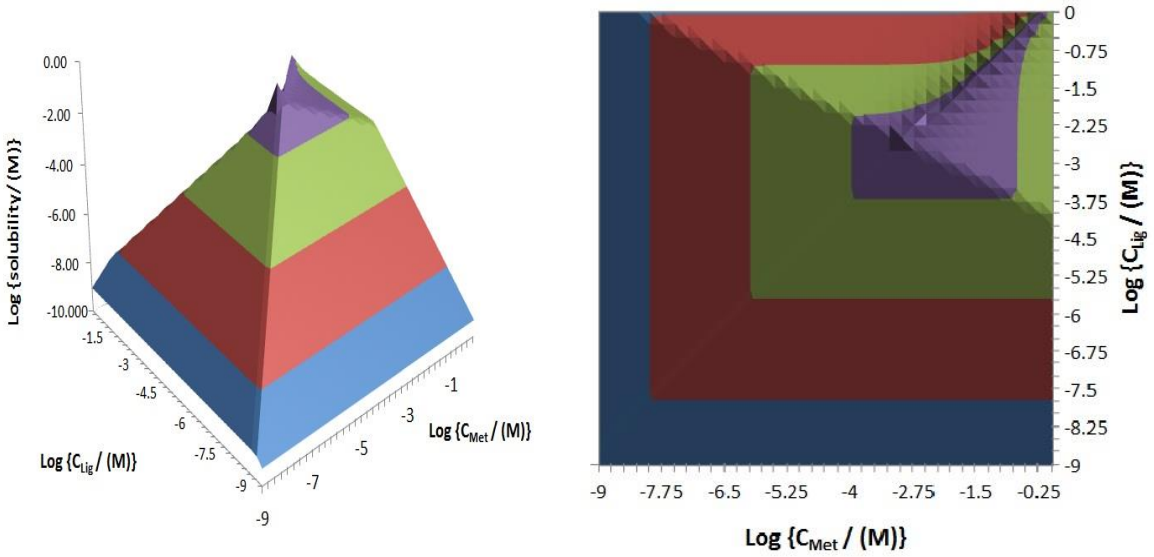

Figure 8.4. Colored wire frame and contour map solubility topos for PbI_2

A complication in visualizing the surfaces is encountered for the 1:2 stoichiometry because the regular-spaced grid points do not coincide with the

stoichiometric spine (Figure 8.5). At the left edge of the grid, when the Pb_{tot} = $[Pb^{2+}]$ is 10^{-9} M, the $I_{tot} = [I^-]$ is 2 x 10^{-9} M. Grid points are at log I_{tot} values of -9.0, -8.75, 8.50. Log (2 x 10^{-9}) = -8.70 is not at a grid point. Thus, the stoichiometric ridge has anomalies caused by landing on non-grid points across the entire grid. The ridge edge should be sharp in the unsaturated region. Here it is shaved off into a thin flat strip. The small peak at the top of the pyramid, where the saturation boundary intersects the stoichiometric ratio, is an artifact. In reality, once the saturation boundary is encountered, the solubility is a fixed constant for the remainder of the spine's run.

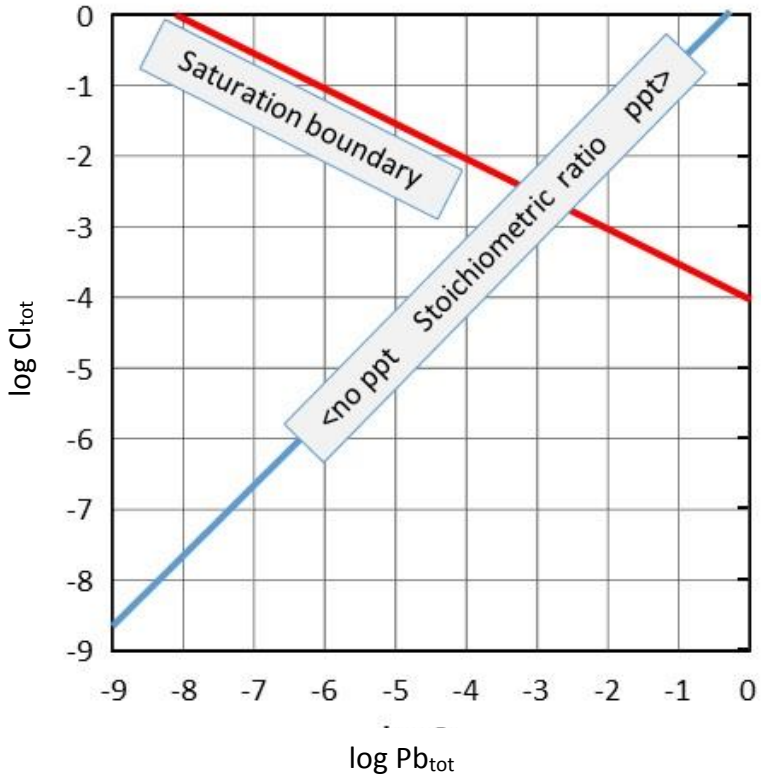

Figure 8.5. The stoichiometric ratio path for a 1:2 salt on the solubility composition grid. While the path crosses the grid at a 45° angle, it misses grid points at every occasion.

8.4 Developments beyond the K_{sp}-only model

The shortcomings of a simple K_{sp} interpretation of the aqueous chemistry of AgCl can be highlighted by including model situations in which ion pairing/neutral complexes, higher chloro-complexes, hydroxyl complexes and binuclear species are present. Unfortunately, time constraints do not allow a detailed treatment here. But the framework has been established with the solubility composition grid around which to organize an analysis of where additional chemical interactions would come into play. Increasingly complete model scenarios can be systematized into the following cases:

Case 1: The simplistic K_{sp}-only model where dissolved species are just Ag^+ and Cl^-

Case 2: Inclusion of a neutral complex/ion pair $AgCl^0$

Case 3: Inclusion of higher, negatively charged, chloro-complexes and silver hydroxyl hydrolytic species - $AgCl_2^-$, $AgCl_3^{2-}$, $AgCl_4^{3-}$, AgOH, $Ag(OH)_2^-$, etc.

Case 4: Inclusion of polynuclear complex, Ag_2Cl_2.

The goal of visualizing these new 3-D topo surfaces would be to highlight the importance of having increasingly detailed descriptions of the chemistry occurring in aqueous solubility systems. Presenting these surfaces with a wide range of compositions will provide the knowledge to know under what conditions the various discrepancies are encountered. The expansion of the Solubility TOPOS program to include these higher cases is in progress and should make it no longer necessary to neglect other important reactions going on in the system. Even beginning students could evaluate the impact of omitting various species from the model.

The solubility of AgCl in the higher cases will include aqueous species beyond [Ag^+]. Chloro- and hydroxyl-complexes will enhance the calculated solubility. For example, the solubility of AgCl in a saturated region with excess Cl^- would be;

$$solubility = [Ag^+] + [AgCl^0] + [AgCl_2^-] + [AgCl_3^{2-}] + [AgCl_4^{3-}] + [AgOH^0] + \cdots \quad \text{(Eq 8.4)}$$

References:

1. Butler, J. N. Ionic equilibrium: Solubility and pH Calculations, 1st ed., John Willey & Sons, Inc., New York, NY, 1998.
2. Clark, R.W.; Bonicamp, J.M. The Ksp- Solubility Conundrum. J. Chem. 75(9), 1998, 1182-1185.
3. Fritz, J. J., Journal of solution chemistry 1985, 14, 865-879.
4. Harris, D. Quantitative Chemical Analysis, 8 ed., W. H. Freeman, New York, NY, 2011.

Chapter 9
Conclusions and Future Directions

9.1 Conclusions

This thesis has examined aqueous equilibrium chemistry through 3-D visualizations of acid-base reactions, metal-ligand complexation reactions, redox reactions and the solubility of ionic salts. The studies established a series of composition grids above which topos trend surfaces were constructed. Because it includes a wider range of compositions than other traditional approaches, features that were noted on the topos prompted new understanding and new questions about the underlying chemistry. Several previously unreported behaviors emerged in the process. One of them was subsequently confirmed through laboratory experiments. In each case, Microsoft Excel™ worksheets were developed with underlying Visual Basic™ macros that easily compute and plot the resulting topo surfaces.

Each subsection below holds bullet points that highlight the new insights that were gained as a result of using the composition grid topos approach.

9.1.1 Acid-base topos

Visualization of buffering against dilution.

Visualization of the limits of the Henderson-Hasselbalch equation

Visualization of conditions under which weak acids and strong acids become indistinguishable

Visualization of the difference between buffering and pseudobuffering

Visualization of the relationship between a titration curve and its corresponding buffer capacity.

Visualizations that emphasize where buffer capacity minima are encountered

Visualization of the equal buffer capacities for polyprotic acids

9.1.2 Metal-ligand topos

Visualization of metal anti-buffering and the conditions required for its observation

Visualization of metal buffering and the conditions required for its maintenance

9.1.3 Redox topos

Visualization of E^o constant character over most conditions

Visualization of galvanic and concentration cells

Visualization of battery life failure, i.e., galvanic cells reaching equilibrium

Visualization of the impacts of other Nernst equation parameters

9.1.4 Solubility topos

Visualization of solubility impacts from common ions vs. pure salt

Visualization framework for more complex interactions in a system

9.2 Future directions

A thorough understanding and appreciation of aqueous equilibrium reactions is important to many fields of study yet there has been a lack of modern software that can easily model complex equilibrium calculations. The Journal of Chemical Education used to have packages that were widely distributed and available for minimal costs. Unfortunately, these have died out and now only exist in obsolete operating system languages. The TOPOS software that originated with this dissertation can help replace these lost teaching resources.

Because they are embedded with Microsoft Excel™, they will be usable on essentially any computer. The program use has a minimal learning curve. It is extremely user friendly in that the only inputs needed to run the programs are entry of thermodynamic constants into designated, color-coded cells. The Journal of Chemical Education appears interested in having the TOPOS software included in a series of papers that as Supplemental Information also include teaching resources for their incorporation into lectures (as PowerPoint™ files) and laboratory exercises.

Not only will the TOPOS programs make is quick and easy for anyone to simulate common laboratory procedures, they will also begin to expose them to the composition grid approach to looking at overall system trends. The envisioned comprehensive future package will allow the user to see the variety of common experimental paths that are contained in a single surface. This will help show the inter-relationships between procedures that might not otherwise be realized. Understanding the wider behavior of equilibrium systems makes it easier to predict the possible behaviors to expect without doing individual calculations.

Improvements for future versions of the TOPOS programs will be:

Acid-base/buffer capacity – incorporation of addition of bases into strong acid titrations, mixtures of acids or/and bases, weak acid into weak base scenarios, species distribution topos, degree of dissociation topos, etc.

Metal-ligand – addition of a wider range of possible complexes and hydrolytic species, complexometric titrations, multi-metal and multi-

ligand systems, incorporation of precipitation or redox processes involved.

Redox – visualization of redox buffers, redox titrations

Solubility – completion of more comprehensive models with complexation, hydrolytic species, polynuclear complexes; gravimetric titrations, separation by precipitation.

Appendix I

Derivation of Exact Equations for Buffer Capacity

I.A An Equation to Correlate Buffer Capacity with V_b and Dilution for a Strong Acid (HCl) Titrated with a Strong Base (NaOH)

A detailed treatment of the system (ignoring activity effects for ease in reading) includes four equations involving four dissolved species: $[H_3O^+]$, $[OH^-]$, $[Na^+]$, and $[Cl^-]$. Other symbols used in this derivation are: V_a and V_b for the volumes of acid and base that have been added to the system at any point; C_a^0 and C_b^0 for the concentrations of the acid and base stock solutions; and y for the dilution factor associated with a specific titration run.

Auto-ionization of water:

$$K_w = [H_3O^+][OH^-] = 1.0 \times 10^{-14} \quad \text{(I.1)}$$

Mass balance on sodium ion (a conserved species):

$$\left[Na^+\right] = \frac{V_b y C_b^{\,0}}{V_a + V_b} \quad \text{(I.2)}$$

Mass balance on chloride ion (another conserved species):

$$\left[Cl^-\right] = \frac{V_a y C_a^{\,0}}{V_a + V_b} \quad \text{(I.3)}$$

Charge balance:

$$[H_3O^+] + [Na^+] = [OH^-] + [Cl^-] \quad \text{(I.4)}$$

Our goal is to solve the set of four equations for V_b as a function of $[H_3O^+]$ so that the exact buffer capacity for each point during a titration can be calculated. This is most easily done by substituting Equations I.1, I.2 and I.3 into the charge balance equation.

$$\left[H_3O^+\right] + \frac{V_b y C_b^{\,0}}{V_a + V_b} = \frac{K_w}{\left[H_3O^+\right]} + \frac{V_a y C_a^{\,0}}{V_a + V_b} \tag{I.5}$$

Algebraic manipulation to isolate V_b involves the following steps:

Multiply both sides by the total volume, $(V_a + V_b)$

$$\left(V_a + V_b\right)\left[H_3O^+\right] + V_b y C_b^{\,0} = \left(V_a + V_b\right)\frac{K_w}{\left[H_3O^+\right]} + V_a y C_a^{\,0} \tag{I.6}$$

Distribute the volume terms to separate V_b and V_a terms:

$$V_a\left[H_3O^+\right] + V_b\left[H_3O^+\right] + V_b y C_b^{\,0} = V_a\frac{K_w}{\left[H_3O^+\right]} + V_b\frac{K_w}{\left[H_3O^+\right]} + V_a y C_a^{\,0} \tag{I.7}$$

Collect all V_b terms on the left:

$$V_b\left[H_3O^+\right] + V_b y C_b^{\,0} - V_b\frac{K_w}{\left[H_3O^+\right]} = V_a\frac{K_w}{\left[H_3O^+\right]} + V_a y C_a^{\,0} - V_a\left[H_3O^+\right] \tag{I.8}$$

Factor out V_b and V_a:

$$V_b\left(\left[H_3O^+\right] + y C_b^{\,0} - \frac{K_w}{\left[H_3O^+\right]}\right) = V_a\left(\frac{K_w}{\left[H_3O^+\right]} + y C_a^{\,0} - \left[H_3O^+\right]\right) \tag{I.9}$$

Isolate V_b:

$$V_b = V_a\frac{\left(\frac{K_w}{\left[H_3O^+\right]} + y C_a^{\,0} - \left[H_3O^+\right]\right)}{\left(\left[H_3O^+\right] + y C_b^{\,0} - \frac{K_w}{\left[H_3O^+\right]}\right)} \tag{I.10}$$

This expression is now differentiated with respect to $[H_3O^+]$ using the chain rule for a quotient of functions.

$$\frac{\partial V_b}{\partial\left[H_3O^+\right]} = V_a\left(\left(\frac{1}{\left[H_3O^+\right] + yC_b{}^0 - \frac{K_w}{\left[H_3O^+\right]}}\right)\left(\frac{-K_w}{\left[H_3O^+\right]^2} - 1\right) - \frac{\left(\frac{K_w}{\left[H_3O^+\right]} + yC_a{}^0 - \left[H_3O^+\right]\right)}{\left(\left[H_3O^+\right] + yC_b{}^0 - \frac{K_w}{\left[H_3O^+\right]}\right)^2}\left(1 + \frac{K_w}{\left[H_3O^+\right]^2}\right)\right) \tag{I.11}$$

Since buffer capacity values relate to pH rather than $[H_3O^+]$, the relationships

$$pH = -\frac{1}{2.303}\ln\left[H_3O^+\right] \tag{I.12}$$

and

$$\frac{d\,[H_3O^+]}{d\ pH} = -2.303[H_3O^+] \tag{I.13}$$

are required to express the derivative in terms of pH:

$$\frac{\partial V_b}{\partial\ pH} = -2.303[H_3O^+]V_a\left(\left(\frac{1}{\left[H_3O^+\right] + yC_b{}^0 - \frac{K_w}{\left[H_3O^+\right]}}\right)\left(\frac{-K_w}{\left[H_3O^+\right]^2} - 1\right) - \frac{\left(\frac{K_w}{\left[H_3O^+\right]} + yC_a{}^0 - \left[H_3O^+\right]\right)}{\left(\left[H_3O^+\right] + yC_b{}^0 - \frac{K_w}{\left[H_3O^+\right]}\right)^2}\left(1 + \frac{K_w}{\left[H_3O^+\right]^2}\right)\right) \tag{I.14}$$

Finally, to express the buffer capacity, β, we need to convert the numerator to moles of base by multiplying the volume times the diluted concentration:

$$\beta = \frac{yC_b^{\,0}\partial V_b}{\partial\,pH} = -yC_b^{\,0}\,2.303[H_3O^+]V_a\left(\left(\frac{1}{[H_3O^+] + yC_b^{\,0} - \frac{K_w}{[H_3O^+]}}\right)\left(\frac{-K_w}{[H_3O^+]^2} - 1\right) - \frac{\left(\frac{K_w}{[H_3O^+]} + yC_a^{\,0} - [H_3O^+]\right)}{\left([H_3O^+] + yC_b^{\,0} - \frac{K_w}{[H_3O^+]}\right)^2}\left(1 + \frac{K_w}{[H_3O^+]^2}\right)\right)$$

(I.15)

Note: If V_a is not 1 L, an added term must be applied to the final form that scales it to 1 L. For example, if V_a is taken as 100.0 mL in a specific run, the final equation would be

$$\beta = \frac{10yC_b^{\,0}\partial V_b}{\partial\,pH} = -10yC_b^{\,0}\,2.303[H_3O^+]V_a\left(\left(\frac{1}{[H_3O^+] + yC_b^{\,0} - \frac{K_w}{[H_3O^+]}}\right)\left(\frac{-K_w}{[H_3O^+]^2} - 1\right) - \frac{\left(\frac{K_w}{[H_3O^+]} + yC_a^{\,0} - [H_3O^+]\right)}{\left([H_3O^+] + yC_b^{\,0} - \frac{K_w}{[H_3O^+]}\right)^2}\left(1 + \frac{K_w}{[H_3O^+]^2}\right)\right)$$

(I.16)

Derivation of the Exact Buffer Capacity vs. V_b Equation for a Weak Monoprotic Acid (HA) Titrated with a Strong Base (NaOH)

A detailed treatment of the system (ignoring activity effects for ease in reading) includes five equations involving five dissolved species: $[H_3O^+]$, $[OH^-]$, $[Na^+]$, [HA], and $[A^-]$. Other symbols used in this derivation are: V_a and V_b for the volumes of acid and base that have been added to the system at any point; C_a^0 and C_b^0 for the concentrations of the acid and base stock solutions; and y for the dilution factor associated with a specific titration run.

Auto-ionization of water:

$$K_w = [H_3O^+][OH^-] = 1.0 \times 10^{-14} \qquad \text{(I.1)}$$

Mass balance on sodium ion (a conserved species):

$$\left[Na^+\right] = \frac{V_b y C_b^{\,0}}{V_a + V_b} \qquad \text{(I.2)}$$

The acid dissociation constant of the weak acid

$$K_a = \frac{\left[H_3O^+\right]\left[A^-\right]}{\left[HA\right]} \qquad \text{(I.16)}$$

And a mass balance on the weak acid:

$$\frac{V_a y C_a^{\,0}}{V_a + V_b} = \left[HA\right] + \left[A^-\right] \qquad \text{(I.17)}$$

Charge balance:

$$[H_3O^+] + [Na^+] = [OH^-] + [A^-] \qquad \text{(I.18)}$$

Our goal is to solve the set of five equations for V_b as a function of $[H_3O^+]$ so that the exact buffer capacity for each point during a titration can be calculated. This is most easily done by combining Equations I.18 and I.19 into an expression for $[A^-$

] and substituting that result along with equations I.1 and I.2 into the charge balance (Equation I.18).

Equations I.16 and I.17 combine to give the well-known acid species distribution relationship:

$$\left[A^-\right] = \alpha_1 \frac{V_a y C_a{}^0}{(V_a + V_b)} = \left(\frac{K_a}{[H_3O^+] + K_a}\right)\left(\frac{V_a y C_a{}^0}{(V_a + V_b)}\right) \tag{I.19}$$

The substituted charge balance equation now appears as:

$$\left[H_3O^+\right] + \frac{V_b y C_b}{V_a + V_b} = \frac{K_w}{\left[H_3O^+\right]} + \alpha_1\left(\frac{V_a y C_a}{(V_a + V_b)}\right) \tag{I.20}$$

Algebraic manipulation to isolate V_b involves the following steps:

Multiply both sides by the total volume, $(V_a + V_b)$

$$(V_a + V_b)\left[H_3O^+\right] + V_b y C_b{}^0 = (V_a + V_b)\frac{K_w}{\left[H_3O^+\right]} + \alpha_1 V_a y C_a{}^0 \tag{I.21}$$

Distribute the volume terms to separate V_b and V_a terms:

$$V_a\left[H_3O^+\right] + V_b\left[H_3O^+\right] + V_b y C_b{}^0 = V_a\frac{K_w}{\left[H_3O^+\right]} + V_b\frac{K_w}{\left[H_3O^+\right]} + \alpha_1 V_a y C_a{}^0 \tag{I.22}$$

Collect all V_b terms on the left:

$$V_b\left[H_3O^+\right] + V_b y C_b{}^0 - V_b\frac{K_w}{\left[H_3O^+\right]} = V_a\frac{K_w}{\left[H_3O^+\right]} + \alpha_1 V_a y C_a{}^0 - V_a\left[H_3O^+\right] \tag{I.23}$$

Factor out V_b and V_a:

$$V_b\left(\left[H_3O^+\right]+yC_b{}^0-\frac{K_w}{\left[H_3O^+\right]}\right)=V_a\left(\frac{K_w}{\left[H_3O^+\right]}+\alpha_1 yC_a{}^0-\left[H_3O^+\right]\right) \tag{I.24}$$

Isolate V_b:

$$V_b=V_a\frac{\left(\frac{K_w}{\left[H_3O^+\right]}+\alpha_1 yC_a{}^0-\left[H_3O^+\right]\right)}{\left(\left[H_3O^+\right]+yC_b{}^0-\frac{K_w}{\left[H_3O^+\right]}\right)} \tag{I.25}$$

$$=V_a\frac{\left(\frac{K_w}{\left[H_3O^+\right]}+\left(\frac{K_a}{[H_3O^+]+K_a}\right)yC_a{}^0-\left[H_3O^+\right]\right)}{\left(\left[H_3O^+\right]+yC_b{}^0-\frac{K_w}{\left[H_3O^+\right]}\right)}$$

Note that this expression for V_b is identical to that for the strong acid/strong base case (Equation I.10) except for the coefficient of the middle term in the numerator on the right-hand side.

This expression is now differentiated with respect to $[H_3O^+]$ using the chain rule for a quotient of functions. (Note it is necessary to replace α_1 with its complete expression before differentiating because the complete α_1 expression has terms that include $[H_3O^+]$, the variable of differentiation.)

$$\frac{\partial V_b}{\partial\left[H_3O^+\right]}=V_a\left(\begin{array}{l}\left(\frac{1}{\left[H_3O^+\right]+yC_b{}^0-\frac{K_w}{\left[H_3O^+\right]}}\right)\left\{\frac{-K_w}{\left[H_3O^+\right]^2}+K_a yC_a{}^0\left(\frac{-1}{\left(\left[H_3O^+\right]+K_a\right)^2}\right)-1\right\}\\ \quad-\frac{\left(\frac{K_w}{\left[H_3O^+\right]}+\left(\frac{K_a}{[H_3O^+]+K_a}\right)yC_a{}^0-\left[H_3O^+\right]\right)}{\left(\left[H_3O^+\right]+yC_b{}^0-\frac{K_w}{\left[H_3O^+\right]}\right)^2}\left(1+\frac{K_w}{\left[H_3O^+\right]^2}\right)\end{array}\right) \tag{I.26}$$

Since buffer capacity values relate to pH rather than $[H_3O^+]$, the relationships

$$\mathrm{pH} = -\frac{1}{2.303}\ln\left[\mathrm{H_3O^+}\right] \tag{I.12}$$

and

$$\frac{d\,[\mathrm{H_3O^+}]}{d\ \mathrm{pH}} = -2.303[\mathrm{H_3O^+}] \tag{I.13}$$

are again used to express the derivative in terms of pH:

$$\frac{\partial \mathrm{V_b}}{\partial\ \mathrm{pH}} = -2.303[\mathrm{H_3O^+}]\mathrm{V_a}\left(\left(\frac{1}{\left[\mathrm{H_3O^+}\right] + \mathrm{yC_b}^{0} - \frac{\mathrm{K_w}}{\left[\mathrm{H_3O^+}\right]}}\right)\left\{\frac{-\mathrm{K_w}}{\left[\mathrm{H_3O^+}\right]^2} + \mathrm{K_a yC_a}^{0}\left(\frac{-1}{\left(\left[\mathrm{H_3O^+}\right] + \mathrm{K_a}\right)^2}\right) - 1\right\} - \frac{\left(\frac{\mathrm{K_w}}{\left[\mathrm{H_3O^+}\right]} + \left(\frac{\mathrm{K_a}}{[\mathrm{H_3O^+}] + \mathrm{K_a}}\right)\mathrm{yC_a}^{0} - \left[\mathrm{H_3O^+}\right]\right)}{\left(\left[\mathrm{H_3O^+}\right] + \mathrm{yC_b}^{0} - \frac{\mathrm{K_w}}{\left[\mathrm{H_3O^+}\right]}\right)^2}\left(1 + \frac{\mathrm{K_w}}{\left[\mathrm{H_3O^+}\right]^2}\right)\right) \tag{I.27}$$

Finally, to express the buffer capacity, β, we need to convert the numerator to moles of base by multiplying the volume times the diluted concentration and correcting to 1 L by multiplying by 10:

$$\beta = \frac{\mathrm{yC_b}^{0}\partial \mathrm{V_b}}{\partial\ \mathrm{pH}} = -10\mathrm{yC_b}2.303[\mathrm{H_3O^+}]\mathrm{V_a}\left(\left(\frac{1}{\left[\mathrm{H_3O^+}\right] + \mathrm{yC_b}^{0} - \frac{\mathrm{K_w}}{\left[\mathrm{H_3O^+}\right]}}\right)\left\{\frac{-\mathrm{K_w}}{\left[\mathrm{H_3O^+}\right]^2} + \mathrm{K_a yC_a}^{0}\left(\frac{-1}{\left(\left[\mathrm{H_3O^+}\right] + \mathrm{K_a}\right)^2}\right) - 1\right\} - \frac{\left(\frac{\mathrm{K_w}}{\left[\mathrm{H_3O^+}\right]} + \left(\frac{\mathrm{K_a}}{[\mathrm{H_3O^+}] + \mathrm{K_a}}\right)\mathrm{yC_a}^{0} - \left[\mathrm{H_3O^+}\right]\right)}{\left(\left[\mathrm{H_3O^+}\right] + \mathrm{yC_b}^{0} - \frac{\mathrm{K_w}}{\left[\mathrm{H_3O^+}\right]}\right)^2}\left(1 + \frac{\mathrm{K_w}}{\left[\mathrm{H_3O^+}\right]^2}\right)\right) \tag{I.28}$$

Derivation of the Exact Buffer Capacity vs. V_b Equation for a Weak Diprotic Acid (H_2A) Titrated with a Strong Base (NaOH)

A detailed treatment of the system (ignoring activity effects for ease in reading) includes six equations involving six dissolved species: $[H_3O^+]$, $[OH^-]$, $[Na^+]$, $[H_2A]$, $[HA^-]$, and $[A^{2-}]$. Other symbols used in this derivation are: V_a and V_b for the volumes of acid and base that have been added to the system at any point; C_a^0 and C_b^0 for the concentrations of the acid and base stock solutions; and y for the dilution factor associated with a specific titration run.

Auto-ionization of water:

$$K_W = [H_3O^+][OH^-] = 1.0 \times 10^{-14} \qquad \text{(I.1)}$$

Mass balance on sodium ion (a conserved species):

$$\left[Na^+\right] = \frac{V_b y C_b^{\,0}}{V_a + V_b} \qquad \text{(I.2)}$$

The first acid dissociation constant of the weak acid

$$K_{a1} = \frac{\left[H_3O^+\right]\left[HA^-\right]}{\left[H_2A\right]} \qquad \text{(I.29)}$$

The second acid dissociation constant of the weak acid

$$K_{a2} = \frac{\left[H_3O^+\right]\left[A^{2-}\right]}{\left[HA^-\right]} \qquad \text{(I.30)}$$

A mass balance on the weak acid:

$$\frac{V_a y C_a^{\,0}}{V_a + V_b} = \left[H_2A\right] + \left[HA^-\right] + \left[A^{2-}\right] \qquad \text{(I.31)}$$

And the charge balance:

$$[H_3O^+] + [Na^+] = [OH^-] + [HA^-] + 2\,[A^{2-}] \qquad \text{(I.32)}$$

Our goal is to solve the set of six equations for V_b as a function of $[H_3O^+]$ so that the exact buffer capacity for each point during a titration can be calculated. This is most easily done by substituting into the charge balance expression (Equation I.32) equivalent values for $[Na^+]$, $[OH^-]$, $[HA^-]$ and $[A^{2-}]$ written exclusively in terms of $[H_3O^+]$ and constant values.

Equations I.29, I. 30 and I.31 combine to give the well-known acid species distribution relationships for $[HA^-]$ and $[A^{2-}]$ in terms of $[H_3O^+]$, K_{a1} and K_{a2}:

$$\left[HA^-\right] = \alpha_1 \frac{V_a y C_a{}^0}{(V_a + V_b)} = \left(\frac{K_{a1}[H_3O^+]}{[H_3O^+]^2 + K_{a1}[H_3O^+] + K_{a1}K_{a2}}\right)\left(\frac{V_a y C_a{}^0}{(V_a + V_b)}\right) \tag{I.33}$$

$$\left[A^{2-}\right] = \alpha_2 \frac{V_a y C_a{}^0}{(V_a + V_b)} = \left(\frac{K_{a1}K_{a2}}{[H_3O^+]^2 + K_{a1}[H_3O^+] + K_{a1}K_{a2}}\right)\left(\frac{V_a y C_a{}^0}{(V_a + V_b)}\right) \tag{I.34}$$

The charge balance equation (Equation I.36) can now be fully substituted. Equation I.2 is used for $[Na^+]$, Equation I.1 is rearranged to express $[OH^-]$ as $K_w/[H_3O^+]$, and Equations I.33 andI. 34 are used for the two charged forms of the acid. The substituted charge balance equation now appears as:

$$\begin{aligned}\left[H_3O^+\right] + \frac{V_b y C_b{}^0}{V_a + V_b} &= \frac{K_w}{\left[H_3O^+\right]} + \alpha_1\left(\frac{V_a y C_a{}^0}{(V_a + V_b)}\right) + 2\alpha_2\left(\frac{V_a y C_a{}^0}{(V_a + V_b)}\right) \\ &= \frac{K_w}{\left[H_3O^+\right]} + (\alpha_1 + 2\alpha_2)\left(\frac{V_a y C_a{}^0}{(V_a + V_b)}\right)\end{aligned} \tag{I.35}$$

Algebraic manipulation to isolate V_b involves the same steps as previously described:

Multiply both sides by the total volume, $(V_a + V_b)$

$$\left[H_3O^+\right](V_a + V_b) + V_b y C_b^{\,0} = \frac{K_w(V_a + V_b)}{\left[H_3O^+\right]} + (\alpha_1 + 2\alpha_2) V_a y C_a^{\,0} \tag{I.36}$$

Distribute the volume terms to separate V_b and V_a terms:

$$V_a\left[H_3O^+\right] + V_b\left[H_3O^+\right] + V_b y C_b^{\,0} = V_a \frac{K_w}{\left[H_3O^+\right]} + V_b \frac{K_w}{\left[H_3O^+\right]} + (\alpha_1 + 2\alpha_2) V_a y C_a^{\,0} \tag{I.37}$$

Collect all V_b terms on the left:

$$V_b\left[H_3O^+\right] + V_b y C_b^{\,0} - V_b \frac{K_w}{\left[H_3O^+\right]} = V_a \frac{K_w}{\left[H_3O^+\right]} + (\alpha_1 + 2\alpha_2) V_a y C_a^{\,0} - V_a\left[H_3O^+\right] \tag{I.38}$$

Factor out V_b and V_a:

$$V_b\left(\left[H_3O^+\right] + y C_b^{\,0} - \frac{K_w}{\left[H_3O^+\right]}\right) = V_a\left(\frac{K_w}{\left[H_3O^+\right]} + (\alpha_1 + 2\alpha_2) y C_a^{\,0} - \left[H_3O^+\right]\right) \tag{I.39}$$

Isolate V_b:

$$V_b = V_a \frac{\left(\frac{K_w}{\left[H_3O^+\right]} + (\alpha_1 + 2\alpha_2) y C_a^{\,0} - \left[H_3O^+\right]\right)}{\left(\left[H_3O^+\right] + y C_b^{\,0} - \frac{K_w}{\left[H_3O^+\right]}\right)} \tag{I.40}$$

$$= V_a \frac{\left(\frac{K_w}{\left[H_3O^+\right]} + \left(\frac{K_{a1}[H_3O^+] + 2K_{a1}K_{a2}}{[H_3O^+]^2 + K_{a1}[H_3O^+] + K_{a1}K_{a2}}\right) y C_a^{\,0} - \left[H_3O^+\right]\right)}{\left(\left[H_3O^+\right] + y C_b^{\,0} - \frac{K_w}{\left[H_3O^+\right]}\right)}$$

Note that this expression for V_b is identical to that for the strong acid/strong base case (Equation I.10) and the monoprotic weak acid (Equation I.25) except for the coefficient of the middle term in the numerator on the right-hand side.

This expression is now differentiated with respect to $[H_3O^+]$ using the chain rule for a quotient of functions. (Note again it is necessary to replace α_1 and α_2 with their complete expressions before differentiating because the complete expressions have terms that include $[H_3O^+]$, the variable of differentiation.)

$$\frac{\partial V_b}{\partial\left[H_3O^+\right]} = V_a\left(\left(\frac{1}{\left[H_3O^+\right] + yC_b^{\,0} - \frac{K_w}{\left[H_3O^+\right]}}\right)\left\{\frac{-K_w}{\left[H_3O^+\right]^2} + yC_a^{\,0}\left[\left(\frac{K_{a1}}{\left[H_3O^+\right]^2 + K_{a1}\left[H_3O^+\right] + K_{a1}K_{a2}}\right) - \frac{K_{a1}[H_3O^+] + 2K_{a1}K_{a2}}{\left(\left[H_3O^+\right]^2 + K_{a1}\left[H_3O^+\right] + K_{a1}K_{a2}\right)^2}\left(2\left[H_3O^+\right] + K_{a1}\right)\right] - 1\right\}\right.$$
$$\left. - \frac{\left(\frac{K_w}{\left[H_3O^+\right]} + yC_a^{\,0}\left(\frac{K_{a1}[H_3O^+] + 2K_{a1}K_{a2}}{\left[H_3O^+\right]^2 + K_{a1}\left[H_3O^+\right] + K_{a1}K_{a2}}\right) - \left[H_3O^+\right]\right)}{\left(\left[H_3O^+\right] + yC_b^{\,0} - \frac{K_w}{\left[H_3O^+\right]}\right)^2}\left(1 + \frac{K_w}{\left[H_3O^+\right]^2}\right)\right) \qquad \text{(I.41)}$$

Since buffer capacity values relate to pH rather than $[H_3O^+]$, the relationships

$$\text{pH} = -\frac{1}{2.303}\ln\left[H_3O^+\right] \qquad \text{(I.12)} \qquad \text{and} \qquad \frac{d\,[H_3O^+]}{d\,\text{pH}} = -2.303[H_3O^+] \qquad \text{(I.13)}$$

are again used to express the derivative in terms of pH:

$$\frac{\partial V_b}{\partial\, pH} = -2.303[H_3O^+]V_a \left(\left(\frac{1}{\left[H_3O^+\right] + yC_b{}^0 - \frac{K_w}{\left[H_3O^+\right]}} \right) \left\{ \frac{-K_w}{\left[H_3O^+\right]^2} + yC_a{}^0 \left[\left(\frac{K_{a1}}{\left[H_3O^+\right]^2 + K_{a1}\left[H_3O^+\right] + K_{a1}K_{a2}} \right) - \frac{K_{a1}[H_3O^+] + 2K_{a1}K_{a2}}{\left(\left[H_3O^+\right]^2 + K_{a1}\left[H_3O^+\right] + K_{a1}K_{a2}\right)^2} \left(2\left[H_3O^+\right] + K_{a1}\right) \right] - 1 \right\} - \frac{\left(\frac{K_w}{\left[H_3O^+\right]} + yC_a{}^0 \left(\frac{K_{a1}[H_3O^+] + 2K_{a1}K_{a2}}{\left[H_3O^+\right]^2 + K_{a1}\left[H_3O^+\right] + K_{a1}K_{a2}} \right) - \left[H_3O^+\right] \right)}{\left(\left[H_3O^+\right] + yC_b{}^0 - \frac{K_w}{\left[H_3O^+\right]} \right)^2} \left(1 + \frac{K_w}{\left[H_3O^+\right]^2} \right) \right) \quad \text{(I.42)}$$

Finally, to express the buffer capacity, β, we need to convert the numerator to moles of base by multiplying the volume times the diluted concentration and correcting to 1 L by multiplying by 10:

$$\beta = -10yC_b^{\,0}\,2.303[H_3O^+]V_a\left(\left(\frac{1}{[H_3O^+]+yC_b^{\,0}-\frac{K_w}{[H_3O^+]}}\right)\left\{\frac{-K_w}{[H_3O^+]^2}+yC_a^{\,0}\left[\left(\frac{K_{a1}}{[H_3O^+]^2+K_{a1}[H_3O^+]+K_{a1}K_{a2}}\right)\right.\right.\right.$$
$$\left.\left.\left.-\frac{K_{a1}[H_3O^+]+2K_{a1}K_{a2}}{\left([H_3O^+]^2+K_{a1}[H_3O^+]+K_{a1}K_{a2}\right)^2}\left(2[H_3O^+]+K_{a1}\right)\right]-1\right\}\right)$$
$$-\frac{\left(\frac{K_w}{[H_3O^+]}+yC_a^{\,0}\left(\frac{K_{a1}[H_3O^+]+2K_{a1}K_{a2}}{[H_3O^+]^2+K_{a1}[H_3O^+]+K_{a1}K_{a2}}\right)-[H_3O^+]\right)}{\left([H_3O^+]+yC_b^{\,0}-\frac{K_w}{[H_3O^+]}\right)^2}\left(1+\frac{K_w}{[H_3O^+]^2}\right)\Bigg)$$

(I.43)

Derivation of the Exact Buffer Capacity vs. V_b Equation for a Weak Triprotic Acid (H_3A) Titrated with a Strong Base (NaOH)

A detailed treatment of the system (ignoring activity effects for ease in reading) includes seven equations involving seven dissolved species: $[H_3O^+]$, $[OH^-]$, $[Na^+]$, $[H_2A]$, $[HA^-]$, and $[A^{2-}]$. Other symbols used in this derivation are: V_a and V_b for the volumes of acid and base that have been added to the system at any point; C_a and C_b for the concentrations of the acid and base stock solutions; and y for the dilution factor associated with a specific titration run.

Auto-ionization of water:

$$K_W = [H_3O^+][OH^-] = 1.0 \times 10^{-14} \qquad \text{(I.1)}$$

Mass balance on sodium ion (a conserved species):

$$\left[Na^+\right] = \frac{V_b y C_b^{\,0}}{V_a + V_b} \qquad \text{(I.2)}$$

The first acid dissociation constant of the weak acid

$$K_{a1} = \frac{\left[H_3O^+\right]\left[H_2A^-\right]}{\left[H_3A\right]} \qquad \text{(I.44)}$$

The second acid dissociation constant of the weak acid

$$K_{a2} = \frac{\left[H_3O^+\right]\left[HA^{2-}\right]}{\left[H_2A^-\right]} \qquad \text{(I.45)}$$

The third acid dissociation constant of the weak acid

$$K_{a3} = \frac{\left[H_3O^+\right]\left[A^{3-}\right]}{\left[HA^{2-}\right]} \qquad \text{(I.46)}$$

A mass balance on the weak acid:

$$\frac{V_a y C_a^{\,0}}{V_a + V_b} = \left[H_3A\right] + \left[H_2A^-\right] + \left[HA^{2-}\right] + \left[A^{3-}\right] \tag{I.47}$$

And the charge balance:

$$[H_3O^+] + [Na^+] = [OH^-] + [H_2A^-] + 2\,[HA^{2-}] + 3\,[A^{3-}] \tag{I.48}$$

Our goal is to solve the set of seven equations for V_b as a function of $[H_3O^+]$ so that the exact buffer capacity for each point during a titration can be calculated. This is most easily done by substituting into the charge balance expression (Equation I.48) equivalent values for $[Na^+]$, $[OH^-]$, $[H_2A^-]$, $[HA^{2-}]$, and $[A^{3-}]$ written exclusively in terms of $[H_3O^+]$ and constant values.

Equations I.44 through I.47 combine to give the well-known acid species distribution relationships for $[H_2A^-]$, $[HA^{2-}]$ and $[A^{3-}]$ in terms of $[H_3O^+]$, K_{a1}, K_{a2} and K_{a3}:

$$\left[H_2A^-\right] = \alpha_1 \frac{V_a y C_a^{\,0}}{(V_a + V_b)} = \left(\frac{K_{a1}[H_3O^+]^2}{[H_3O^+]^3 + K_{a1}[H_3O^+]^2 + K_{a1}K_{a2}[H_3O^+] + K_{a1}K_{a2}K_{a3}}\right)\left(\frac{V_a y C_a^{\,0}}{(V_a + V_b)}\right) \tag{I.49}$$

$$\left[HA^{2-}\right] = \alpha_2 \frac{V_a y C_a^{\,0}}{(V_a + V_b)} = \left(\frac{K_{a1}K_{a2}[H_3O^+]}{[H_3O^+]^3 + K_{a1}[H_3O^+]^2 + K_{a1}K_{a2}[H_3O^+] + K_{a1}K_{a2}K_{a3}}\right)\left(\frac{V_a y C_a^{\,0}}{(V_a + V_b)}\right) \tag{I.50}$$

$$\left[A^{3-}\right] = \alpha_3 \frac{V_a y C_a^{\,0}}{(V_a + V_b)} = \left(\frac{K_{a1}K_{a2}K_{a3}}{[H_3O^+]^3 + K_{a1}[H_3O^+]^2 + K_{a1}K_{a2}[H_3O^+] + K_{a1}K_{a2}K_{a3}}\right)\left(\frac{V_a y C_a^{\,0}}{(V_a + V_b)}\right) \tag{I.51}$$

The charge balance equation (Equation 48) can now be fully substituted. Equation I.2 is used for $[Na^+]$, Equation I.1 is rearrange to express $[OH^-]$ as $K_w/[H_3O^+]$, and Equations I.49, I.50 and I.51 are used for the three charged forms of the acid. The substituted charge balance equation now appears as:

$$\left[H_3O^+\right] + \frac{V_b y C_b^{\,0}}{V_a + V_b} = \frac{K_w}{\left[H_3O^+\right]} + \alpha_1\left(\frac{V_a y C_a^{\,0}}{(V_a + V_b)}\right) + 2\alpha_2\left(\frac{V_a y C_a^{\,0}}{(V_a + V_b)}\right) + 3\alpha_3\left(\frac{V_a y C_a^{\,0}}{(V_a + V_b)}\right)$$

$$= \frac{K_w}{\left[H_3O^+\right]} + (\alpha_1 + 2\alpha_2 + 3\alpha_3)\left(\frac{V_a y C_a^{\,0}}{(V_a + V_b)}\right) \qquad \text{(I.52)}$$

Algebraic manipulation to isolate V_b involves the same steps as previously described:

Multiply both sides by the total volume, $(V_a + V_b)$

$$\left[H_3O^+\right](V_a + V_b) + V_b y C_b^{\,0} = \frac{K_w(V_a + V_b)}{\left[H_3O^+\right]} + (\alpha_1 + 2\alpha_2 + 3\alpha_3) V_a y C_a^{\,0} \qquad \text{(I.53)}$$

Distribute the volume terms to separate V_b and V_a terms:

$$V_a\left[H_3O^+\right] + V_b\left[H_3O^+\right] + V_b y C_b^{\,0} = V_a\frac{K_w}{\left[H_3O^+\right]} + V_b\frac{K_w}{\left[H_3O^+\right]} + (\alpha_1 + 2\alpha_2 + 3\alpha_3) V_a y C_a^{\,0} \qquad \text{(I.54)}$$

Collect all V_b terms on the left:

$$V_b\left[H_3O^+\right] + V_b y C_b^{\,0} - V_b\frac{K_w}{\left[H_3O^+\right]} = V_a\frac{K_w}{\left[H_3O^+\right]} + (\alpha_1 + 2\alpha_2 + 3\alpha_3) V_a y C_a^{\,0} - V_a\left[H_3O^+\right] \qquad \text{(I.55)}$$

Factor out V_b and V_a:

$$V_b\left(\left[H_3O^+\right] + y C_b^{\,0} - \frac{K_w}{\left[H_3O^+\right]}\right) = V_a\left(\frac{K_w}{\left[H_3O^+\right]} + (\alpha_1 + 2\alpha_2 + 3\alpha_3) y C_a^{\,0} - \left[H_3O^+\right]\right) \qquad \text{(I.56)}$$

Isolate V_b:

$$V_b = V_a \frac{\left(\frac{K_w}{\left[H_3O^+\right]} + \left(\alpha_1 + 2\alpha_2 + 3\alpha_3 \right) yC_a^{\,0} - \left[H_3O^+\right] \right)}{\left(\left[H_3O^+\right] + yC_b^{\,0} - \frac{K_w}{\left[H_3O^+\right]} \right)}$$

$$= V_a \frac{\left(\frac{K_w}{\left[H_3O^+\right]} + \left(\frac{K_{a1}[H_3O^+]^2 + 2K_{a1}K_{a2}[H_3O^+] + 3K_{a1}K_{a2}K_{a3}}{[H_3O^+]^3 + K_{a1}[H_3O^+]^2 + K_{a1}K_{a2}[H_3O^+] + K_{a1}K_{a2}K_{a3}} \right) yC_a^{\,0} - \left[H_3O^+\right] \right)}{\left(\left[H_3O^+\right] + yC_b^{\,0} - \frac{K_w}{\left[H_3O^+\right]} \right)} \qquad \text{(I.57)}$$

Note that this expression for V_b is identical to that for the strong acid/strong base case (Equation I.10), the monoprotic weak acid (Equation I.25) and the diprotic weak acid (Equation I.40) except for the coefficient of the middle term in the numerator on the right-hand side.

This expression is now differentiated with respect to $[H_3O^+]$ using the chain rule for a quotient of functions. (Note again it is necessary to replace α_1, α_2 and α_3 with their complete expressions before differentiating because the complete expressions have terms that include $[H_3O^+]$, the variable of differentiation.)

$$\frac{\partial V_b}{\partial\left[H_3O^+\right]} = V_a\left(\left(\frac{1}{\left[H_3O^+\right] + yC_b{}^0 - \frac{K_w}{\left[H_3O^+\right]}}\right)\left\{\frac{-K_w}{\left[H_3O^+\right]^2} + K_{a1}yC_a{}^0\left[\left(\frac{2\left[H_3O^+\right] + 2K_{a2}}{[H_3O^+]^3 + K_{a1}[H_3O^+]^2 + K_{a1}K_{a2}[H_3O^+] + K_{a1}K_{a2}K_{a3}}\right) - \left(\frac{[H_3O^+]^2 + 2K_{a2}[H_3O^+] + 3K_{a2}K_{a3}}{\left([H_3O^+]^3 + K_{a1}[H_3O^+]^2 + K_{a1}K_{a2}[H_3O^+] + K_{a1}K_{a2}K_{a3}\right)^2}\right)\left(3\left[H_3O^+\right]^2 + 2\left[H_3O^+\right]K_{a1} + K_{a1}K_{a2}\right)\right] - 1\right\}\right)$$

$$- \frac{\left(\frac{K_w}{\left[H_3O^+\right]} + yC_a{}^0\left\{\frac{K_{a1}[H_3O^+]^2 + 2K_{a1}K_{a2}[H_3O^+] + 3K_{a1}K_{a2}K_{a3}}{[H_3O^+]^3 + K_{a1}[H_3O^+]^2 + K_{a1}K_{a2}[H_3O^+] + K_{a1}K_{a2}K_{a3}}\right\} - \left[H_3O^+\right]\right)}{\left(\left[H_3O^+\right] + yC_b{}^0 - \frac{K_w}{\left[H_3O^+\right]}\right)^2}\left(1 + \frac{K_w}{\left[H_3O^+\right]^2}\right)$$

(I.58)

Since buffer capacity values relate to pH rather than $[H_3O^+]$, the relationships

$$pH = -\frac{1}{2.303}\ln\left[H_3O^+\right] \qquad \text{(I.12)} \qquad \text{and} \qquad \frac{d\,[H_3O^+]}{d\,pH} = -2.303[H_3O^+] \qquad \text{(I.13)}$$

are again used to express the derivative in terms of pH:

$$\frac{\partial V_b}{\partial\, pH} = -2.303[H_3O^+]V_a \left(\left(\frac{1}{\left[H_3O^+\right] + yC_b{}^0 - \frac{K_w}{\left[H_3O^+\right]}} \right) \left\{ \frac{-K_w}{\left[H_3O^+\right]^2} + K_{a1} yC_a{}^0 \left[\left(\frac{2\left[H_3O^+\right] + 2K_{a2}}{[H_3O^+]^3 + K_{a1}[H_3O^+]^2 + K_{a1}K_{a2}[H_3O^+] + K_{a1}K_{a2}K_{a3}} \right) - \left(\frac{[H_3O^+]^2 + 2K_{a2}[H_3O^+] + 3K_{a2}K_{a3}}{\left([H_3O^+]^3 + K_{a1}[H_3O^+]^2 + K_{a1}K_{a2}[H_3O^+] + K_{a1}K_{a2}K_{a3}\right)^2} \right) \left(3\left[H_3O^+\right]^2 + 2\left[H_3O^+\right]K_{a1} + K_{a1}K_{a2}\right) \right] - 1 \right\} \right)$$

$$- \frac{\left(\frac{K_w}{\left[H_3O^+\right]} + yC_a{}^0 \left\{ \frac{K_{a1}[H_3O^+]^2 + 2K_{a1}K_{a2}[H_3O^+] + 3K_{a1}K_{a2}K_{a3}}{[H_3O^+]^3 + K_{a1}[H_3O^+]^2 + K_{a1}K_{a2}[H_3O^+] + K_{a1}K_{a2}K_{a3}} \right\} - \left[H_3O^+\right] \right)}{\left(\left[H_3O^+\right] + yC_b{}^0 - \frac{K_w}{\left[H_3O^+\right]} \right)^2} \left(1 + \frac{K_w}{\left[H_3O^+\right]^2} \right)$$

(I.59)

Finally, to express the buffer capacity, β, we need to convert the numerator to moles of base by multiplying the volume times the diluted concentration:

$$\beta = -yC_b^{\,0}\,2.303[H_3O^+]V_a\left(\left(\frac{1}{\left[H_3O^+\right] + yC_b^{\,0} - \frac{K_w}{\left[H_3O^+\right]}}\right)\left\{\frac{-K_w}{\left[H_3O^+\right]^2} + K_{a1}yC_a^{\,0}\left[\left(\frac{2\left[H_3O^+\right] + 2K_{a2}}{[H_3O^+]^3 + K_{a1}[H_3O^+]^2 + K_{a1}K_{a2}[H_3O^+] + K_{a1}K_{a2}K_{a3}}\right) - \left(\frac{[H_3O^+]^2 + 2K_{a2}[H_3O^+] + 3K_{a2}K_{a3}}{\left([H_3O^+]^3 + K_{a1}[H_3O^+]^2 + K_{a1}K_{a2}[H_3O^+] + K_{a1}K_{a2}K_{a3}\right)^2}\right)\left(3\left[H_3O^+\right]^2 + 2\left[H_3O^+\right]K_{a1} + K_{a1}K_{a2}\right)\right] - 1\right\}\right)$$

$$- \frac{\left(\frac{K_w}{\left[H_3O^+\right]} + yC_a^{\,0}\left\{\frac{K_{a1}[H_3O^+]^2 + 2K_{a1}K_{a2}[H_3O^+] + 3K_{a1}K_{a2}K_{a3}}{[H_3O^+]^3 + K_{a1}[H_3O^+]^2 + K_{a1}K_{a2}[H_3O^+] + K_{a1}K_{a2}K_{a3}}\right\} - \left[H_3O^+\right]\right)}{\left(\left[H_3O^+\right] + yC_b^{\,0} - \frac{K_w}{\left[H_3O^+\right]}\right)^2}\left(1 + \frac{K_w}{\left[H_3O^+\right]^2}\right)$$

(I.60)

The General Form for Volume of Base (V_b) as a Function of [H_3O^+]

The derivations above reveal that it is possible to write a general equation between the volume of base added in a titration, V_b, and the hydronium ion concentration, [H_3O^+].

Strong Acid/Strong Base Form:

$$V_b = V_a \frac{\left(\frac{K_w}{\left[H_3O^+ \right]} + yC_a{}^0 - \left[H_3O^+ \right] \right)}{\left(\left[H_3O^+ \right] + yC_b{}^0 - \frac{K_w}{\left[H_3O^+ \right]} \right)} \qquad \text{(I.10)}$$

Weak Acid/ Strong Base Form:

$$V_b = V_a \frac{\left(\frac{K_w}{\left[H_3O^+ \right]} + \left(\sum_{i=1}^{n} i\alpha_i \right) yC_a{}^0 - \left[H_3O^+ \right] \right)}{\left(\left[H_3O^+ \right] + yC_b{}^0 - \frac{K_w}{\left[H_3O^+ \right]} \right)} \qquad \text{(I.61)}$$

where the completely protonated form of the acid is uncharged, n is the number of titratable protons, and α's are the fractional coefficients computed from the well-known formulas from acid species distribution diagrams.

Appendix II

Program listings, Instructions and Numerical Methods

This appendix contains programs listings for the four TOPOS programs that have been created during this project. In each case, the program has an initial tab with instructions for using the program and backing it up before use. Some programs have an additional tab that explain the numerical methods that were used to solve the equilibrium equation sets that give rise to the surface values.

II.1 pH/BufCap TOPOS

The pH TOPOS program has already been published in the Journal of Chemical Education[1]. The BufCap TOPOS program will be submitted with the contents of Chapter 4 as a companion paper. Both pH TOPOS and BufCap TOPOS use the same numerical method engine to generate the 3-D surfaces. For that reason, the macro subroutines and numerical methods description are only listed once. Their Instruction tab contents are identical except for the program name and the additional buffer capacity surfaces, so only the pH TOPOS version is included here.

Instructions Tab

pH TOPOS: 3-D Topo Surface Plotting Software
Garon C. Smith, Md Mainul Hossian and Patrick McCarthy
Department of Chemistry and Biochemistry
University of Montana

Instructions for using pH TOPOS, a set of Visual Basic macro-enabled worksheets that generate 3-D topo surfaces above a titration/dilution composition grid.

Before trying any computations with this file, save a copy as a macro-enabled worksheet under a different name to preserve embedded programming and cell

formulas. If you accidetly overwrite some cells, alter a macro, or delete a plot, the program may not function properly.

Do not delete the topo surface from the worksheet. The plot is automatically modified by the program to relate to your new calculations. If you delete it, you will need to start from scratch on making a new surface plot. Axes are labeled automatically by Excel. They are often not optimal from all viewing angles.

This software will automatically compute pH topo surfaces for any monoprotic, diprotic and triprotic acid. All the user need do is:

1. Make sure that the file has been opened and "Macros enabled" has been selected.

2. Select the worksheet tab at the bottom for type of acid to be visualized (monoprotic, diprotic or triprotic).

3. Enter appropriate K_a values in the colored cells on the worksheet. Use exponential notation, i.e., a K_a of 1.75×10^{-5} would be entered as 1.75e-5. (To visualize topo surfaces for strong acid protons, use a K_a of 1×10^{6}.)

The macro for each sheet can be started in two ways. The easiest is to use the short-cut key:

Control+Shift+M for monoprotic

Control+Shift+D for diprotic, and

Control+Shift+T for triprotic

You can alternatively open the "View" menu, then open the "Macros" menu and select "View Macros". A "Macro" window will open with the three programs listed: diprotic, monoprotic and triprotic. Highlight the choice you wish and then click on the "Run" button.

Once activated, the user should see new values percolate through the grid-point matrix. An updated pH topo surface will replace any previous image. The file as

originally download contains the K_a values for the acetic acid, oxalic acid and L-histidine dihydrochloride topos that appear in the main paper.

Rows 20 - 56 on each worksheet correspond to the [H_3O^+] that have been calculated for each grid point as labeled in Column A and Row 20. Further down the sheet, in rows 61-97, are the corresponding pH values that are actually plotted as the pH topos surface.

Once a surface has been generated, it can be freely rotated in any direction to enhance viewing. To do this, right-click on the surface image and select the 3-D Rotation item. Axis labels may need to be repositioned as you rotate the surface. Their positions were optimized for the viewing angle shown in the paper. Excel will automatically adjust the labels during rotation. Sometimes this helps; at other times, it does not.

Excel offer other options for topo plots including solid colored surfaces, color-coded 2-D contour maps or solid colored 2-D contour maps.

Visual Basic Macro Listing

```
Sub Monoprotic()
'
' Monoprotic Macro
' Monprotic acid pH surface
'
' Keyboard Shortcut: Ctrl+Shift+M
'
    Dim Kw As Double
    Dim Ka As Double
```

```
    Dim Va As Double
    Dim Vb As Double
    Dim Ca As Double
    Dim Cb As Double
    Dim Col As Integer
    Dim Row As Integer
    Dim DecimalPlaces As Integer
    Dim H As Double
    Dim FuncValue As Double
    Dim FigStep As Double
'
    Va = Cells(16, 2)
    Kw = Cells(16, 3)
    Ka = Cells(16, 4)
'
    For Row = 0 To 36
        Ca = 10 ^ Cells(Row + 22, 2)
        Cb = 10 ^ Cells(Row + 22, 2)
        For Col = 0 To 40
            Vb = Cells(21, Col + 3) * 0.001
'
' Find first non-zero digit in H+ concentration
```

```
'
        DecimalPlaces = 0
        H = 1
FirstSigFig: FuncValue = H ^ 3 + ((Cb * Vb) / (Va + Vb) + Ka) * H ^ 2 + (-Ka * ((Ca * Va - Cb * Vb) / (Vb + Va)) - Kw) * H - (Ka * Kw)
        If FuncValue <= 0 Then GoTo MoreSigFigs
        H = H / 10
        GoTo FirstSigFig
'
'   Find additional sig figs for H+
'
MoreSigFigs: FigStep = H
        H = H * 10
        DecimalPlaces = DecimalPlaces + 1
SigFigRed:  H = H - FigStep
        FuncValue = H ^ 3 + ((Cb * Vb) / (Va + Vb) + Ka) * H ^ 2 + (-Ka * ((Ca * Va - Cb * Vb) / (Vb + Va)) - Kw) * H - (Ka * Kw)
        If FuncValue > 0 Then GoTo SigFigRed
        H = H + FigStep
        FigStep = FigStep / 10
        DecimalPlaces = DecimalPlaces + 1
        If DecimalPlaces < 15 Then GoTo SigFigRed
```

```
            Cells(Row + 22, Col + 3) = H


        Next Col
    Next Row
End Sub
Sub Diprotic()
'
' Diprotic Macro
' Diprotic acid pH surface
'
' Keyboard Shortcut: Ctrl+Shift+D
'
'
' Diprotic Macro
' Diprotic acid pH surface
'
' Keyboard Shortcut: Ctrl+Shift+D
'
    Dim Kw As Double
    Dim Ka1 As Double
    Dim Ka2 As Double
    Dim Va As Double
```

```
    Dim Vb As Double
    Dim Ca As Double
    Dim Cb As Double
    Dim Col As Integer
    Dim Row As Integer
    Dim DecimalPlaces As Integer
    Dim H As Double
    Dim FuncValue As Double
    Dim FigStep As Double
'
    Va = Cells(16, 2)
    Kw = Cells(16, 3)
    Ka1 = Cells(16, 4)
    Ka2 = Cells(16, 5)
'
    For Row = 0 To 36
        Ca = 10 ^ Cells(Row + 22, 2)
        Cb = 10 ^ Cells(Row + 22, 2)
        For Col = 0 To 40
            Vb = Cells(21, Col + 3) * 0.001
'
'   Find first non-zero digit in H+ concentration
```

```
'
        DecimalPlaces = 0
        H = 1
FirstSigFig: FuncValue = H ^ 4 + (Ka1 + (Cb * Vb) / (Va + Vb)) * H ^ 3 + (Ka1 * Ka2 + Ka1 * (Cb * Vb) / (Va + Vb) - Kw - Ka1 * (Ca * Va) / (Vb + Va)) * H ^ 2 + (Ka1 * Ka2 * (Cb * Vb) / (Va + Vb) - Kw * Ka1 - 2 * (Ca * Va) / (Vb + Va) * Ka1 * Ka2) * H - (Kw * Ka1 * Ka2)
        If FuncValue <= 0 Then GoTo MoreSigFigs
        H = H / 10
        GoTo FirstSigFig
'
'   Find additional sig figs for H+
'
MoreSigFigs: FigStep = H
        H = H * 10
        DecimalPlaces = DecimalPlaces + 1
SigFigRed:  H = H - FigStep
        FuncValue = H ^ 4 + (Ka1 + (Cb * Vb) / (Va + Vb)) * H ^ 3 + (Ka1 * Ka2 + Ka1 * (Cb * Vb) / (Va + Vb) - Kw - Ka1 * (Ca * Va) / (Vb + Va)) * H ^ 2 + (Ka1 * Ka2 * (Cb * Vb) / (Va + Vb) - Kw * Ka1 - 2 * (Ca * Va) / (Vb + Va) * Ka1 * Ka2) * H - (Kw * Ka1 * Ka2)
        If FuncValue > 0 Then GoTo SigFigRed
        H = H + FigStep
        FigStep = FigStep / 10
```

```
        DecimalPlaces = DecimalPlaces + 1
        If DecimalPlaces < 15 Then GoTo SigFigRed
        Cells(Row + 22, Col + 3) = H

    Next Col
  Next Row
End Sub
```

Numerical Methods Tab

The pH for each grid point is calculated by writing the master charge balance equation as a function of $[H_3O^+]$ and rearranging it to a polynomial expression. For a monoprotic acid, it is a cubic equation

$$[H_3O^+]^3 + \left(\frac{C_b V_b}{V_a + V_b} + K_a\right)[H_3O^+]^2 - \left(K_a\left(\frac{C_a V_a - C_b V_b}{V_a + V_b}\right) + K_w\right)[H_3O^+] - K_a K_w = 0$$

Eq I.1

For a diprotic acid it is a quartic equation and for a triprotic acid it is a fifth order polynomial. Due to physical constraints on the problem, only one root exists in the interval between 0 M and 1 M. The macro simply systematically makes guesses for the value of $[H_3O^+]$ and looks for a sign change when substituted into the polynomial function.

Here, for example, is the graph of the function for the first grid point in the acetic acid pH topo surface of the paper. $V_b = 0$ and $C_a = C_b = 1$ M. V_a is always 0.100 L. K_a is 1.75×10^{-5} and K_w is 1×10^{-14}.

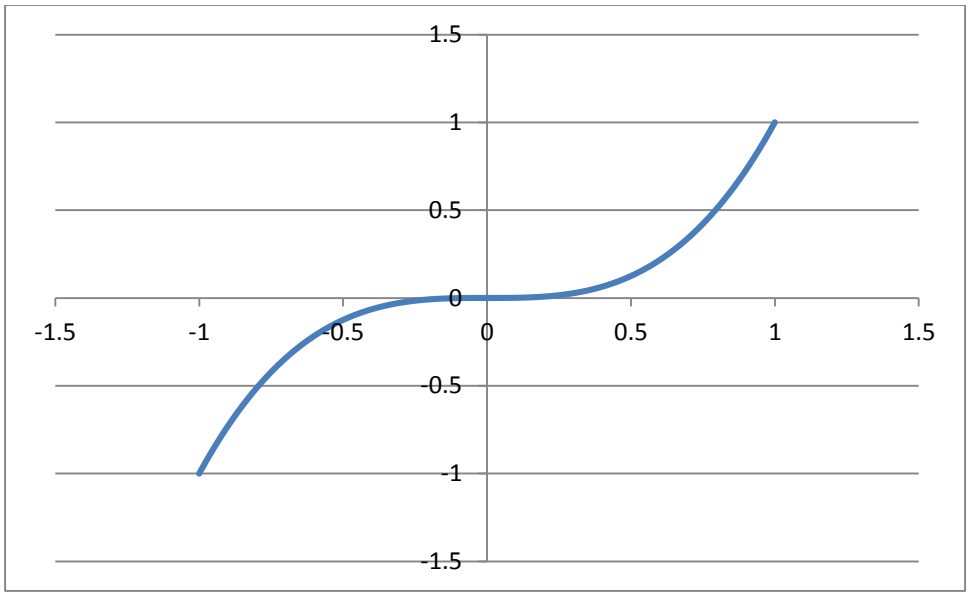

Figure II.1. Plot of the cubic function for the first grid point of the acetic acid pH topo surface. Each grid point on the surface has its own unique cubic equation. This means that the macro solves 41 x 37 = 1517 different cubic equations.

Using a starting guess of 1 M for [H_3O+] always yields a positive functional value. The program makes each subsequent guess for [H_3O^+] as 1/10 of the preceeding one. When a sign change is encountered, the program has found which order of magnitude corresponds to the root. (See Order of Magnitude Search starting at cell V1 to the upper right) Note the function value is negative (yellow cell) for 0.001, so the root is larger than 0.001.

The program then shifts into generating the significant figures for the root one place at a time. The function values returned in finding the first two significant figures of the root are shown in the searc tables at cells V10 and V19 to the right. The negative sign for a guess of 0.0041 M in cell V29 produced a negative sign, so the root is larger than 00.0041 M. Each time the program encounters a sign change, another significant figure has been determined. The numerical search continues until the [H_3O^+] has been confirmed to 16 significant figures. The ultimate [H_3O+] value for this first grid point is 0.0041745592848297 M.

Order of magnitude search	
$[H_30^+]$ guess	Function value
1	1
0.1	0.000998
0.01	8.27E-07
0.001	-1.6E-08

1st sig fig search	
0.010	8.27E-07
0.009	5.73E-07
0.008	3.73E-07
0.007	2.21E-07
0.006	1.12E-07
0.005	3.79E-08
0.004	-5.7E-09

2nd sig fig search	
0.0050	3.79E-08
0.0049	3.23E-08
0.0048	2.7E-08
0.0047	2.2E-08
0.0046	1.72E-08
0.0045	1.27E-08
0.0044	8.52E-09
0.0043	4.58E-09
0.0042	8.97E-10
0.0041	-2.5E-09

Because of the wide range of conditions encountered, the Solver Tool in Excel is not capable of reliably finding solutions, particularly in dilute settings. While it is faster to solve an equation in many instances, it will diverge and return a "no solution found" message for many grid points in flatish portions of the topos, especially the very dilute regions. The sign change technique is highly robust against divergence.

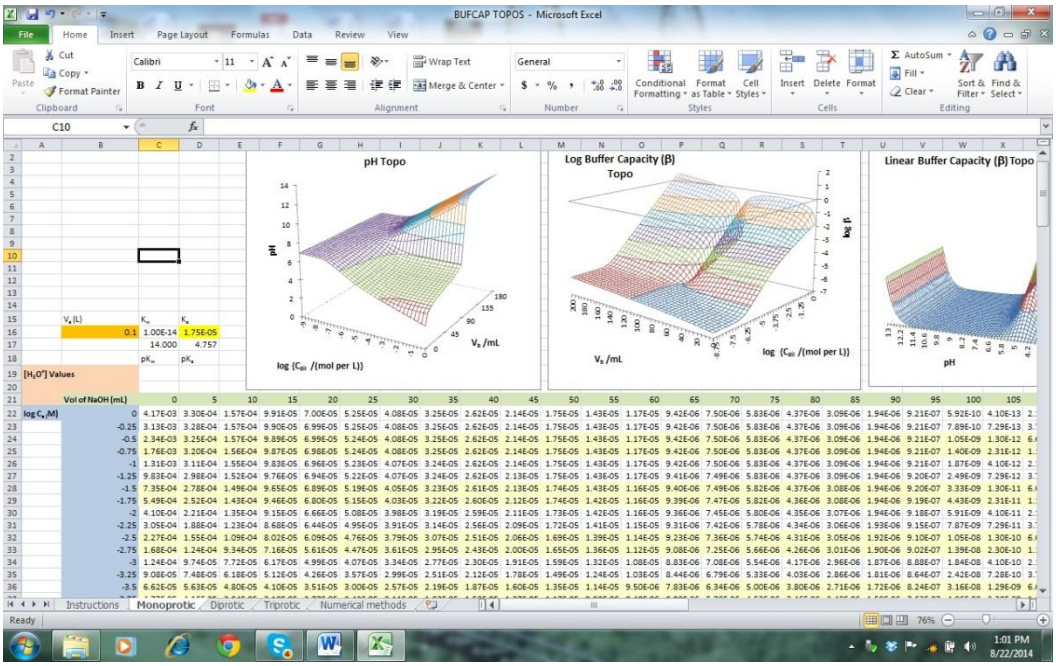

Figure AII.1. User screen for the pH/BufCap TOPOS program.

II.2 Complexation TOPOS

The Complexation TOPOS program instructions are similar to those for pH TOPOS except that more detail is required in describing the exact form of the thermodynamic constants that are used as inputs. In this instance all data are input as the logarithmic form of their overall formation constants. Values are required for each complex that will form, for each protonated form of the uncomplexed ligand and for any hydrolytic hydroxo-complexes that the metal is known to form. This requires that K_a or pK_a values for the ligand first be cumulated. Then they need to be adjusted from the dissociation direction to the association direction which means cumulated K_as be inverted or the cumulated pK_as have the sign changed. An additional parameter that must be entered is the pH that will be maintained over the entire surface.

Visual Basic Macro Listing

```
Sub Surface()
'
' Metal-ligand complexation surface
' Logarithmic composition grid
'
' Keyboard Shortcut: Ctrl+Shift+M
'
    Dim H As Double
    Dim OH As Double
    Dim B1 As Double
    Dim B2 As Double
```

```
Dim B3 As Double
Dim B4 As Double
Dim B5 As Double
Dim B6 As Double
Dim BMOH1 As Double
Dim BMOH2 As Double
Dim BH1 As Double
Dim BH2 As Double
Dim BH3 As Double
Dim BH4 As Double
Dim BH5 As Double
Dim BH66 As Double
Dim Row As Integer
Dim Col As Integer
Dim TotLig As Double
Dim TotMet As Double
Dim CalcMet As Double
Dim CalcLig As Double
Dim FreeMet As Double
Dim FreeLig As Double
Dim NumbIter As Integer
Dim NumbConv As Integer
```

```
    Dim LigGuess As Double
    Dim MetGuess As Double
    Dim DifMet As Double
    Dim DifLig As Double
'
' Initialize formation and protonation constants
'
    B1 = 10 ^ Cells(3, 2)
    B2 = Cells(4, 2)
    If B2 <> 0 Then B2 = 10 ^ B2
    B3 = Cells(5, 2)
    If B3 <> 0 Then B3 = 10 ^ B3
    B4 = Cells(6, 2)
    If B4 <> 0 Then B4 = 10 ^ B4
    B5 = Cells(7, 2)
    If B5 <> 0 Then B5 = 10 ^ B5
    B6 = Cells(8, 2)
    If B6 <> 0 Then B6 = 10 ^ B6
    BH1 = 10 ^ Cells(11, 2)
    BH2 = Cells(12, 2)
    If BH2 <> 0 Then BH2 = 10 ^ BH2
    BH3 = Cells(13, 2)
```

```
   If BH3 <> 0 Then BH3 = 10 ^ BH3
   BH4 = Cells(14, 2)
   If BH4 <> 0 Then BH4 = 10 ^ BH4
   BH5 = Cells(15, 2)
   If BH5 <> 0 Then BH5 = 10 ^ BH5
   BH6 = Cells(16, 2)
   If BH6 <> 0 Then BH6 = 10 ^ BH6
   BMOH1 = Cells(19, 2)
   If BMOH1 <> 0 Then BMOH1 = 10 ^ Cells(19, 2)
   BMOH2 = Cells(20, 2)
   If BMOH2 <> 0 Then BMOH2 = 10 ^ BMOH2
   BMOH3 = Cells(21, 2)
   If BMOH3 <> 0 Then BMOH3 = 10 ^ BMOH3
   H = 10 ^ -Cells(23, 2)
   OH = 0.00000000000001 / H
   Base10 = Log(10)
'
' Start grid point loops
'
   For Row = 0 To 36
      TotLig = 10 ^ Cells(Row + 27, 2)
      For Col = 0 To 36
```

```
        TotMet = 10 ^ Cells(26, Col + 3)
'
'   Set initial guess for free species
'
        FreeMet = TotMet * 0.001
        FreeLig = TotLig * 0.0000001
'
'   Set iteration loop counter
'
        NumbIter = 0
'
'   Set convergence check flag at start of iteration
'
Iteration:  NumbConv = 0
'
'   Use current guesses in mass balance equations
'
CalcMet = FreeMet + BMOH1 * FreeMet * OH + BMOH2 * FreeMet * OH ^ 2 + B1
* FreeMet * FreeLig + B2 * FreeMet * FreeLig ^ 2 + B3 * FreeMet * FreeLig ^ 3 +
B4 * FreeMet * FreeLig ^ 4 + B5 * FreeMet * FreeLig ^ 5 + B6 * FreeMet * FreeLig
^ 6
CalcLig = FreeLig + BH1 * H * FreeLig + BH2 * H ^ 2 * FreeLig + BH3 * H ^ 3 *
FreeLig + BH4 * H ^ 4 * FreeLig + BH5 * H ^ 5 * FreeLig + BH6 * H ^ 6 * FreeLig +
```

```
B1 * FreeMet * FreeLig + 2 * B2 * FreeMet * FreeLig ^ 2 + 3 * B3 * FreeMet *
FreeLig ^ 3 + 4 * B4 * FreeMet * FreeLig ^ 4 + 5 * B5 * FreeMet * FreeLig ^ 5 + 6 *
B6 * FreeMet * FreeLig ^ 6


'
'   Compute mass balance errors, set convergence flags
'
DifMet = Abs(TotMet - CalcMet)
If DifMet <= 0.000001 * TotMet Then NumbConv = NumbConv + 1
DifLig = Abs(TotLig - CalcLig)
If DifLig <= 0.000001 * TotLig Then NumbConv = NumbConv + 1
'
'Check convergence flags for both converged
'
If NumbConv = 2 Then GoTo StoreData
'
'   Refine free species guesses since not converged
'
FreeMet = FreeMet * (TotMet / CalcMet) ^ 0.5
FreeLig = FreeLig * (TotLig / CalcLig) ^ 0.5
'
'   Update iteration counter, check for iteration limit
```

```
'

NumbIter = NumbIter + 1

If NumbIter = 1000 Then GoTo StoreData

GoTo Iteration

'

'   Store free species values in cells

'

StoreData:  Cells(Row + 69, Col + 3) = FreeMet

            Cells(Row + 111, Col + 3) = FreeLig


        Next Col

    Next Row


End Sub
```

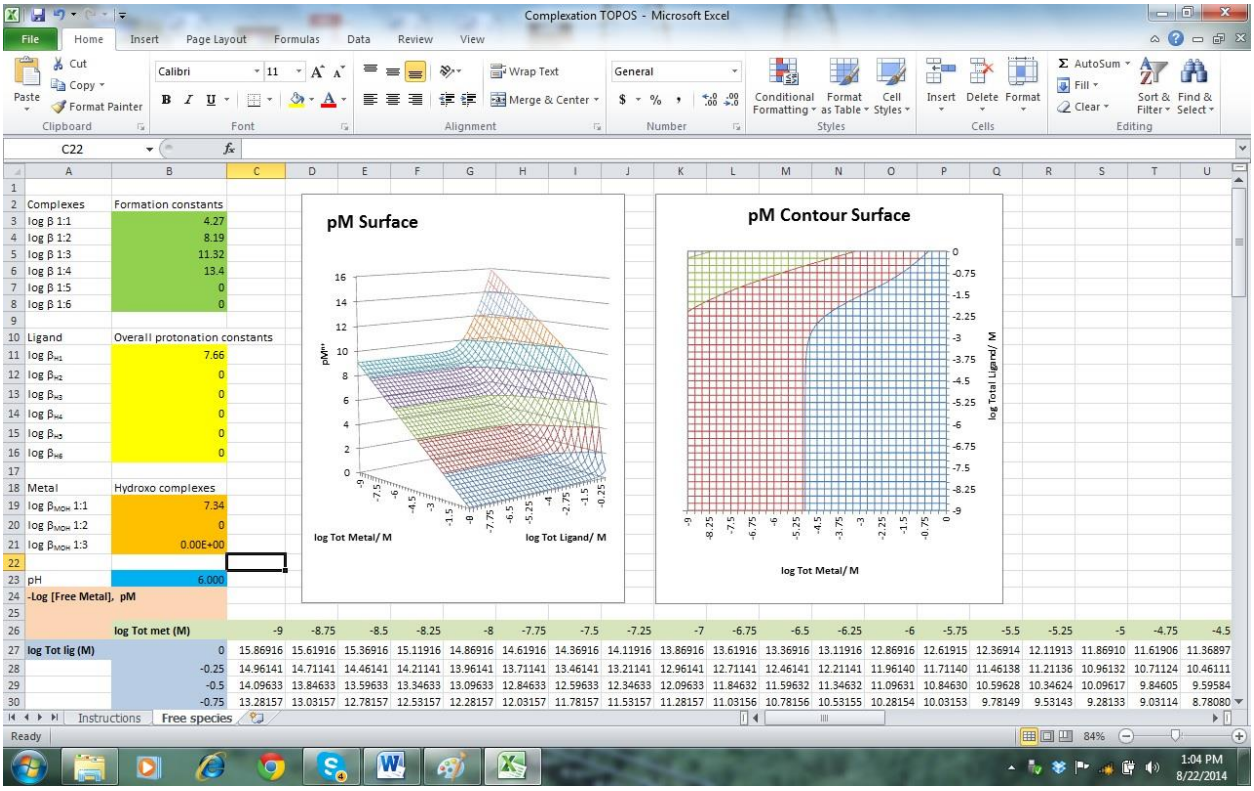

Figure AII.2. User screen for Complexation TOPOS program.

II.3 Redox TOPOS

The Redox TOPOS program is different in that no numerical methods are required to compute the potential for each grid point coordinates. The entire calculation is done with a simple embed formula. Three inputs for this program allow a user to see the real-time effect of changing the standard resduction potential (E^0), the number of electrons (n) or the temperature (K). Other input cells allow the inclusion of 1) pure phases (liquid or solid); and 2) pH or acid/base species in the half reaction of interest.

Instruction tab

Instructions for using Redox TOPOS, a set of worksheets that generate 3-D topo surfaces above a redox composition grid.

Before trying any computations with this file, save a copy under a different name to preserve embedded programming and cell formulas. If you accidently overwrite some cells or delete a plot, the program may not function properly.

Do not delete the topo surface from the worksheet. The plot is automatically modified by the program to relate to your new calculations. If you delete it, you will need to start from scratch on making a new surface plot. Axes are labeled automatically by Excel. They are often not optimal from all viewing angles.

This software will automatically compute a Nernst potential topo surface based on the parameters associated with the half-reaction of interest. All half-reactions are considered to be in the form that corresponds to its Standard Reduction potential. The general form of that would be:

$$a\ Ox + n\ e^- \leftrightarrow c\ Red \qquad E^0 = \text{ in Volts}$$

Often, a half-reaction will include H_3O^+ (or more simply H^+) on the left-hand side or OH^- on the right-hand side with accompanying H_20 as needed.

$$a\ Ox + b\ H^+ + n\ e^- \leftrightarrow c\ Red + b/2\ H_2O \qquad \text{for acid conditions}$$

or

$$a\,Ox + 2d\,H_2O + n\,e^- \leftrightarrow c\,Red + d\,OH^- \qquad \text{for basic conditions}$$

All three of these forms of half-cell reactions have been incorporated into the worksheets with the Nernst equation written in the form

$$\mathcal{E} = \mathcal{E}^0 + \frac{R\mathcal{T}}{n\mathcal{F}} \ln \frac{[Ox]^a}{[Red]^c} \left(\frac{[H_3O^+]^b}{[OH^-]^d} \right)$$

$$= \mathcal{E}^0 + 0.000198423 \frac{\mathcal{T}}{n} \log \frac{[Ox]^a [H_3O^+]^b}{[Red]^c [OH^-]^d}$$

Two types of input devices, sliders and input cells, are present through which the user tells the Redox TOPOS worksheet which surface to generate.

Three input devices are sliders. These are employed to enter the E^0 value , the number of electrons (n), and the temperature (in °C) for the half-reaction.

E^0 values can range from -3.000 V to +3.000 V. The current setting of the slider is visible in cell B1 immedi-

ately above the slide bar. The mouse can be used to adjust the slider to an approximate value. Then clicking on the < and > slide bar buttons will let you adjust to an exact final value in 0.001 V increments.

n, the number of electrons, can vary from 1 e^- to 6 e^-. Manipulate the slider until the desired n-value appears

in cell B5 immediately above the slide bar. The < and > slide bar buttons can also be used to make a

selection.

T values can range from 0°C to 100°C, or 273.15K to 373.15K, the entire possible liquid range of water. The

current setting off the slider appears in both temperature scales in cells B9 (celsius) and D9 (kelvin). The

computations are done utilizing the kelvin temperature. The mouse can be used to adjust the slider to an

approximate value. Then clicking on the < and > slide bar buttons will let you adjust to an exact final

temperature in 0.01^{o} increments.

There are five input cells -- four control the coefficients in the half-reaction of interest and one stipulates the pH value to be used for the calculations. These are all found in the lavendar-shaded area between lines 13 and 19.

The Coefficient of the Oxidized form is entered into cell B14. The default value is 1. If the half-reaction of

interest requires a higher coeficient, enter it here. If the oxidized form is a pure phase, e.g., $Br_2(l)$, enter a 0 here.

The Coefficient of the Reduced form is entered into cell D14. The defaultl value is 1. If the half-reaction of

interest requires a higher coefficient, enter it here. If the reduced form is a pure phase, e.g., Fe(*s*), enter a 0

here.

The Coefficient for H^+ in acid medium half-reactions is entered into cell B16. If H^+ is not present in the half-

reaction, enter a 0 here. The default value for this cell is 0 since most half-reactions do not involve H^+.

The Coefficient for OH^- in basic medium half-reactions is entered into cell B18. If OH^- is not present in the half-

reaction, enter a 0 here. The default value for this cell is 0 since most half-reactions do not involve OH^-.

The pH va;ue for surface calculations is entered into cell D9. Upon entering a pH value, the spreadsheet

automatically displays the equivalent H^+ molar concentration in cell F16 and the equivalent OH^- molar

concentration in cell F18.

As soon as any input value is changed, the user should see new values percolate through the grid-point matrix. An updated Nernst potential topo surface will replace any previous image. The file as originally download contains the input values for the Fe^{3+}/Fe^{2+} half-reaction at 25^0C and a standard reduction potential of 0.771 V.

Rows 24- 64 on the worksheet correspond to the E values that have been calculated for each grid point composition as labeled in Column A and Row 23.

Once a surface has been generated, it can be freely rotated in any direction to enhance viewing. To do this, right-click on the surface image and select the 3-D Rotation item. Axis labels may need to be repositioned as you rotate the surface. Their positions were optimized for the viewing angle shown in the paper. Excel will automatically adjust the labels during rotation. Sometimes this helps; at other times, it does not.

Excel offer other options for topo plots including solid colored surfaces, color-coded 2-D contour maps or solid colored 2-D contour maps.

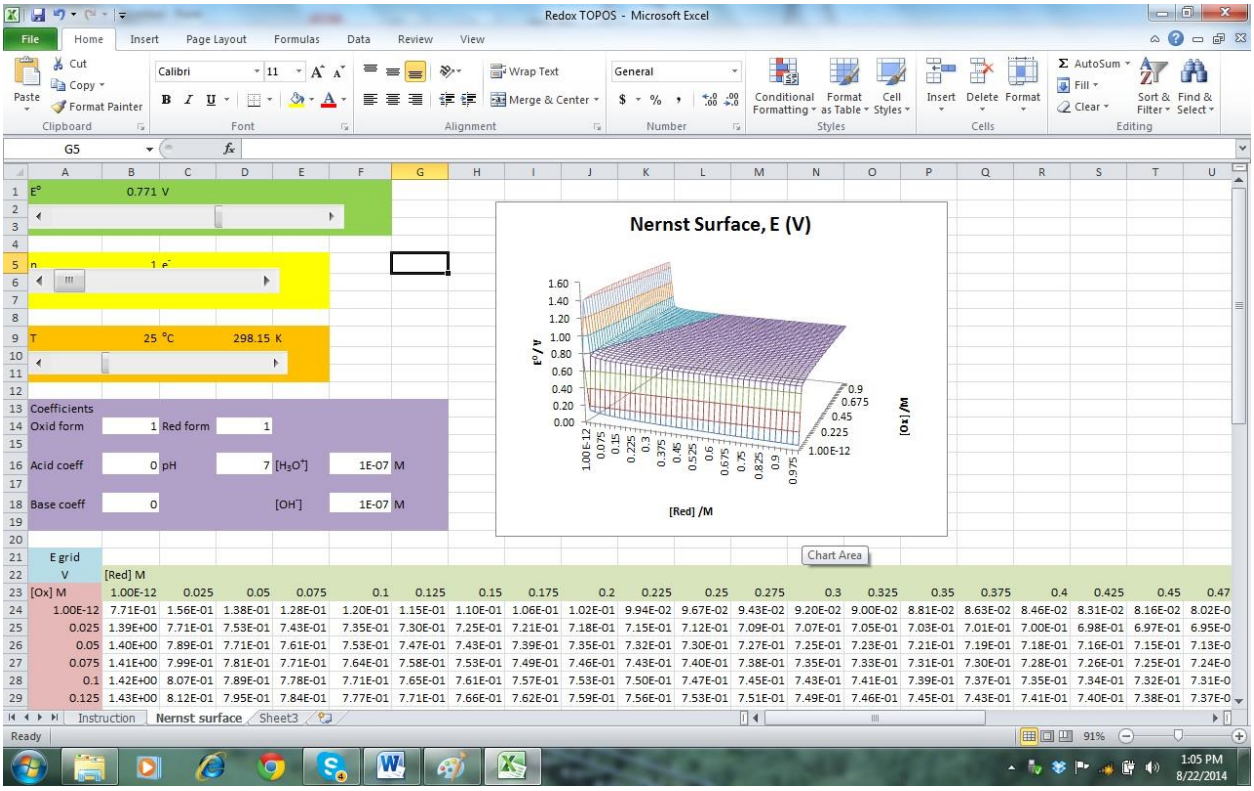

Figure AII.3. User screen for Redox TOPOS program.

II.4 Solubility TOPOS

The Solubility TOPOS program is under development. At this writing it only implements the Simple K_{sp} model for sparingly soluble salts that have a stoichiometry with one component ion possessing a subscript of 1, i.e., 1:1, 1:2, 1:3, 2:1 and 3:1. User inputs for this simple case are the stoichiometry of interest and the K_{sp} value for the salt.

Visual Basic Macro Listing

```
Sub Case1()
'
' Case 1 - No complexes (version of 140508
' Solubility surface
'
' Keyboard Shortcut: Ctrl+Shift+M
'
    Dim CaseNumb As Integer
    Dim MetSub As Integer
    Dim LigSub As Integer
    Dim Ksp As Double
    Dim Row As Integer
    Dim Col As Integer
    Dim TotLig As Double
    Dim TotMet As Double
```

```
    Dim Solubility As Double
    Dim FreeMet As Double
    Dim FreeLig As Double
    Dim XSLig As Double
    Dim XSMet As Double
    Dim IterCount As Integer
    Dim LigGuess As Double
    Dim MetGuess As Double
'
    Cells(10, 1) = ""
    CaseNumb = Cells(13, 2)
    If CaseNumb = 1 Then MetSub = 1: LigSub = 1: GoTo LegitCase
    If CaseNumb = 2 Then MetSub = 1: LigSub = 2: GoTo LegitCase
    If CaseNumb = 3 Then MetSub = 2: LigSub = 1: GoTo LegitCase
    If CaseNumb = 4 Then MetSub = 1: LigSub = 3: GoTo LegitCase
    If CaseNumb = 5 Then MetSub = 3: LigSub = 1: GoTo LegitCase
    If CaseNumb = 6 Then MetSub = 2: LigSub = 3: GoTo LegitCase
    If CaseNumb = 7 Then MetSub = 3: LigSub = 2: GoTo LegitCase
    Cells(10, 1) = "Illegal Case Number": GoTo WrongCase
'
LegitCase:
    Ksp = Cells(16, 2)
```

```
'
   For Row = 0 To 36
      TotLig = 10 ^ Cells(Row + 22, 2)
      For Col = 0 To 36
         TotMet = 10 ^ Cells(21, Col + 3)
'
'  Determine whether solid is present
'
         If TotMet ^ MetSub * TotLig ^ LigSub > Ksp Then GoTo SolidPresent
'
'  No precipitate.  Determine which component is in excess
'
         FreeMet = TotMet: FreeLig = TotLig
         If (TotMet / MetSub) > (TotLig / LigSub) Then Solubility = TotLig / LigSub
         If (TotMet / MetSub) = (TotLig / LigSub) Then Solubility = TotMet / MetSub
         If (TotMet / MetSub) < (TotLig / LigSub) Then Solubility = TotMet / MetSub
         GoTo StoreData
'
'  Branch to subroutine based on precipitate stoichiometry
'
SolidPresent:
   If MetSub = 1 Then GoTo MetSub1
```

```
'   If LigSub = 1 Then GoTo LigSub1
'
'   Calculations for formulas with just one cation
'
MetSub1:
   If TotMet = (TotLig / LigSub) Then FreeMet = (Ksp / (LigSub ^ LigSub)) ^ (1 /
(LigSub + 1)): FreeLig = LigSub * FreeMet: Solubility = FreeMet: GoTo StoreData
   If TotMet > (TotLig / LigSub) Then GoTo M1XSMetal
'
'   Excess ligand is present
'
M1XSLigand:
   XSLig = TotLig - (LigSub * TotMet): LigGuess = XSLig: IterCount = 1

M1RefineLigand:
   MetGuess = Ksp / LigGuess ^ LigSub
   LigGuess = XSLig + (LigNum * MetGuess)
   IterCount = IterCount + 1
   If IterCount = 8 Then Solubility = MetGuess: FreeLig = LigGuess: FreeMet =
MetGuess: GoTo StoreData
   GoTo M1RefineLigand
'
```

```
'   Excess metal is present
'
M1XSMetal:
   XSMet = TotMet - (TotLig / LigSub): MetGuess = XSMet: IterCount = 1

M1RefineMetal:
   LigGuess = (Ksp / MetGuess) ^ (1 / LigSub)
   MetGuess = XSMet + (LigGuess / LigSub)
   IterCount = IterCount + 1
   If IterCount = 8 Then Solubility = (LigGuess / LigSub): FreeMet = MetGuess:
FreeLig = LigGuess: GoTo StoreData
   GoTo M1RefineMetal

LigSub1:
   If (TotMet / MetSub) = (TotLig / LigSub) Then FreeLig = (Ksp / (MetSub ^
MetSub)) ^ (1 / (MetSub + 1)): FreeMet = MetSub * FreeLig: Solubility = FreeLig:
GoTo StoreData
   If (TotMet / MetSub) > (TotLig / LigSub) Then GoTo L1XSMetal
'
'   Excess ligand is present
'
L1XSLigand:
   XSLig = TotLig - (MetSub * TotMet): LigGuess = XSLig: IterCount = 1
```

```
L1RefineLigand:
   MetGuess = Ksp / LigGuess ^ LigSub
   LigGuess = XSLig + (MetNum * MetGuess)
   IterCount = IterCount + 1
   If IterCount = 8 Then Solubility = MetGuess: FreeLig = LigGuess: FreeMet =
MetGuess: GoTo StoreData
   GoTo L1RefineLigand
'
'  Excess metal is present
'
L1XSMetal:
   XSMet = TotMet - (TotLig / LigSub): MetGuess = XSMet: IterCount = 1

L1RefineMetal:
   LigGuess = (Ksp / MetGuess) ^ (1 / LigSub)
   MetGuess = XSMet + (LigGuess / LigSub)
   IterCount = IterCount + 1
   If IterCount = 8 Then Solubility = (LigGuess / LigSub): FreeMet = MetGuess:
FreeLig = LigGuess: GoTo StoreData
   GoTo L1RefineMetal
```

```
'
'  Store the solubility and free species data
'
StoreData:  Cells(Row + 22, Col + 44) = Solubility
            Cells(Row + 64, Col + 44) = FreeMet
            Cells(Row + 106, Col + 44) = FreeLig
        Next Col
    Next Row
WrongCase:
End Sub
```

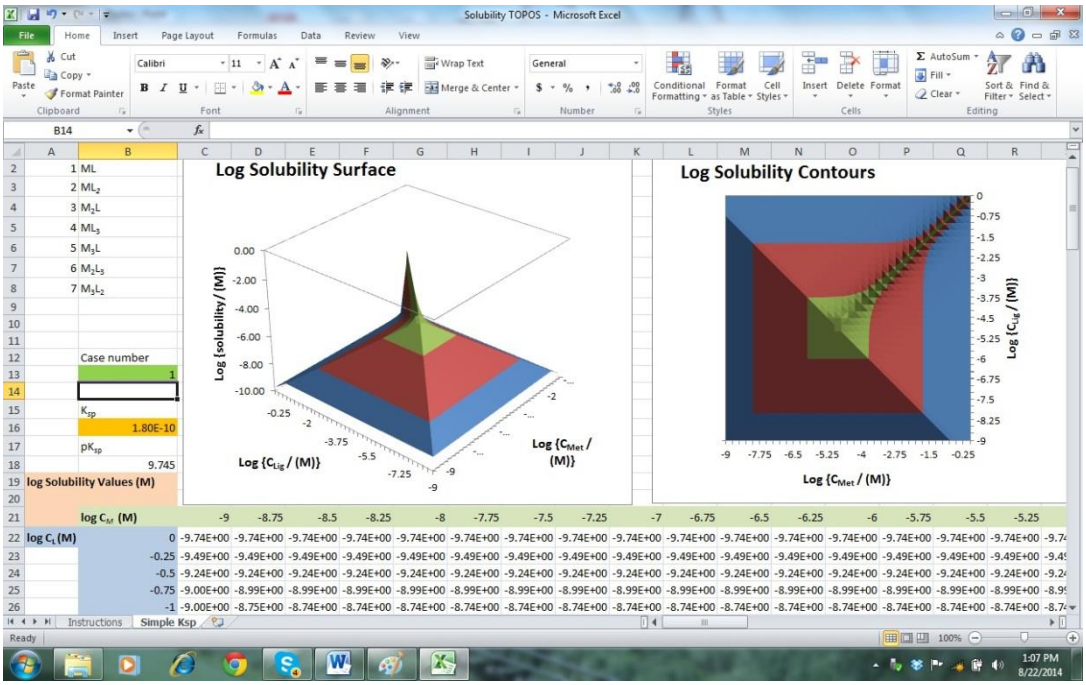

Figure AII.4. User screen for Solubility TOPOS program.